Collective effects of microswimmers in nematic liquid crystals

Bhavesh Gautam

THÈSE PRÉSENTÉE
POUR OBTENIR LE GRADE DE

DOCTEUR
DE L'UNIVERSITÉ DE BORDEAUX

ÉCOLE DOCTORALE DES SCIENCES PHYSIQUES ET DE L'INGÉNIEUR

SPÉCIALITÉ - LASERS, MATIÈRE ET NANOSCIENCES

par **Bhavesh GAUTAM**

****

Titre/Title:

Effets collectifs des micronageurs dans les cristaux liquides nématiques

Collective Effects of Microswimmers in Nematic Liquid Crystals

****

Sous la direction de: **Juho LINTUVUORI**

Soutenue le 15/04/2024

Membres du jury

Mme. Emmanuelle Lacaze	Directrice de recherche, INSP, Sorbonne Université	Rapportrice
Mme. Christine Grauby-Heywang	Professeure d'université, LOMA, Université de Bordeaux	Examinatrice
M. Marco Mazza	Associate Professor, Loughborough University	Rapporteur
M. Philippe Poulin	Directeur de recherche, CRPP, Université de Bordeaux	Examinateur
M. Alois Würger	Professeur d'université, LOMA, Université de Bordeaux	Invitée
M. Juho Lintuvuori	Chargé de recherche, CNRS, LOMA	Invitée

Acknowledgment

I express my sincere gratitude to my supervisor, Juho Lintuvuori, for his unwavering support throughout the thesis. I am also deeply thankful to my parents and sisters, who always encouraged me and provided support from afar (India).

A special appreciation goes to my friends: Maryam, Toni, Angela, Xunyi, and, of course, Christos, for our traditional "Friday nights", and for making my time in Bordeaux one of the most memorable experiences. I wish I could mention all my lab colleagues, but I extend my thanks to Apurba, Jonny, Andrea, Alpesh, Samlan and Vagharshak for making every lunch interesting and enjoyable.

I am thankful to the members of the jury, Marco Mazza, Emmanuelle Lacaze, Christine Grauby-Heywang, and Philippe Poulin, for their valuable participation in the evaluation process. Special thanks to Alois Würger for insightful perspectives on the project.

Résumé

Effets collectifs des micronageurs dans les cristaux liquides nématiques

La thèse se concentre sur les effets collectifs des micro-nageurs dans les cristaux liquides nématiques. En utilisant des simulations de Boltzmann sur réseau, nous étudions un système composé de nageurs sphériques au sein d'un cristal liquide nématique. Nos résultats révèlent que le couplage entre les champs de flux du nageur et l'élasticité cristalline liquide peut déstabiliser l'alignement nématique uniforme. Dans l'espace quasi-2D, nous observons l'émergence d'une instabilité dominée par la flexion avec les propulseurs, ce qui est en accord avec les expériences de bactéries dans des films nématiques minces.

Après l'ouverture de la troisième dimension, une rupture spontanée de la symétrie chirale est observée ; l'état nématique uniforme devient instable et se transforme en un état cholestérique (chiral), caractérisé par une torsion continue du champ directeur. Cela est observé à la fois pour les nageurs propulseurs (extensiles) et les nageurs tracteurs (contractiles). En analysant les déformations dans le champ directeur nématique, l'instabilité dominante est identifiée comme étant la torsion-flexion. Nos simulations démontrent que la dynamique des particules et le directeur nématique sont connectés. Dans l'état chiral, tant les nageurs propulseurs que les nageurs tracteurs présentent des trajectoires hélicoïdales.

De plus, des stratégies pour contrôler la dynamique des micro-nageurs sont également étudiées. Motivés par des expériences bactériennes, nous considérons des nageurs de types propulseur et tracteur au sein de motifs nématiques. En accord avec les expériences, nos résultats montrent qu'un propulseur présente une trajectoire circulaire dans une déformation en flexion pure et une trajectoire linéaire dans une déformation en éventail pure. Pour un nageur tracteur, un comportement opposé est observé. Enfin, nous explorons le transport de cargaison de particules colloïdales enchevêtrées par des défauts topologiques. Nos simulations suggèrent que le remplacement d'une colloïde passive par un nageur sphérique n'affecte pas le défaut topologique partagé et fournit une mobilité. La particule active est observée pour se lier à la cargaison via un défaut topologique. Avec un nageur propulseur, nous observons un transport guidé le long du directeur nématique, tandis qu'avec un tracteur, un transport perpendiculaire au directeur nématique est observé.

Mots-clés: Micro-nageurs, Dynamique collective, Cristaux liquides nématiques, Rupture spontanée de la symétrie chirale

Abstract

Collective effects of microswimmers in nematic liquid crystals

The thesis focuses on the collective effects of microswimmers in nematic liquid crystals. Using hydrodynamic simulations, we study a system consisting of spherical swimmers within a nematic liquid crystal. Our findings reveal that coupling between the swimmer flow fields and the liquid crystalline elasticity can destabilize the uniform nematic alignment. In quasi-2D space, we observe the emergence of bend-dominated instability with pushers, which is in agreement with experiments of bacteria in thin nematic films.

After opening the 3rd dimension, a spontaneous chiral symmetry breaking is observed; the uniform nematic state becomes unstable and transitions into a cholesteric-like (chiral) state, characterized by a continuous twist in the director field. This is observed for both pusher (extensile) and puller (contractile) swimmers. By analyzing the deformations in the nematic director field, the dominant instability is found to be twist-bend. Our simulations demonstrate that the particle dynamics and nematic director are connected. In the chiral state, both pusher and puller swimmers exhibit helical trajectories.

Further, strategies for controlling microswimmer dynamics are also studied. Motivated by bacterial experiments, we consider swimmers of both pusher and puller types within nematic patterns. In agreement with experiments, our findings show that a pusher exhibits circular trajectory in a pure bend and linear trajectory in a pure splay. For a puller swimmer, opposite behavior is observed. Finally, we explore cargo transport of colloidal particles entangled by topological defects. Our simulations suggest that replacing a passive colloid with a spherical swimmer does not affect the shared topological defect and provides motility. The active particle is observed to bind to the cargo via a topological defect. With a pusher swimmer, we observe guided transport along the nematic director, while with a puller, transport is observed to be perpendicular to the nematic director.

Keywords: Micro-swimmers, Collective dynamics, Nematic liquid crystals, Spontaneous chiral symmetry breaking

Contents

Chapter 1

Introduction

1.1 | Microswimmers

Active particles, such as microswimmers, use energy to propel themselves through various environments. Typically living on a microscopic scale, they exist in nature as organisms like bacteria, algae, and sperm. However, artificial microswimmers, such as Janus spheres, Janus rods, and vesicles, can also be engineered for specific applications [1]. Some examples of natural and artificial microswimmers are shown in Figure 1.1.

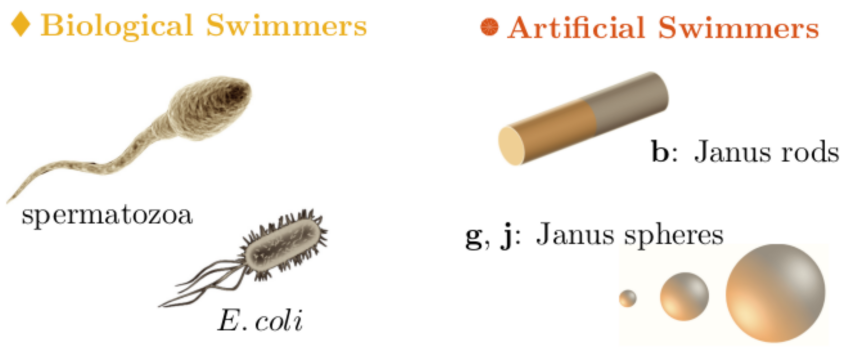

Figure 1.1: **Microswimmer examples**: The figure shows examples of both natural (spermatozoa and *Escherichia coli*) and artificial microswimmers (Janus rod and Janus spheres of varying radii). The figure is taken from [2].

1.1.1 | Motility of microswimmers

Natural microswimmers

In nature, microswimmers often swim for their survival. *Escherichia coli*, for instance, exhibits chemotaxis (movement along nutrient gradients) to locate environments rich in nutrients [3]. Many algae also exhibit strategic motility to optimize their position relative to light gradients, which helps them find suitable habitats and avoid adverse conditions [4].

Motility is also a crucial aspect of reproductive processes. Sperm navigate the female reproductive tract with precision, aiming to reach and fertilize the egg [5]. Understanding the swimming behavior of a microswimmer can help us explain various physical processes.

Artifical microswimmers

Researchers have been trying to mimic the efficient movement observed in natural microswimmers [6, 1, 7, 8]. Significant progress has been made with the fabrication of artificial microswimmers [2]. However, controlling their dynamics for potential applications remains an active area of research. Depending on the type of artificial microswimmer, researchers use a variety of methods to guide them [9, 2]. These include the use of chemical gradients in the surrounding environment [9], and applying external fields on the microswimmers [10, 11]. Another practical approach involves the use of confining walls. For example, in an experimental study, a chemically driven Janus sphere was shown to swim parallel to and in proximity to confining walls [12]. The attraction towards solid surfaces has been observed with swimming bacteria in confined environments [13, 14].

Swimming at micrometer scale

Microswimmers have various propulsion mechanisms to create flow fields around them [14, 15]. At the micron scale, fluid dynamics differ from the macro scale [16] and can be characterized by a Reynolds Number (Re). The Reynolds number is defined as the ratio of inertial to viscous forces acting on a swimming body, given by $Re = \frac{\rho U L}{\eta}$, where L is the body size, U is the swimming velocity, η is the fluid viscosity, and ρ is the fluid density [14]. Typically, Reynolds numbers for microswimmers range from 10^{-2} to 10^{-5} [14]. Thus, the Navier-Stokes equations can be effectively simplified by removing the inertial term. These modified equations are known as the Stokes equations, one can solve them with suitable boundary conditions to find steady-state flow fields around microswimmers [14].

1.2 | Collective phenomenon in isotropic environment

On an individual scale, the dynamics of microswimmers have been extensively explored in experiments [17, 15, 18, 13]. Nevertheless, in the natural environment, microswimmers rarely found alone; they almost always exist in groups. Thus, their motion is not independent but rather influenced by each other in a complex way. Physical systems characterized by a high volume fraction of microswimmers can show remarkable phenomena (Figure 1.2), including swarming [19, 20, 21], the formation of biofilms [22, 23, 24, 25], and vortex formation [26, 27]. Many of these collective behaviors are necessary for the survival of bacterial colonies. For instance, swarming (Figure 1.2a), a phenomenon where bacteria undergo rapid mass migration across a surface, is vital for efficient nutrient search. Another crucial

collective behavior is the formation of biofilm by bacterial colonies (Figure 1.2b). When exposed to antimicrobial substances, certain bacteria can self-organize into 3D multicellular structures, enhancing their resilience against the antimicrobial environment [22, 24].

Collective phenomena often result from hydrodynamic interactions [20, 26, 28, 29]. When microswimmers are in close proximity, they can exert forces on each other through the surrounding fluid, thereby influencing their dynamics. One such example is shown in Figure 1.2c, the formation of a bacterial vortex in a densely populated bacterial suspension confined within a flattened droplet [27]. This vortex formation can be explained by considering hydrodynamic interactions between the bacteria [26].

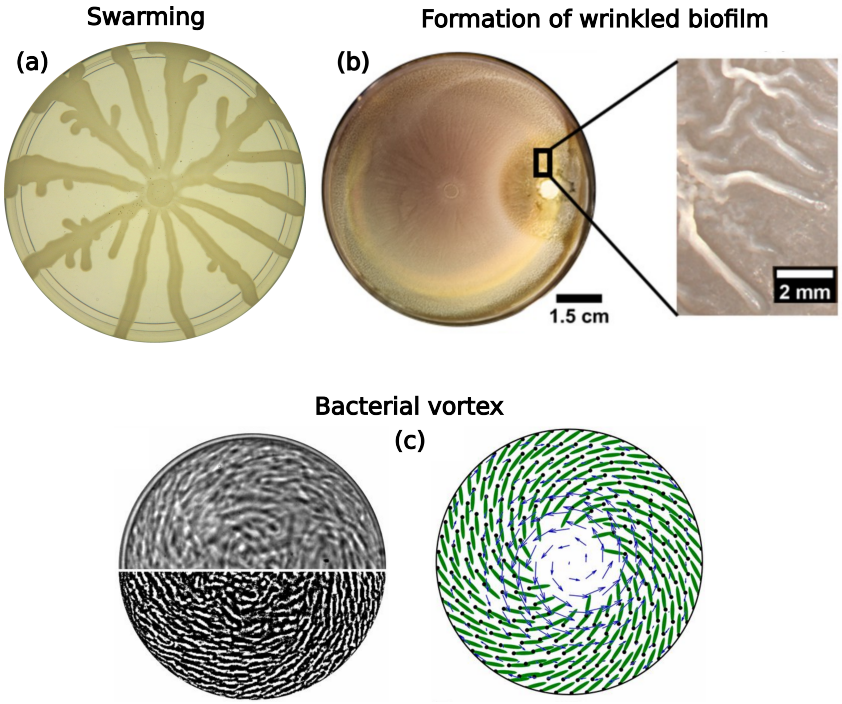

Figure 1.2: **Collective Behavior in Natural Microswimmers**: (a) Swarming behavior of *Pseudomonas aeruginosa* bacteria inoculated at the center of a nutrient-containing dish, migrating outward (source: Wikipedia). (b) Formation of wrinkled biofilm by *Bacillus subtilis* bacteria near antibiotic-rich regions (source: [22]). (c) Bacterial vortex observed in a confined dense suspension of *B. subtilis* bacteria (source: [26]).

1.3 | Microswimmers in liquid crystals

In the majority of the aforementioned studies, microswimmers were investigated in an isotropic medium. Now, the question is: What happens if the surrounding medium is anisotropic, such as the liquid crystal? Liquid crystals are unique since they can exhibit both positional and orientational order while retaining the ability to flow. In nematic liquid crystals, molecules align along a preferred direction known as the director. This directional molecular alignment introduces anisotropy in viscosity [30, 31, 32], affecting the dynamics of microswimmers.

Experimental evidence indicates that natural microswimmers, like bacteria, exhibit constrained behavior when immersed in a nematic liquid crystal. Because of elastic interactions with liquid crystal molecules, rod-like bacteria prefer to swim along the director [33, 34, 35, 36, 37, 38]. The majority of these studies have been conducted with rod-shaped bacteria in a liquid crystal environment. In this case, the elastic torque exerted on a bacterium is directly proportional to the angle between the director and the bacterium itself. Thus, the torque is minimum when the bacterium aligns parallel to the liquid crystal director. Now, what happens if there is no elastic torque on a microswimmer?

This question was answered in a simulation study that focused on the dynamics of a spherical microswimmer, or squirmer, moving within a nematic liquid crystal [39]. As shown in Figure 1.3b, the results suggested the presence of a hydrodynamic torque, which depends on the nature of the squirmer's flow field. If the squirmer has a pusher-like flow field, the torque aligns it parallel to the nematic director, and if the squirmer has a puller-like flow field, the torque aligns it perpendicular to the nematic director. This study provides an understanding of how the flow field of microswimmers couples with the anisotropic nature of liquid crystals and affects microswimmer dynamics.

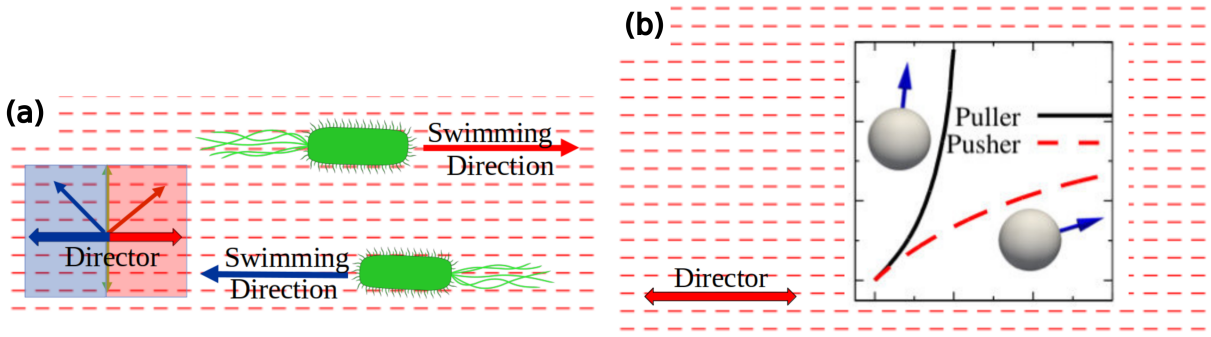

Figure 1.3: **Dominant torque on rod-like and spherical Microswimmers**: The sketch depicts the preferred swimming direction for rod-like and spherical particles in a liquid crystal environment (red lines indicate directors). (a) Elastic torque dominates for rod-like particles, resulting in a preferred alignment parallel to the director. (b) For spherical particles, where elastic torque is zero, the hydrodynamic torque determines the preferred swimming direction. A pusher-type spherical swimmer prefers to swim along the director, while a puller-like swimmer prefers to swim perpendicular to the director [39]. Inset in (b) is sourced from [39].

Flexibility and versatility are key features of a liquid crystal medium. In a typical experimental setup, bacteria are immersed within a lyotropic liquid crystal, which is then confined between two glass plates [40, 36, 41, 37]. Planar anchoring is applied at the glass surfaces, setting the nematic director to align parallel to the surface. Due to the long-range orientational property of nematic liquid crystals, the director in the bulk also aligns parallel to the surface. Nevertheless, the surfaces can be treated to induce homeotropic anchoring, compelling the director to be perpendicular to the surfaces. As the rod-like bacteria tend to align with the nematic director, leveraging anchoring effects

can allow us to engineer systems with liquid crystals, to guide microswimmers in specific directions [41, 37, 42].

1.3.1 | Collective phenomena in liquid crystal environment

Unipolar motion in patterend liquid crystal

One strategy for guiding microswimmers within liquid crystals is to use a patterned director field. Several experimental studies in this area have unveiled interesting phenomena [41, 35, 37, 36]. To this end, a noteworthy contribution comes from the study conducted by Chenhui Peng and colleagues [37]. In their experiments, the bacteria, *B. subtilis*, were introduced into a liquid crystal environment with a spatially varying director field. When the director field had either a pure bend or a pure splay, the swimming of bacteria was observed to be bipolar (Figure 1.4(a)-(d)). However, when a mixed bend-splay pattern was introduced, above a critical volume fraction, the bacteria showed unipolar swimming (shown in Figure 1.4 (e)-(g)). This finding suggests that the collective effect of the bacterial population can overcome elastic forces within liquid crystals and can influence the dynamics of microswimmers.

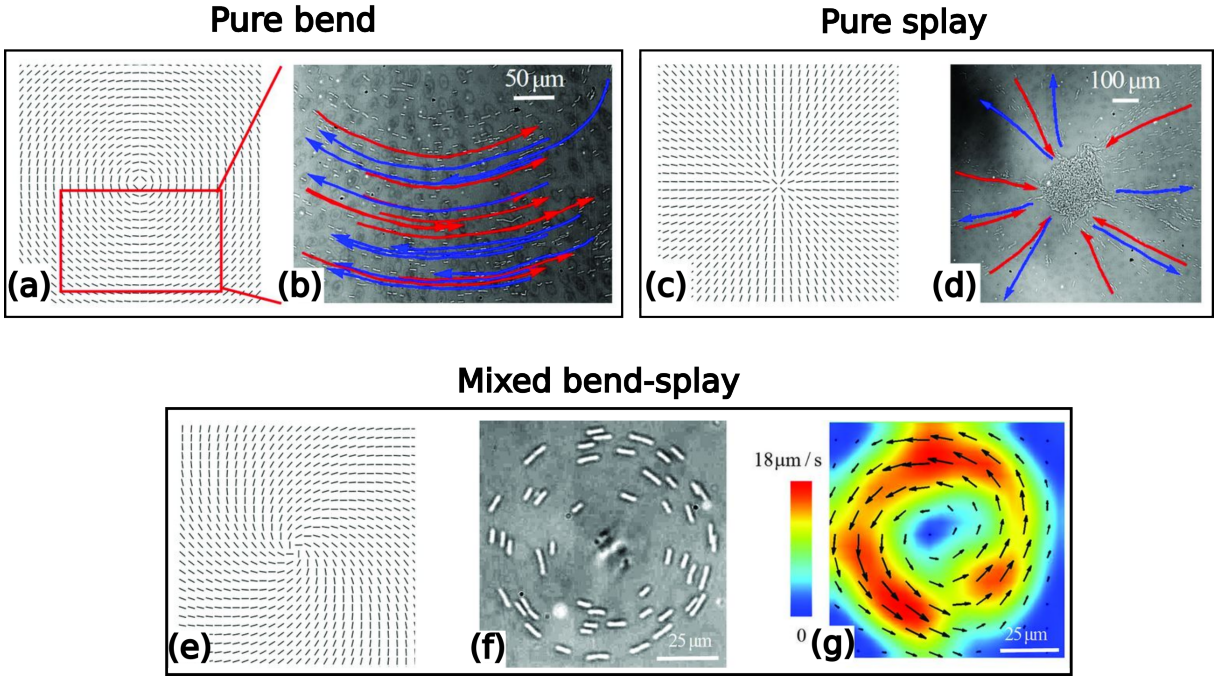

Figure 1.4: **Bacteria in patterned liquid crystal environment**: *Bacillus subtilis* bacteria immersed in liquid crystal with a patterned director field. (a) Director field with a pure bend pattern. (b) Bipolar motion of bacteria observed within regions with a pure bend pattern (arrows represent the direction of motion). (c) Director field with a pure splay pattern. (d) Bacteria follow the local director in a bipolar fashion and aggregate at the center of the splay pattern. (e) Director field with a mixed bend-splay pattern. (f) Above a critical concentration, bacteria exhibit unipolar motion in regions with a mixed bend-splay pattern. (g) Map of bacterial velocities. All figures are taken from [37].

Emergence of instabilities in 2D LLCs

Another study highlighting the importance of collective effects in microswimmers' dynamics is an experimental work done by Shuang Zhou and colleagues [40]. They introduced a new term "Living Liquid Crystals" or LLCs, to represent any system where motile bacteria are immersed within a water-based, nontoxic liquid crystal. Experiments with LLCs revealed that swimming bacteria influence the long-range nematic ordering within the liquid crystal [40, 41]. Moreover, beyond a critical activity, the uniform alignment of the director field becomes unstable, and a periodic stripe pattern emerges (shown in Figure 1.5(c)-(d)). At even higher activity, this periodic pattern vanishes and defects appear in the system (see Figure 1.5 (e)-(f))

LC experiments suggest that beyond a critical activity, the long-range nematic alignment in LLCs becomes unstable [40]. This instability arises from the coupling between the microswimmer's flow field and the liquid crystal's orientational order, leading to spatiotemporal director patterns. These instabilities were absent in the LLC realized by C. Peng et al. [37], as unipolar bacterial motion (Figure 1.4 (e)-(g)) was observed at a significantly lower concentration [37] than the critical threshold reported in [40] for instabilities.

1.4 | Active nematics

Another class of active suspensions with nematic order is known as active nematics [43]. In this class, the constituent rod-like particles are non-motile, yet they have the capability to generate flow fields around them. Examples of active nematics include suspensions of microtubule filaments and kinesin motors [44, 45, 46], and suspensions of actin filaments [47]. In a uniformly ordered active suspension or active nematic system, particle-generated flows cancel out each other [48]. A linear stability analysis of such suspensions in 2D, suggests that a bend fluctuation will grow if the flow generated by the particles is of an extensile type [49]. Conversely, a splay fluctuation will grow if the flow generated by the particles is of a contractile type [49]. However, director deformations induced by hydrodynamic instabilities frequently lead to the formation of defects [50, 43], a state commonly referred to as active turbulence.

As shown in Figure 1.5 (g)-(f), experiments conducted with extensile active nematics, such as microtubule-kinesin suspensions confined in two dimensions, have shown active turbulence [44, 43]. This observation is further supported by numerical simulations [50]. Given the fundamental similarity between an active nematic system and a suspension of motile bacteria in a liquid crystal, both systems should exhibit similar hydrodynamic instabilities. In LLCs, *B. subtilis* bacteria were suspended in a liquid crystal medium [40]. These bacteria are "pushers" and generate extensile-type flow fields [51, 28, 52]. Consequently, the most unstable mode of director deformation is predicted to be bend [49].

Indeed, as the activity increases, the LLC shows wave patterns (see Figure 1.5 (c)-(d)) reminiscent of bend deformations and the nucleation of defects (Figure 1.5 (e)-(f)) Figures (a)-(f) are taken from [40], Figure (g) is sourced from [44].

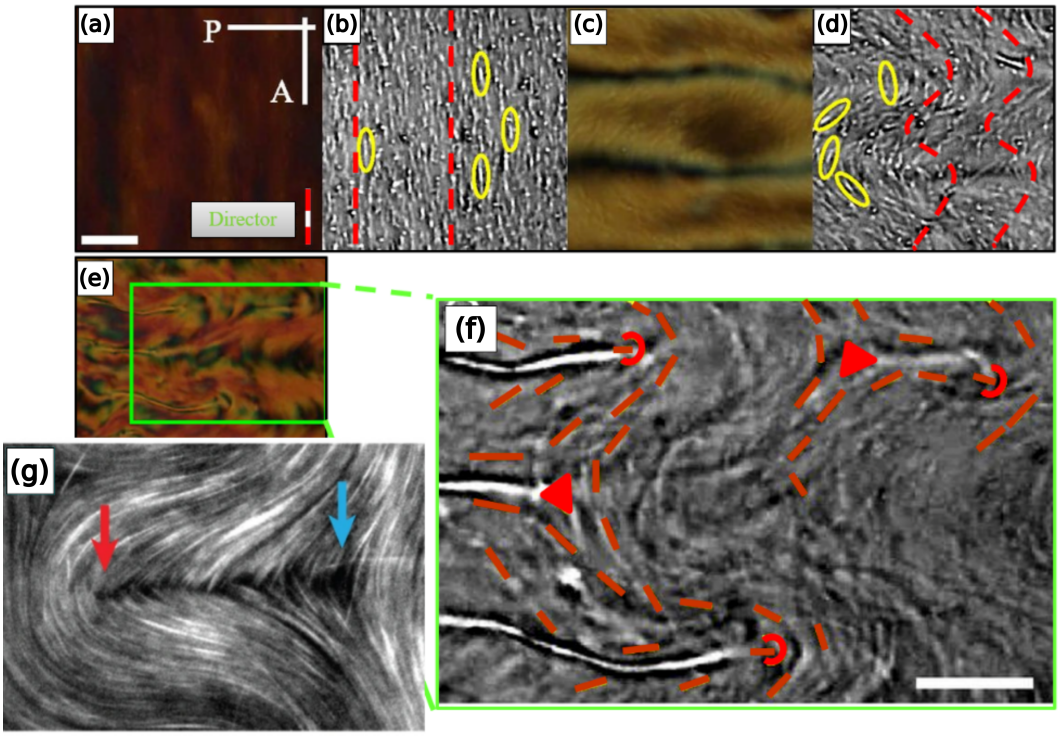

Figure 1.5: **Emergence of hydrodynamic instabilities**: The figure illustrates the presence of hydrodynamic instabilities in active ordered suspensions. Figures (a)-(f) showcase spatiotemporal pattern formations resulting from hydrodynamic instabilities in LLCs [40]. (a)-(b) Inactive bacteria (yellow ellipses) align parallel to the nematic director (depicted in red). (c)-(d) Active bacteria generate a periodic stripe pattern. (e)-(f) Higher bacterial concentration leads to the appearance of $\pm 1/2$ defects in LLCs. (g) A 2D active nematic system of microtubule-kinesin suspension forms $\pm 1/2$ defects (red and blue arrows) [44, 43].

The majority of experimental studies on active nematics have primarily been conducted in a 2D setup [44, 47]. Nonetheless, numerical simulations have shown that introducing a third dimension can significantly impact turbulence in extensile active nematics [53, 54, 55]. In quasi-2D environments, active turbulence is characterized by straight disclination lines, while in 3D, the disclination lines become contorted [53, 54, 56, 57, 58]. These results suggest the presence of twist deformations in the nematic director field. Moreover, linear stability analysis in 3D settings has predicted that twist-bend deformations grow in extensile active nematics [55].

1.5 | Thesis overview

The primary objective of the thesis is to understand how hydrodynamic coupling between microswimmer flow fields and liquid crystalline elasticity influences the nematic order in liquid crystals. Our system consists of spherical microswimmers in nematic liquid crystals. The self-propulsion for microswimmers is described by surface slip velocity as per the squirmer model. The simulations have been performed using the *Ludwig* code [59], which employs a hybrid Lattice Boltzmann algorithm to solve the relevant hydrodynamic equations of the liquid crystal and microswimmers.

1.6 | Thesis outline

Next in the thesis, Chapter 2 discusses different types of liquid crystal phases and the concept of the Landau-de Gennes free energy. Chapter 3 introduces the squirmer model for microswimmers. Chapter 4 briefly discusses the hydrodynamic equations governing the system of microswimmers and nematic liquid crystal suspensions. Chapter 5 investigates the system confined to a quasi-2D space, focusing on the emerging bend-dominated instability. Chapter 6 explores the system without any spatial constraints, in 3-dimensions, showcasing a transition to a cholesteric-like state. Finally, Chapter 7 examines how an individual microswimmer behaves in patterned nematics and investigates the potential of entangled topological defects in cargo transport.

Chapter 2

Liquid crystal

In this chapter, various types of liquid crystal phases are briefly discussed, with a focus on nematic and cholesteric phases. Next, different types of deformations in the nematic director field are introduced. And the corresponding elastic free energy according to the Oseen-Frank formalism is discussed. Following that, the concept of the **Q**-tensor order parameter and the Landau-de Gennes free energy is explained. The contributions from bulk, elastic deformations, and the surface effects are discussed. Finally, the chapter concludes by discussing a mapping between the elastic energies of the Oseen-Frank and Landau-de-Gennes free energies.

2.1 | Introduction

There are several states of matter, including solid and liquid. However, certain materials exhibit an intermediate state between these two, known as the liquid crystalline state [60]. This state was first observed in 1888 by Friedrich Reinitzer while examining the physical properties of a compound named cholesteryl benzoate [61, 62]. He noted that the compound had two different melting points [60, 61]. At the first melting point, the solid crystalline form transformed into a cloudy liquid, and then at the second melting point, the cloudiness vanished, and the liquid became clear (see Figure 2.1). Later, Otto Lehman, a German physicist, examined this cloudy fluid under a microscope and reported the presence of crystal-like ordering between molecules [63, 62]. Subsequently, this cloudy liquid was termed "liquid crystal" as it possessed characteristics of both liquids, such as fluidity, and solids, including long-range order [60, 62]. Usually, materials with anisotropic molecular shapes, such as disc-like, cone-like, or rod-like, exhibit the liquid crystalline state [60]. In liquid crystals, the anisotropy in molecular shape causes orientational ordering, ultimately leading to anisotropic physical properties [60]

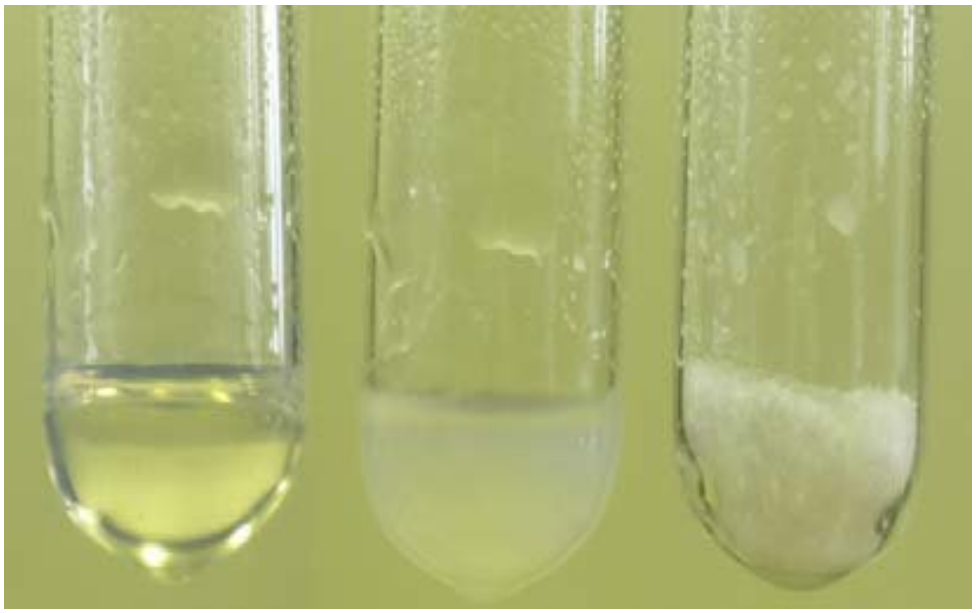

Figure 2.1: **Cholesteryl benzoate phases**: The image displays three phases of cholesteryl benzoate observed in experiments [64]. On the left, the isotropic fluid phase is characterized by a clear liquid; in the middle, the liquid crystalline phase exhibits a cloudy appearance; and on the right, the solid phase resembles white powder. The figure is sourced from [64].

2.1.1 | Thermotropic and lyotropic liquid crystals

Depending on how the liquid crystalline phase is induced, the liquid crystals can be classified into two broad categories: thermotropic liquid crystals and lyotropic liquid crystals [60].

Thermotropic liquid crystals

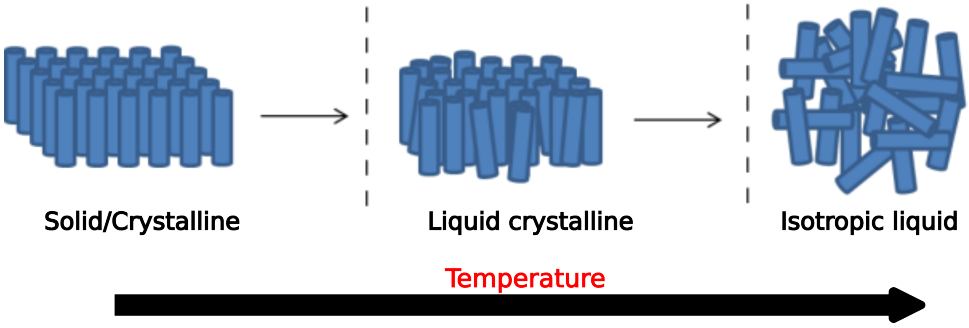

Figure 2.2: **Molecular arrangement in thermotropic liquid crystal**: The sketch illustrates the molecular arrangement of rod-like molecules (blue colored) in solid, liquid crystalline and isotropic fluid phases of a thermotropic liquid crystal material [65]. As the temperature increases, the molecular ordering decreases.

When the liquid crystal phase is achieved by changing the temperature, those liquid crystals are referred to as thermotropic. The molecular orientations in these compounds

are influenced by temperature changes, as illustrated in Figure 2.2. Cholesteryl benzoate, shown in Figure 2.1, is an example of thermotropic liquid crystal [64]. Another example is pentylcyanobiphenyl, popularly known as 5CB.

Thermotropic liquid crystals are further classified based on whether mesophases (intermediate phases between liquid and solid) appear on both sides of the temperature change. If the liquid crystalline phase can be induced by both, decreasing and increasing the temperature of the compound, then these thermotropic liquid crystals are known as 'enantiotropic' [66]. Some thermotropic liquid crystals lack this reversibility of phase transition; they can reach the liquid crystalline phase through unidirectional temperature change. These are referred to as 'monotropic' [66].

Lyotropic liquid crystals

Lyotropic is a class of liquid crystals where the liquid crystalline phase is induced by dissolving specific anisotropic materials in a suitable solvent. Unlike thermotropic liquid crystals, the long-range ordering in lyotropic liquid crystals is influenced by the change in concentration of the dissolved particles rather than change in temperature. An example of lyotropic liquid crystal material is disodium cromoglycate (DSCG). In aqueous solution, DSCG exhibits a nematic phase even at room temperature [67]. An advantage of lyotropic liquid crystals is their non-toxicity to biological organisms [68]. For instance, Living Liquid Crystals (LLCs) are solutions of bacterial populations within a lyotropic liquid crystal [40]. Experiments with LLCs have provided valuable insights into the dynamics of microswimmers within an anisotropic liquid crystal environment [40, 41, 37, 42].

2.2 | Liquid crystal phases

The materials showing liquid crystalline phase have molecules with anisotropic shapes, like rods, discs, or cones. The thermotropic liquid crystals with rod-like constituent molecules can be classified into three types: nematic, smectic, and cholesteric [60].

2.2.1 | Nematic phase

In the nematic phase (shown in Figure 2.3), rod-like molecules align themselves along a specific direction called the director, denoted by a unit vector $\hat{\mathbf{n}}$. In this phase, molecules exhibit long-range orientational ordering but no positional ordering. The centers of gravity of the molecules are randomly distributed (as in the isotropic liquid phase).

The optical properties of any material are influenced by the preferential alignment of the molecules. A uniaxial nematic liquid crystal is birefringent [60]; that is, the refractive index along the director is different from the refractive index perpendicular to the director.

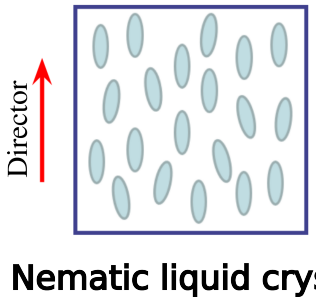

Figure 2.3: **Nematic phase**: The figure illustrates the alignment of rod-like molecules (depicted in cyan) in the nematic liquid crystal. The average molecular orientation is indicated by the director $\hat{\mathbf{n}}$ (represented by the red arrow).

The nematic phase is apolar; the molecules show no preference for aligning parallel or antiparallel to the director, resulting in the head-tail symmetry in the director ($\hat{\mathbf{n}} = -\hat{\mathbf{n}}$). Nematic liquid crystal molecules are responsive to external fields, allowing their average orientation to be controlled by applying either magnetic or electric field [60]. This characteristic, combined with the ability of liquid crystals to influence light polarization, forms the basis of liquid crystal display (LCD) technology.

2.2.2 | Cholesteric phase

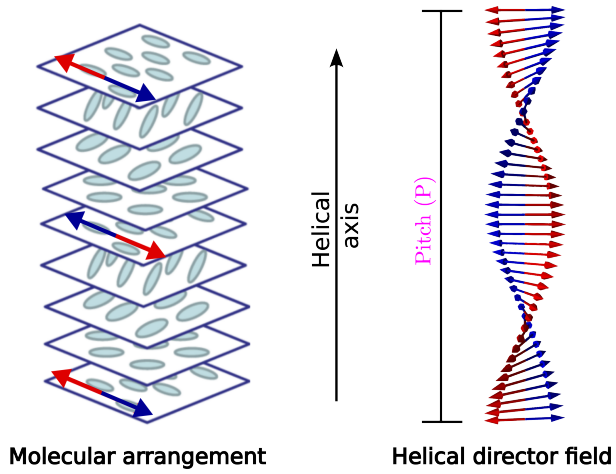

Figure 2.4: **Cholesteric phase**: The sketch illustrates the molecular alignment of rod-like molecules (depicted in green) in the cholesteric phase. Within each layer, the molecules have a nematic arrangement, with the director represented by the double-sided arrow. These directors undergo rotation along the direction of layer stacking, giving rise to the helical director field (on right-side), characteristic of the cholesteric phase. The nematic planes are drawn for better illustration, they don't have any specific physical meaning.

The cholesteric phase was first observed by Friedrich Reinitzer, while he was working with cholesterol derivatives from plants [61]. That's why this phase is called 'cholesteric' [62].

In this phase, molecules align their long axes in a helical pattern [60], as shown in Figure 2.4. This phase is exclusive to compounds with chiral molecules (they can't overlap with their mirror images) [60].

To schematically understand the cholesteric phase (Figure 2.4), one can consider a layer of molecules in the nematic phase. Now, add another layer on top, tilting its director by an angle relative to the previous layer. Repeat until the nematic directors align. Because the molecules are 'nematically' arranged in a layer, the cholesteric phase is also known as twisted nematic or chiral nematic phase. Each layer's director rotates by a fixed angle, creating a helical arrangement of directors. The axis perpendicular to the directors is called the helical axis. The distance over which the director rotates by 2π is the chiral pitch length P (see Figure 2.4).

The pitch of a cholesteric liquid crystal changes with the temperature and can also be altered by adding chiral dopants [69]. A property of the cholesteric phase is the selective reflection of light based on its helical structure. It can lead to the display of colors due to constructive interference of specific wavelengths [60]. This phenomenon is utilized in various applications, including reflective displays and color-changing materials [69].

Twisted director fields

Our simulation results in Chapter 6 reveal a transition in the liquid crystal state, from a nematic to a cholesteric-like state. To understand our results better, we introduce a measure, termed as the tilt angle (α). It is the angle between the director and the helical axis, as shown in Figure 2.5. It is important to remember that α can have values within range $[0, \pi/2]$. In the cholesteric phase the tilt angle $\alpha = 90°$.

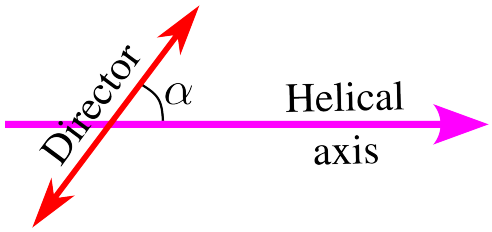

Figure 2.5: **Definition of the tilt angle**: the figure depicts the definition of the tilt angle, denoted by α, for a cholesteric liquid crystal. α represents the angle between the helical axis (depicted by the pink arrow) and the director (red).

In a cholesteric state, if the helical axis aligns with the x-axis, and the tilt and pitch are denoted by α and P respectively, then the helical/twisted director field $\hat{\mathbf{n}}(\mathbf{r})$ is expressed as follows:

$$\hat{\mathbf{n}}(\mathbf{r}) = (\cos\alpha,\ \sin\alpha\cos qx,\ \pm\sin\alpha\sin qx) \tag{2.1}$$

where $\pm$ corresponds to left and right handed twists, $q = 2\pi/\mathrm{P}$, and x signifies the x-coordinate. One can visualize the twisted director field of the cholesteric phase using

$\alpha = \pi/2$ in Equation 2.1. The simulation package used in this thesis, called *Ludwig* [59], uses Equation 2.1, to initialize the liquid crystal in a cholesteric phase. In Figure 2.6, we present the helical director field for a cholesteric phase, with the helical axis chosen along $\hat{x}$ and the pitch, P = 128, in lattice units (LU).

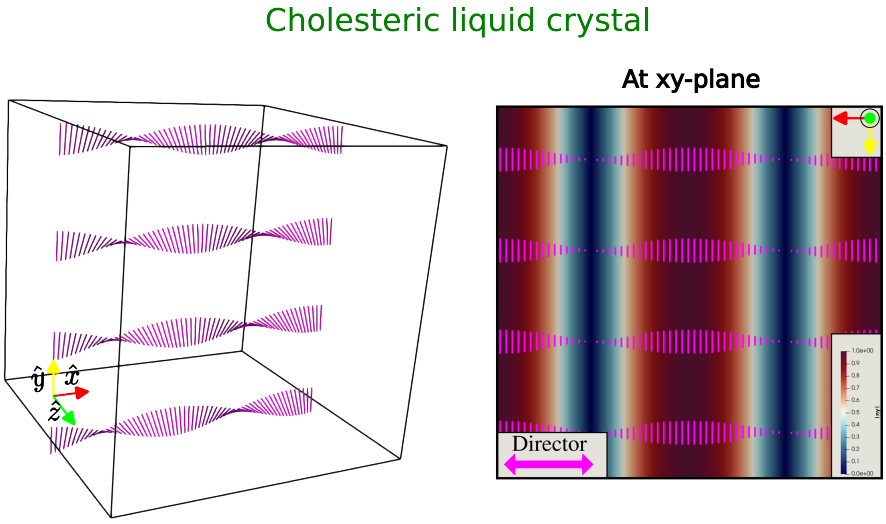

Figure 2.6: **Cholesteric liquid crystal director field**: The figure visualizes the director field of cholesteric liquid crystal, created using the simulation package *Ludwig*. The twisted director field is based on Equation 2.1, with a tilt angle of $\alpha = 90°$ and pitch P = 128 LU. The pitch length is equal to the box length. On the left, the 3D simulation box is presented with directors (colored in pink). In the right figure, the director field is visualized at a xy-plane, with the color bar representing the absolute value of the director component along y-axis, denoted as $|n_y|$.

It is also possible to have $\alpha < \pi/2$ while still maintaining a helical structure, as shown in Figure 2.7. But, a helical structure with zero tilt is not possible. When $\alpha = 0$, the directors align perfectly parallel to each other, resulting in nematic configuration. In the nematic phase the tilt is zero and pitch is taken as infinity.

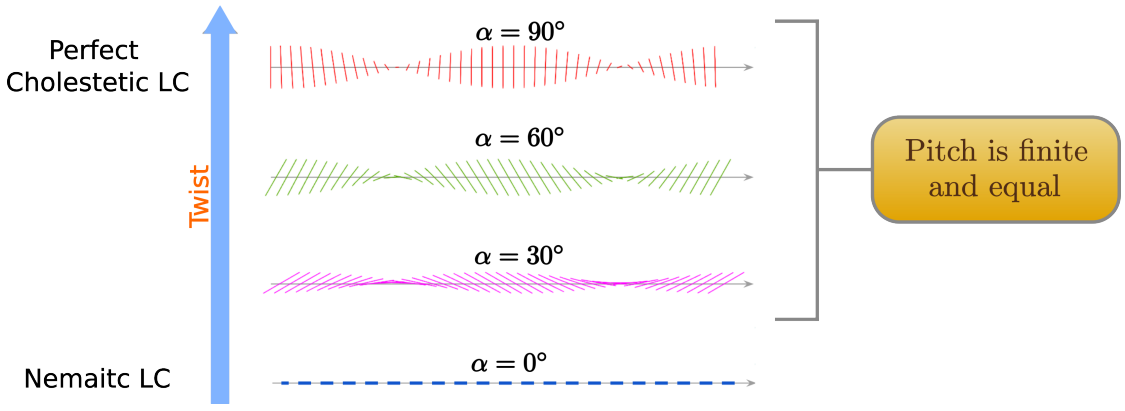

Figure 2.7: **Tilt angle and the helical structure:** Illustration of helical director field, $\hat{\mathbf{n}} = (\cos\alpha, \sin\alpha\cos qx, \pm\sin\alpha\sin qx)$, corresponding to various tilt angle (α). At $\alpha = 90°$, the helix corresponds to a cholesteric phase. For tilt angles less than 90 degrees, the helical structure is cholesteric-like but not cholesteric. The nematic phase has zero tilt and infinite pitch. The left side bar represents the amount of twist (T) deformations in the helical structure, which scales as $T \sim \sin^2\alpha$. The twist is maximum in the cholesteric phase and minimum in the nematic phase.

2.2.3 | Smectic phases

Smectic phases are more ordered than the nematic phase, in the sense that in addition to the orientational order, the smectic phases also have positional order [60]. The positional ordering comes from the arrangement of the molecules in a layered structure, as shown in Figure 2.8. In these phases, the molecular centers of mass are correlated and are organized in clearly defined planes. Within each layer, the molecules are oriented in a particular direction and have the freedom to move freely. Moreover, the layers themselves can slide over one another. This combination of layer sliding and intralayer molecular movement contributes to the fluid-like behavior observed in the smectic phase.

Typically, the smectic phases are observed at lower temperatures compared to the nematic phase. The smectic phases contain up to 12 different phases, with Smectic-A (SmA) and Smectic-C (SmC) being the most common [60]. In SmA, the average orientation of the molecular long axes (the director) is perpendicular to the layer. While in SmC, molecules within each layer are tilted, resulting in the director being inclined at an angle relative to the plane's normal.

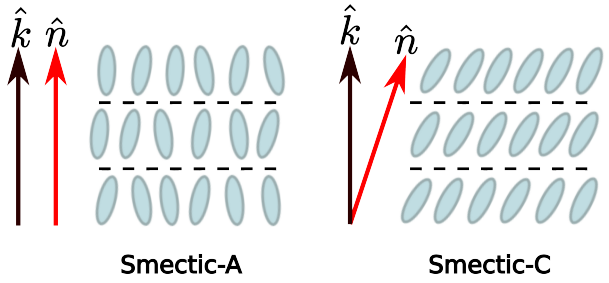

Figure 2.8: **Smectic phases**: The figure illustrates the layered structures in smectic phases. In Smectic-A (SmA), molecules align parallel to the plane normal (depicted by black arrow), resulting in the director (red arrow) being parallel to the plane normal. In Smectic-C (SmC), the molecules are tilted relative to plane normal.

2.2.4 | Blue phases

Finally, I would like to mention the blue phases (BPs). These phases are unique to cholesteric liquid crystals with chiral molecules. Reinitzer first observed blue phases in 1888 [61], and due to their vibrant blue appearance under a polarizing microscope, they were named 'blue phases'. Although, these phases do not always have blue appearance. Blue phases can only be observed between the cholesteric and the isotropic fluid in a very narrow temperature range ($0.5° - 1°$) [70]. They are classified into three sub-phases: BPI, BPII, and BPIII. BPIII has molecular ordering similar to the isotropic phase [71]. In blue phases, molecules form helices, but unlike the cholesteric phase, they twist in two dimensions, creating a double-twist (see Figure 2.9). Similar to the cholesteric phase,

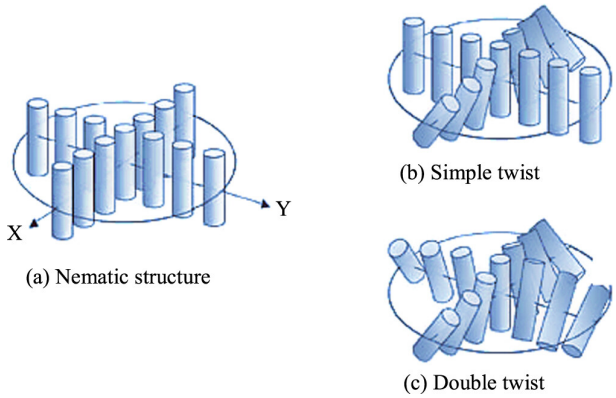

Figure 2.9: **Single and double twist structure**: The sketch shows the difference between single-twist structure found in cholesteric phase and double-twist structure found in blue phases. The figures are taken from [72].

blue phases can selectively reflect visible light, making them potentially useful in optical devices like liquid crystal displays (LCDs). However, the main limitation is the narrow temperature range in which blue phases exist. Efforts are underway to expand this range by incorporating polymers or nanoparticles [73].

2.3 | Oseen-Frank elastic free energy

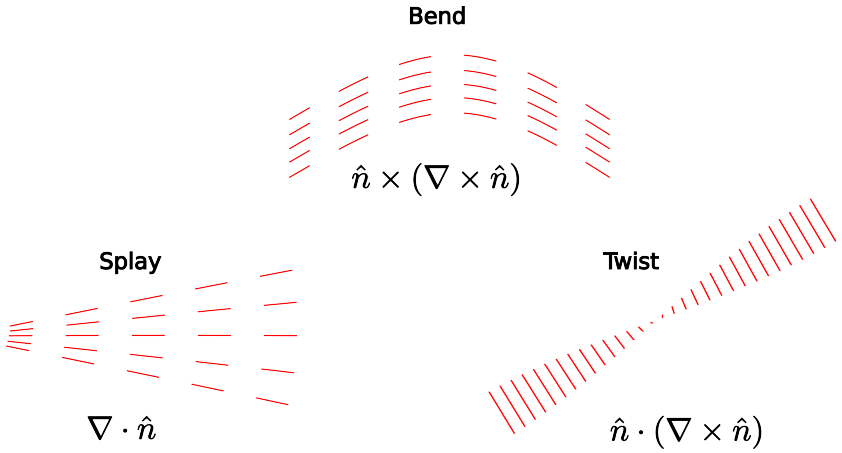

Figure 2.10: **Deformations in the nematic director field:** The sketch illustrates various types of deformations in the nematic director field $\hat{\mathbf{n}}(\mathbf{r})$. In the Oseen-Frank formalism, bend deformations can be calculated using $\hat{\mathbf{n}} \times (\nabla \times \hat{\mathbf{n}})$, twist deformations using $\hat{\mathbf{n}} \cdot \nabla \times \hat{\mathbf{n}}$, and splay using $\nabla \cdot \hat{\mathbf{n}}$.

In uniaxial nematic liquid crystals, the directors align perfectly parallel to each other, and any deformation in the director field adds an extra energy cost to the total free energy. Three fundamental deformations or distortions, are splay, bend, and twist, which are shown in Figure 2.10. These distortions contribute to the total free energy through the elastic free energy. The Oseen-Frank formalism provides a framework to evaluate the elastic free energy density using the director field $\hat{\mathbf{n}}(\mathbf{r})$.

In Oseen-Frank formalism, for the uniaxial nematic liquid crystal with a director field $\hat{\mathbf{n}}(\mathbf{r})$, the elastic free energy density $F^{\mathrm{OF}}_{\mathrm{elastic}}$ is expressed as [74]

$$\begin{aligned} F^{\mathrm{OF}}_{\mathrm{elastic}} = & \frac{1}{2}K_{11}(\nabla\cdot\hat{\mathbf{n}})^2 + \frac{1}{2}K_{22}(\hat{\mathbf{n}}\cdot\nabla\times\hat{\mathbf{n}})^2 + \frac{1}{2}K_{33}(\hat{\mathbf{n}}\times(\nabla\times\hat{\mathbf{n}}))^2 \\ & - K_{24}\nabla\cdot[\hat{\mathbf{n}}(\nabla\cdot\hat{\mathbf{n}}) + \hat{\mathbf{n}}\times(\nabla\times\hat{\mathbf{n}})] \end{aligned} \tag{2.2}$$

Here, K_{11}, K_{22}, and K_{33} represent the elastic constants for splay, twist, and bend distortions, respectively [60]. The elastic constant K_{24} accounts for the fourth type of distortion known as "biaxial splay".

2.4 | Q-tensor order parameter

An order parameter quantifies the degree of order or symmetry in a physical system. Since the isotropic phase is less ordered than the nematic phase, one can define an order parameter that is zero in the isotropic phase and non-zero in the nematic phase.

In a liquid crystal composed of rod-like molecules, the order parameter is represented by a symmetric, traceless tensor known as the **Q**-tensor. In the uniaxial nematic phase with a director $\hat{\mathbf{n}}$, the **Q**-tensor is defined as:

$$\boxed{Q_{\alpha\beta} = \frac{3s}{2}\left(n_\alpha n_\beta - \frac{1}{3}\delta_{\alpha\beta}\right)} \tag{2.3}$$

Here, Greek indices represent Cartesian components, and summation over repeated indices is implied. Consider a scenario where the preferred alignment is along the x-axis. Using the above equation, the **Q**-tensor can be written as:

$$\mathbf{Q} = \begin{pmatrix} s & 0 & 0 \\ 0 & -\frac{s}{2} & 0 \\ 0 & 0 & -\frac{s}{2} \end{pmatrix}$$

Since we assumed the nematic phase to be uniaxial, the **Q**-tensor has only two independent eigenvalues: s and $-s/2$. The absolute largest eigenvalue, denoted as s, is called the scalar order parameter, and the associated eigenvector determines the director $\hat{\mathbf{n}}$. The scalar order parameter s measures the degree of molecular alignment along $\hat{\mathbf{n}}$ and is defined as follows:

$$s = \frac{1}{2}\left\langle \cos^2\theta - \frac{1}{3}\right\rangle \tag{2.4}$$

Here, angular brackets represent the spatial average, and θ denotes the angle between the molecular long axes and the director. In the case of randomly oriented molecules, such as in an isotropic fluid, $\langle\cos^2\theta\rangle = \frac{1}{3}$, resulting in $s = 0$. Conversely, when molecules are perfectly aligned, $\langle\cos^2\theta\rangle = 1$, and $s = 1/3$.

The **Q**-tensor contains information about the scalar order parameter as well as the director. Also, **Q** can vary in space and time, in the simulations. At each time step, **Q** can be diagonalized. Consequently, the largest absolute eigenvalue provides the scalar order parameter s, and the corresponding eigenvector gives the director $\hat{\mathbf{n}}$.

2.5 | Landau-de Gennes free energy

The transition from the isotropic to the nematic phase is governed by changes in the free energy of the liquid crystal material. The phase characterized by the lowest free energy becomes the stable phase under specific conditions. Various approaches have been made to describe nematic-isotropic transitions, such as Onsager density functional theory and Maier-Saupe mean-field theory [60]. However, in this section, our focus is on a phenomenological theory (without knowing molecular details) known as Landau-de Gennes theory [60].

This theory proposes that the free energy density near the transition temperature can be described through a power series expansion in terms of the order parameter **Q** and its spatial gradients. For a uniaxial nematic phase with spatially invariant **Q**, the free energy density is due to the bulk contribution:

$$F_{\text{bulk}} = \frac{A_0}{2}\left(1 - \frac{\gamma}{3}\right) Q_{\alpha\beta}^2 - \frac{A_0\gamma}{3} Q_{\alpha\beta}Q_{\beta\gamma}Q_{\gamma\alpha} + \frac{A_0\gamma}{4}(Q_{\alpha\beta}^2)^2 \tag{2.5}$$

Here, A_0 is a constant, and $Q_{\alpha\beta}^2$ represents $Q_{\alpha\beta}Q_{\alpha\beta}$. The temperature dependence is introduced through the parameter γ, which also determines the scalar order parameter s,

$$s = \frac{1}{6} + \frac{1}{2}\sqrt{1 - \frac{8}{3\gamma}}$$

If **Q**-tensor varies in space, an additional elastic term contributes to the free energy density. Under the one elastic constant approximation, it can be written as:

$$F_{\text{elastic}} = \frac{K}{2}(\partial_\gamma Q_{\alpha\beta})^2 \tag{2.6}$$

Here, K is the elastic constant. A non-zero gradient in the order parameter indicates deformations in the nematic director field (see Figure 2.10). For a cholesteric liquid crystal, the elastic contribution is modified to account for the twist in the director field. For a cholesteric phase with a helical pitch length P_0 and $q_0 = 2\pi/\mathrm{P}_0$, the elastic contribution is given by:

$$F_{\text{elastic}} = \frac{K}{2}\left((\partial_\gamma Q_{\alpha\beta})^2 + (\epsilon_{\alpha\gamma\delta}\,\partial_\gamma Q_{\delta\beta} + 2\,q_0\,Q_{\alpha\beta})^2\right) \tag{2.7}$$

Here, $\epsilon_{\alpha\gamma\delta}$ is the Levi-Civita symbol.

2.5.1 | Surface contributions to free energy density

Experiments with nematic liquid crystals are often conducted in confined environments [40, 42, 37, 32]. When the liquid crystal is near a solid surface, molecular interactions between the surface and the liquid crystal molecules can influence the director orientation. This holds true for various surfaces, including colloids [75, 76]. The nature of these interactions decides the preferred orientations of liquid crystal molecules near the interface, and due to the long-range orientational property of liquid crystals, these effects extend into the bulk. This is known as surface anchoring.

Surface anchoring involves modifying the chemical or physical properties of the surface to induce a preferred orientation for the liquid crystal molecules [77, 78, 79]. Types of surface anchoring include homeotropic anchoring, where molecules align perpendicular to the surface, and degenerate planar anchoring, where molecules lie parallel to the surface. For simulations involving walls or colloids with surface anchoring effect, the Landau free energy density has an additional surface term, which is generally expressed as:

$$F_s = \frac{1}{2} W_0 (Q_{\alpha\beta} - Q^0_{\alpha\beta})^2 \tag{2.8}$$

Here, W_0 denotes the anchoring strength, and $\mathbf{Q^0}$ represents the preferred tensor order parameter at the surface, which can be set to induce either homeotropic or planar anchoring (for examples, see [80]). The surface term F_s reaches its minimum when the director field aligns with the preferred orientation, given by $\mathbf{Q^0}$.

2.5.2 | Mapping between Frank and de Gennes elastic free energy

In our simulations, the $\mathbf{Q}$-tensor is initialized for the uniaxial nematic liquid crystal, using Equation 2.3. At each time step, the total free energy density is evaluated according to the Landau-de Gennes formalism. The bulk and elastic contributions are calculated using Equation 2.5 and Equation 2.6, respectively. If there are any walls or particles with a surface anchoring effect, the surface energy contribution is also included in total free energy using Equation 2.8.

However, calculating elastic free energy using Landau formalism has one drawback. The elastic energy consolidates contributions from twist, bend, splay, and biaxial splay into a single term $\sim \frac{K}{2}(\partial_\gamma Q_{\alpha\beta})^2$; thus, one cannot calculate the individual contributions from different deformations.

To address this issue, we shift our attention to the Oseen-Frank formalism. In this case, under a single elastic constant approximation, the elastic energy reads,

$$F^{\mathrm{OF}}_{\mathrm{elastic}} = \frac{1}{4} K\, S^2 + \frac{1}{4} K\, T^2 + \frac{1}{2} K |\mathbf{B}|^2 + \frac{1}{2} K \mathrm{Tr}(\mathbf{\Delta}^2) \tag{2.9}$$

where the splay S, bend $\mathbf{B}$, and twist T deformations are defined as:

$$S = \nabla \cdot \hat{\mathbf{n}} \qquad T = \hat{\mathbf{n}} \cdot (\nabla \times \hat{\mathbf{n}}) \qquad \mathbf{B} = \hat{\mathbf{n}} \times (\nabla \times \hat{\mathbf{n}}) \tag{2.10}$$

and the $\mathbf{\Delta}$ in Equation 2.9 is the biaxial splay deformation, which is defined by a symmetric traceless tensor [81].

While Equations 2.9 and 2.10 can be used to calculate the magnitudes of different distortions and their corresponding energies, it would be advantageous in our simulations to calculate the distortions directly from the $\mathbf{Q}$-tensor. To achieve this, we use the formalism proposed by Selinger [81]. In this approach, the distortions are calculated using a special tensor $\mathbf{q}$, which is related to $\mathbf{Q}$ as follows:

$$q_{ij} = \frac{1}{3}\left(\delta_{ij} + \frac{2Q_{ij}}{s}\right) \tag{2.11}$$

here, s represents the scalar order parameter of the nematic liquid crystal. Due to the inherent ambiguity in defining the splay scalar uniquely in terms of q_{ij}, a splay vector $\mathbf{S} = S\hat{\mathbf{n}}$ is introduced [81], and the distortions are given by:

$$S_i = q_{il}\partial_j q_{jl} \qquad T = \epsilon_{ijk} q_{il}\partial_j q_{kl} \qquad B_k = -q_{il}\partial_i q_{kl} \tag{2.12}$$

We use these expressions to calculate $|\mathbf{S}|$, $|T|$, and $|\mathbf{B}|$, representing the magnitudes of splay, bend, and twist deformations, respectively.

From *Ludwig* code [59], the output is a $\mathbf{Q}$-tensor field. These tensors can be diagonalized to extract the eigenvalues and eigenvectors. At each lattice point, the nematic director is determined by taking the eigenvector corresponding to the highest absolute eigenvalue. Subsequently, we reconstruct the $\mathbf{Q}$-tensor using Equation 2.3. Then, we construct the $\mathbf{q}$-tensor using Equation 2.11, and calculate distortions using Equation 2.12.

Chapter 3

Microswimmer model

The aim of the thesis is to understand the collective effects of microswimmers within a nematic liquid crystal. This chapter discusses the squirmer model, which is employed to simulate the dynamics of the swimmers. The following chapter introduces the simulation model for the nematic liquid crystal.

3.1 | Introduction

Microswimmers generate flow fields to propel themselves in the surrounding fluid. There are a variety of mechanisms by which these flow fields are generated. For instance, bacteria like *Escherichia coli* have specialized hair-like structures called flagella on the surface (see Figure 3.1). A small cell motor rotates this bundle of flagella to generate a flow field [82]. Another natural microswimmer, *Chlamydomonas reinhardtii*, has two flagella (shown in Figure 3.1), both beat in a breaststroke-like pattern to move the swimmer forward [83].

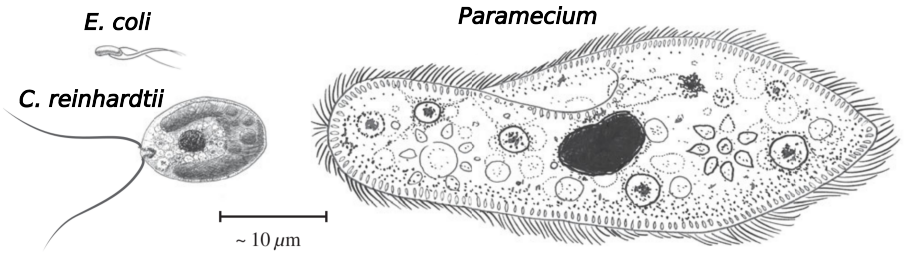

Figure 3.1: **Natural microswimmers with hair-like appendages:** This schematic figure illustrates the variety in the number and type of hair-like appendages across different natural microswimmers. For example, *Escherichia coli* has multiple flagella, *Chlamydomonas reinhardtii* has only two flagella, and *Paramecium* has multiple cilia (shorter flagella) that cover its entire body. The figure is sourced from [84].

To model the dynamics of the swimmers, we use the Squirmer model, developed by Lighthill and Blake [85, 86]. The model approximates the swimmer as a spherical object, whose surface undergoes periodic waving motion (like microswimmer surface with cilia) to generate a flow field. In its simplest form, the model approximates this squirming motion

by incorporating tangential slip velocity on the spherical surface (see Figure 3.3). This surface slip velocity creates a flow field around the swimmer and propels it forward.

As discussed in Chapter 1, microswimmers swim in low Reynolds number regime [16], where the viscous forces dominate over the inertial forces. Therefore, the flow field $\mathbf{u}$ around the microswimmers is a Stokes flow. The Stokes and continuity equations can be written as:

$$\begin{aligned} \nabla \cdot \mathbf{u} &= 0 \\ \nabla p &= \eta \nabla^2 \mathbf{u} \end{aligned} \tag{3.1}$$

where η is the fluid viscosity and p is the pressure. The solution of above equations can be expanded into a series of flow fields generated by singular sources [84], such as the source dipole and the force dipole (shown in Figure 3.2). The flow field due to the source dipole decays as $1/r^3$, where r is the distance from the swimmer. The flow field due to the force dipole decays as $1/r^2$ (extensile force dipole is shown in Figure 3.2). Studies have shown that combination of a source dipole and force dipole is sufficient to describe far-field flows generated by microswimmers [84, 87, 17, 13, 88].

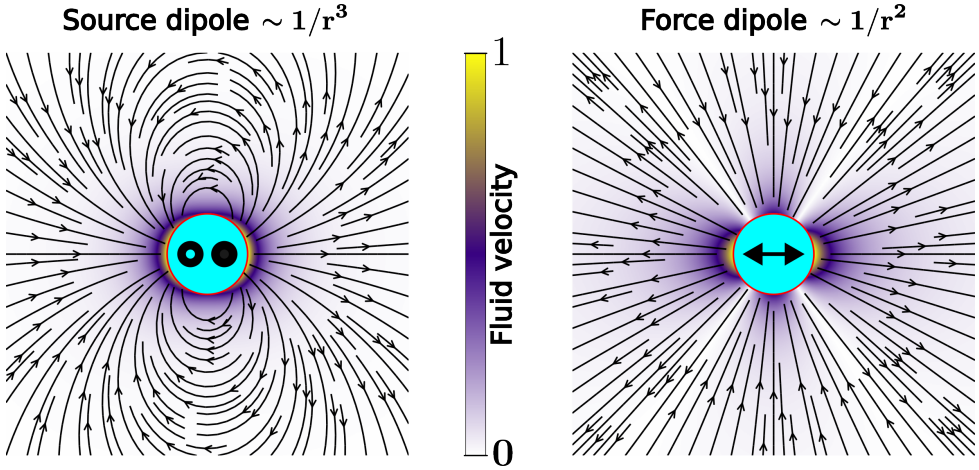

Figure 3.2: **Flow field due to singular sources:** The figure illustrates the flow fields generated by a source dipole and a force dipole (extensile). The color bar represents the scaled velocity. Streamlines indicate the direction of fluid movement. If the distance from the singular source is given by r, then the flow field of a source dipole decays as $1/r^3$, while that of a force dipole decays as $1/r^2$. Source dipole consist of a source (where the fluid direction is radially outward) and a sink (where the fluid direction is radially inward). An extensile force dipole pushes the fluid outwards along the axis (black double-sided arrow). At large distances from a microswimmer, the flow has no contribution from the source dipole, the dominant flow is a force dipole [84].

3.2 | Squirmer model

As per the standard Squirmer model, the axisymmetric slip velocity u_s, at the surface of a spherical swimmer of radius R is given by [84]

$$u_s(\theta)|_{r=R} = B_1 \sin\theta + B_2 \sin\theta\cos\theta \tag{3.2}$$

where θ is the polar angle measured from the swimmer orientation vector $\hat{\mathbf{e}}$ (refer to Figure 3.3). The coefficient B_1 is related to the source dipole, and it sets the swimming speed $u_0 = \frac{2B_1}{3}$. The coefficient B_2 corresponds to the strength of the force dipole and influences the fluid mixing around the swimmer. When $B_2 < 0$, the force dipole is extensile; the fluid is pushed outwards along the swimmer axis (see flow field of the force dipole in Figure 3.2). Conversely, when $B_2 > 0$, the force dipole is contractile; the fluid is pulled inwards along the swimmer axis.

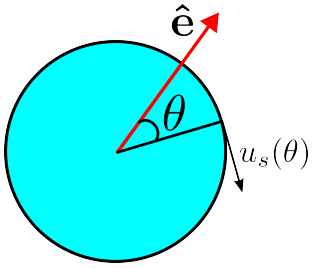

Figure 3.3: **Definition of θ in the Squirmer model:** The figure depicts a spherical squirmer with an orientation vector $\hat{\mathbf{e}}$. The slip velocity u_s at the squirmer surface is given by $u_s(\theta) = B_1 \sin\theta + B_2 \sin\theta\cos\theta$, where θ is the angle between a point on surface and $\hat{\mathbf{e}}$.

As discussed earlier, microswimmers use various propulsion mechanisms to generate flow fields. For example, the *E. coli* bacterium generates thrust from behind. It rotates its flagella bundle located at the back to push the bacterial body forward. Therefore, *E.coli* is classified as a pusher [17]. Another example of a pusher is *B.subtilis* [26]. A pusher is characterized by a far-field flow resembling that of an extensile force dipole. Conversely, some microswimmers, such as *C. reinhardtii*, generate thrust from the front. They propel themselves forward by pulling and are therefore classified as pullers. A puller exhibit a far-field flow resembling to a contractile force dipole [89].

In the squirmer model, pushers and pullers are distinguished by the squirmer parameter $\beta = \frac{B_2}{B_1}$. A squirmer with $\beta < 0$ exhibits an extensile flow field (fluid is pushed outwards along the axis), and is therefore called a pusher squirmer (example shown for $\beta = -5$, in Figure 3.4). In contrast, a squirmer with $\beta > 0$ exhibits a contractile flow field (fluid is pulled inwards along the axis), and is classified as a puller squirmer (see $\beta = +5$ in Figure 3.4). A third category includes microswimmers like *Volvox* and *Paramecium*, which lack force dipole contributions in their far-field flow [89, 90]. Such microswimmers are represented by neutral squirmers, with $\beta = 0$ (see Figure 3.4).

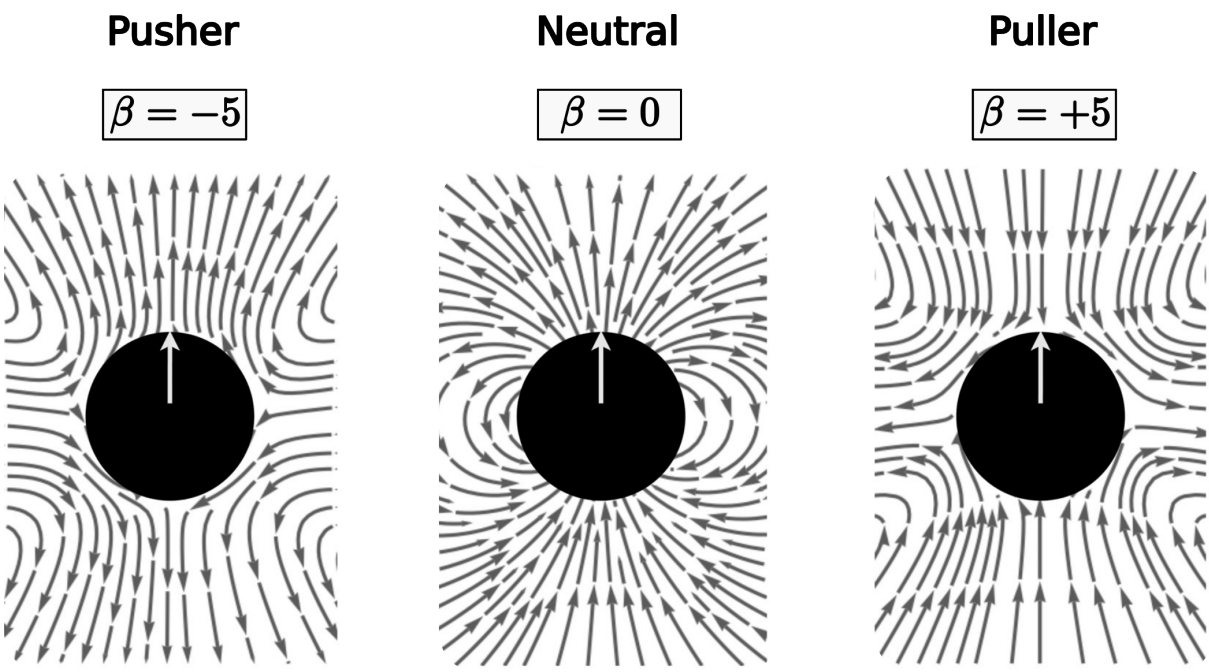

Figure 3.4: **Squirmer flow fields:** Flow fields generated by various types of squirmers, pusher ($\beta = -5$), puller ($\beta = +5$), and neutral ($\beta = 0$). The swimming direction is indicated by the white arrow. Streamlines (in black) show the (local) movement of fluid. A pusher flow field resembles an extensile force dipole; the fluid is pushed outwards along the moving direction. A puller flow field resembles a contractile force dipole; the fluid is pulled inwards along the moving direction. Neutral squirmer's flow field only has source dipole. The figure is taken from [91].

Chapter 4

Simulation model

This chapter focuses on the model used to simulate the nematic liquid crystal. First, the Landau free energy is reviewed, which describes the energy landscape of the liquid crystal. Following that, the Beris-Edwards equation is discussed, which governs the dynamic evolution of the order parameter tensor (**Q**-tensor). Finally, a short introduction to the Lattice Boltzmann method (LBM) is provided, a tool to solve the hydrodynamic equations (like Navier-Stokes), which govern the flow within the system.

4.1 | Hydrodynamics of Liquid Crystal

The Landau-de Gennes free energy density describes the thermodynamics of a liquid crystal. In the uniaxial nematic phase with a spatially invariant **Q** (no deformations in the nematic director field), the free energy density simplifies to the bulk term [60]:

$$F_{\text{bulk}} = \frac{A_0}{2}\left(1 - \frac{\gamma}{3}\right) Q_{\alpha\beta}^2 - \frac{A_0\gamma}{3} Q_{\alpha\beta}Q_{\beta\gamma}Q_{\gamma\alpha} + \frac{A_0\gamma}{4}(Q_{\alpha\beta}^2)^2 \tag{4.1}$$

When the director field is not uniform and there are deformations (as shown in Figure 2.10), an additional elastic term is added [60],

$$F_{\text{elastic}} = \frac{K}{2}(\partial_\gamma Q_{\alpha\beta})^2 \tag{4.2}$$

If the liquid crystal is confined between two surfaces with anchoring effects, an anchoring term is added,

$$F_{\text{anch}} = \frac{1}{2} W_0 (Q_{\alpha\beta} - Q_{\alpha\beta}^0)^2 \tag{4.3}$$

Consequently, the total Landau free energy density, $\mathcal{F}$, of a nematic liquid crystal is the sum of various contributions,

$$\mathcal{F} = F_{\text{bulk}} + F_{\text{elastic}} + F_{anch} \tag{4.4}$$

4.1.1 | Beris-Edwards equation

The dynamics of the order parameter **Q**-tensor is governed by the Beris-Edwards equation [92],

$$(\partial_t + \vec{\mathbf{u}} \cdot \nabla)\,\mathbf{Q} = \Gamma \mathbf{H} + \mathbf{S}(\mathbf{W}, \mathbf{Q}) \tag{4.5}$$

In this equation, the right-hand side accounts for the advection of **Q** by the fluid with velocity $\vec{\mathbf{u}}$. On the left-hand side, the first term $\Gamma\mathbf{H}$, is responsible for relaxation towards the minimum of the total free energy density $\mathcal{F}$ (given by Equation 4.4). Here, Γ denotes the rotational diffusion constant, which sets the timescale for this relaxation motion. The molecular field, **H**, represents the variation of $\mathcal{F}$ with respect to **Q**,

$$\mathbf{H} = \frac{\delta \mathcal{F}}{\delta \mathbf{Q}} + \left(\frac{\mathbf{I}}{3}\right) \mathrm{Tr}\, \frac{\delta \mathcal{F}}{\delta \mathbf{Q}} \tag{4.6}$$

The molecular field **H** provides the force that drives the liquid crystal towards the equilibrium state. The second term in Equation 4.5, $\mathbf{S}(\mathbf{W}, \mathbf{Q})$, is the flow coupling term. It describes how the orientation of liquid crystal molecules is influenced by fluid flow,

$$\mathbf{S}(\mathbf{W}, \mathbf{Q}) = (\xi \mathbf{D} + \boldsymbol{\omega}) \left(\mathbf{Q} + \frac{\mathbf{I}}{3}\right) + (\xi \mathbf{D} - \boldsymbol{\omega}) \left(\mathbf{Q} + \frac{\mathbf{I}}{3}\right) - 2\xi \left(\mathbf{Q} + \frac{\mathbf{I}}{3}\right) \mathrm{Tr}(\mathbf{Q}\mathbf{W}) \tag{4.7}$$

Here, **W** is the velocity gradient tensor. **D** and $\boldsymbol{\omega}$ represent the symmetric and antisymmetric contributions to **W**. The parameter ξ depends on the molecular details of the liquid crystal and determines whether the director field is flow aligning or flow tumbling. Specifically, if $\xi > 1$, the director field is flow tumbling, and if $\xi < 1$, the field is flow aligning.

The dynamics of a liquid crystal, governed by the Beris-Edwards equation, is intricately coupled with the Navier-Stokes (NS) equations:

$$\rho\left(\partial_t u_\alpha + u_\beta \partial_\beta u_\alpha\right) = \partial_\beta \Pi_{\alpha\beta} + \eta \partial_\beta \left(\partial_\alpha u_\beta + \partial_\beta u_\alpha\right) \tag{4.8}$$

Here ρ represents the fluid density and η denotes the isotropic viscosity. The flow field, $\vec{\mathbf{u}}$, also obeys the continuity equation $\partial_t \rho = -\nabla \cdot (\rho \vec{\mathbf{u}})$. For an incompressible fluid, this equation simplifies to $\partial_\alpha(\rho u_\alpha) = 0$. In Equation 4.8, $\mathbf{\Pi}$ denotes the thermodynamic stress tensor. For a liquid crystal without any activity, the stress tensor is expressed as,

$$\begin{aligned} \Pi_{\alpha\beta} = {} & 2\xi \left(Q_{\alpha\beta} + \frac{1}{3}\delta_{\alpha\beta}\right) Q_{\gamma\epsilon} H_{\gamma\epsilon} - \xi H_{\alpha\gamma} \left(Q_{\gamma\beta} + \frac{1}{3}\delta_{\gamma\beta}\right) \\ & - \xi \left(Q_{\alpha\gamma} + \frac{1}{3}\delta_{\alpha\gamma}\right) H_{\gamma\beta} - \partial_\alpha Q_{\gamma\nu} \frac{\delta \mathcal{F}}{\delta \partial_\beta Q_{\gamma\nu}} + Q_{\alpha\gamma} H_{\gamma\beta} - H_{\alpha\gamma} Q_{\gamma\beta} \end{aligned} \tag{4.9}$$

Note, in the case of active nematic systems, the stress tensor has an additional term $-\zeta\mathbf{Q}$, reflecting the active nature of the liquid crystal molecules [49, 48]. The parameter

ζ, known as activity, depends on the flow field generated by active liquid crystal molecules. If their flow field is of an extensile type, pushing fluid away along the molecular long axis, then $\zeta > 0$. Conversely, if their flow field is of a contractile type, pulling fluid inwards along the molecular long axis, then $\zeta < 0$. In our simulations, $\zeta = 0$, the liquid crystal is not active, only particles (swimmers) are active.

4.2 | Lattice Boltzmann Method

The fundamental concept behind LBM is to represent the fluid as a collection of fictitious particles on a lattice, where each lattice node is associated with a set of distribution functions $\{f_i\}$. These f_i's represent the probability density of finding a (fluid) particle with a discrete velocity $\vec{\mathbf{c}}_i$. The evolution of f_i in time Δt is given by the equation [93],

$$f_i(\vec{\mathbf{r}} + \vec{\mathbf{c}}_i\Delta t, t + \Delta t) - f_i(\vec{\mathbf{r}}, t) = -\frac{\Delta t}{\tau}\left(f_i(\vec{\mathbf{r}}, t) - f_i^{eq}(\vec{\mathbf{r}}, t)\right) \tag{4.10}$$

The left-hand side represents the streaming of (fluid) particles to neighboring nodes, and the right-hand side accounts for the the relaxation toward the equilibrium distribution, given by f_i^{eq}. The relaxation time scale τ, sets the kinematic viscosity ν of the fluid:

$$\nu = c_s^2(\tau - \frac{\Delta t}{2}) \tag{4.11}$$

Here, c_s is the speed of sound in lattice units. The discrete velocities $\{\vec{\mathbf{c_i}}\}$ in Equation 4.10, are chosen from a set based on the lattice configuration. To obtain hydrodynamic quantities like fluid's density (ρ) and velocity ($\vec{\mathbf{u}}$) at a lattice node,

$$\rho = \sum_i f_i \qquad\qquad \rho\vec{\mathbf{u}} = \sum_i f_i\vec{\mathbf{c_i}} \tag{4.12}$$

Typically, Lattice Boltzmann Method (LBM) lattices are denoted as "DnQm", where "n" indicates the spatial dimension, and "m" corresponds to the number of discrete velocities in the set $\{\vec{\mathbf{c_i}}\}$. For 2D studies, the commonly adopted lattice is D2Q9, characterized by a 9-velocity model. In 3D simulations, various velocity models are available, with the favored choice being the 19-velocity model. Consequently, the preferred lattice used in 3D simulations is D3Q19. In this thesis, whether the simulation is quasi-2D or full 3D, only D3Q19 lattice is used.

4.3 | Implementation

The liquid crystal dynamics follows the Beris-Edwards equation (Equation 4.5) and the fluid flow is governed by the Navier-Stokes (Equation 4.8) and continuity equations. These equations are connected via an elastic tensor (Equation 4.9). Our simulations are conducted using the *Ludwig* simulation package [59], which efficiently solves these equations using a hybrid approach. Specifically, the Beris-Edwards equation is tackled through the finite-difference method, and the Navier-Stokes equation is solved using LBM. In our simulations, the microswimmers are modelled as spherical swimmers, rendered motile by a surface slip velocity (Equation 3.2 in Chapter 3). In LBM, a solid boundary is typically modelled using the bounce back scheme [94, 95]. However, this can be modified to take into account for particle motion [96] and the effects of the active slip flow, as done in [97]. This is also implemented within the *ludwig* code; for full details, please refer to this link: `https://ludwig.epcc.ed.ac.uk/`

Chapter 5

Microswimmers in tighlty confined nematics

This chapter presents our simulation results for a system of spherical microswimmers in a nematic liquid crystal, confined within quasi-2D space. We begin by outlining the simulation setup and initial conditions. Next, we analyze the emerging instability for systems with pusher populations, and present a state diagram. We also examine the role of motility in the emerging instability by considering pushers with zero speed.

5.1 | Simulation setup

To conduct our simulations, we used a simulation box with dimensions $256 \times 256 \times 27$, along the x, y, and z directions. The system was confined in quasi-2D space, by placing walls in the z-direction (see Figure 5.1). The walls had planar surface anchoring, which allowed free movement of the nematic director only in the xy-plane; any deviations from this plane were penalized. Spherical swimmers with random orientations were placed at the mid-plane. The nematic liquid crystal was uniformly initialized throughout the box with a scalar order parameter $s = 1/3$, and the director field $\hat{\mathbf{n}}(\mathbf{r})$ was initialized along the x-axis (represented as pink in Figure 5.1). Periodic boundary conditions were imposed at the box edges along the x and y direction.

N spherical swimmers/squirmers of radius $R = 6$ in the lattice units (LU) were used in simulations. For self-propulsion, a surface slip velocity (given by Equation 3.2) was applied at swimmers surfaces. We considered pusher-type swimmers (pushes the fluid outward along the particle axis). The source dipole strength B_1 in the squirmer parameter β was fixed at 0.0015, which set the swimming speed $u_0 \equiv \frac{2}{3}B_1 = 10^{-3}$ LU. The force dipole strength B_2 was systematically varied, such that $\beta \in [-5, -1]$. The number of swimmers is represented using the area (volume) fraction ϕ_{af}, defined as $\phi_{af} = \frac{N\pi R^2}{L_x L_y}$. The ϕ_{vf} was varied between 5% and 20%.

For modeling the nematic liquid crystal, following parameters were used: $A_0 = 0.1$, $\gamma = 3.0$, $K = 0.005$, $\Gamma = 0.3$, and rotational viscosity $\gamma_1 = \frac{2s^2}{\Gamma} = 5/3$. These parameters set the Reynolds number, $\mathrm{Re} \equiv \frac{u_0 R}{\eta} \approx 0.036$, and the Ericksen number, $\mathrm{Er} \equiv \frac{\gamma_1 u_0 R}{K} \approx 2$.

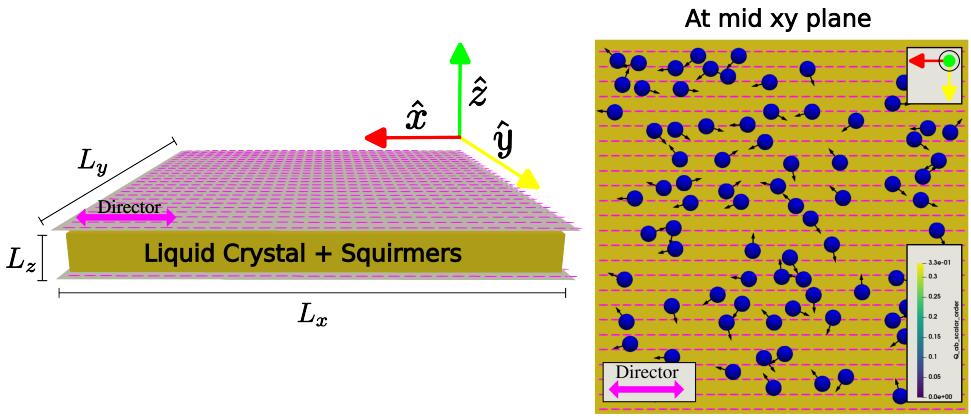

Figure 5.1: **Illustration of the quasi-2D simulation setup:** The figure shows our quasi-2D simulation setup. The system consisting of spherical swimmers within a nematic liquid crystal, is confined between walls. Planar anchoring is imposed on the walls and the director field (in pink) is initialized along the x-direction. In right figure; particles (blue spheres) are initialized at the mid-plane with random x,y coordinates and random orientations (in black). The color bar represents the value of scalar order parameter s, which is uniform and initialized to $s = 1/3$ throughout the simulation box.

In [49, 98, 99], the activity at the continuum limit is defined as being directly proportional to both the force dipole strength and the concentration of active particles. We adopted the same approach in our simulations, the global activity was increased by either increasing the force dipole strength, characterized by $|\beta|$, or the volume fraction ϕ_{af}, or both.

5.2 | Pushers in quasi-2D nematic liquid crystal

5.2.1 | Uniform, Wave and Chaotic states

When pusher swimmers were introduced in the nematic liquid crystal, at low global activity, the uniform nematic order was observed to be stable. The director field, initially aligned along the x-axis, remained uniform and aligned in the same direction (refer to Figure 5.2). Some perturbations were observed in the director field, but they were localized (refer to $|\beta| = 3$ in Figure 5.2), the overall nematic order remained uniform. Throughout the thesis, liquid crystal state with stable uniform nematic order is referred as the "Uniform state".

Beyond a critical global activity, the coupling between the swimmer flow fields and the nematic order led to a flow instability; the uniform nematic alignment became unstable, and periodic distortions were observed in the director field (shown in Figure 5.3). Due to the distinctive wave-like pattern, this state was named, the "Wave state". At even higher activities, the wave pattern disappeared, and we observed defects in the system. Straight disclination lines appeared, which looked like point defects in 2D (see red triangles and circular arcs in Figure 5.4). This state was labeled as the "Chaotic state". Within the

chaotic states, the number of defects (on average) was oberved to increase with global activity (refer to Figure 5.4).

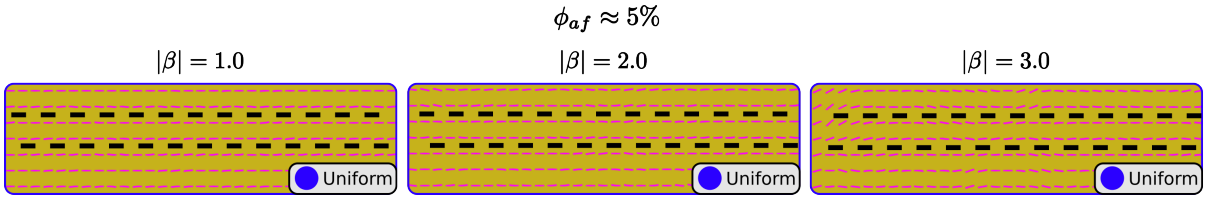

Figure 5.2: **Examples of uniform states**: For the nematic liquid crystal with pusher population (ϕ_{af}), the figure shows the director fields (in pink) for various force dipole strength (β). For better visualization, pushers are not shown here. Within the uniform states, the perturbations in the director field are localized (see rightmost figure), and has no effect on the global uniform nematic alignment. The director fields are shown at the steady state and at the section of xy-midplane. The yellow color represents the scalar order parameter $s = 1/3$. Black dashed lines indicate the global alignment of the director field.

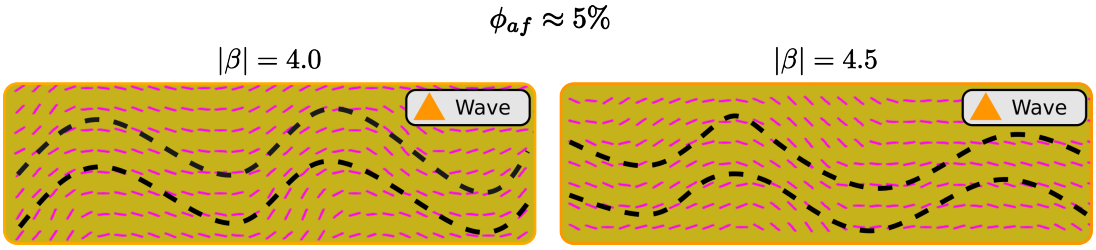

Figure 5.3: **Emergence of periodic distortions in the director field**: The figure shows the wave-like pattern observed in the wave states. The director fields (in pink) are shown at the steady state and at the xy-midplane. Increasing swimmer concentration ϕ_{af} or the force dipole strength $|\beta|$, beyond a critical threshold leads to periodic distortions in the director field. The black dashed lines highlight the periodic wave-like pattern.

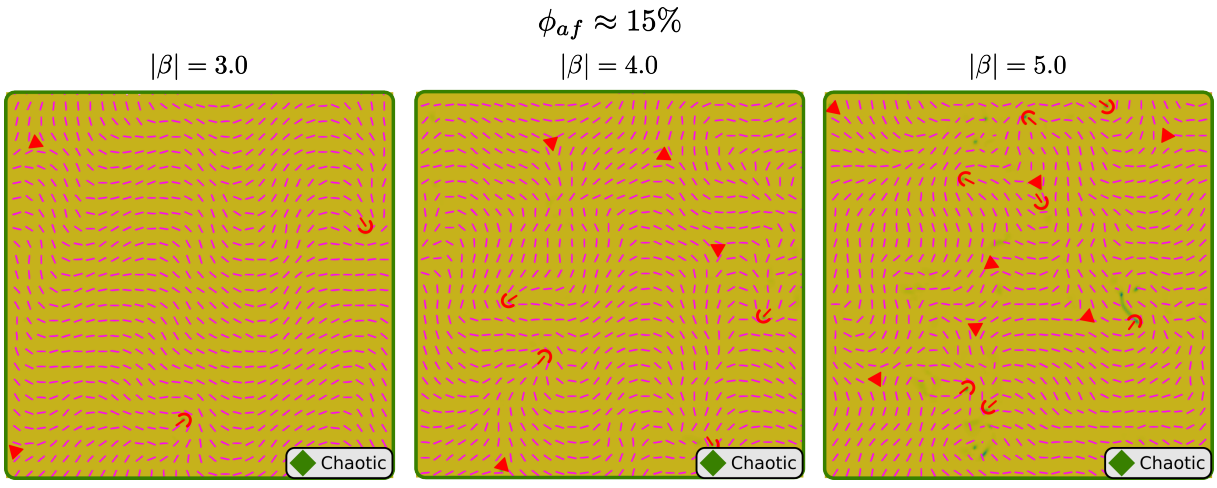

Figure 5.4: **Increase in the number of defects with activity**: At higher global activity, straight disclination lines (look like point defects in 2D) are observed in the system. The director field (in pink) is observed to have no spatial symmetry. Within the chaotic state, the number of defects (on average) is observed to increase with activity (left to right). In defect-free regions (yellow region), scalar order parameter $s \approx 1/3$, which decreases by 20% close to a defect (greenish region). Red triangles approximate the positions of $-1/2$ defects, and circular arcs indicate $+1/2$ defects. Not all defects are marked.

In steady uniform states at low volume fraction ϕ_{af}, pushers were observed to swim along the local nematic director $\hat{\mathbf{n}}$ in an apolar fashion (i.e., swimming along $\hat{\mathbf{n}}$ and $-\hat{\mathbf{n}}$). This behavior aligns with an individual spherical pusher swimming in a nematic liquid crystal [39]. However, at higher ϕ_{af}, the apolar motion was not observed within the mid-plane of the simulation box. Because of higher collision frequency, pushers were observed to swim near the walls.

Our simulations reveal that the collective effects of swimmers can destabilize the uniform nematic order. Above a critical activity, the coupling between the swimmer flow fields and the nematic order triggered a flow instability, which caused periodic distortions in the director field $\hat{\mathbf{n}}$. In the next section, we analyze the director field deformations (twist, bend, and splay) across the uniform, wave, and chaotic states to characterize the underlying nature of instability.

5.2.2 | Analysis of director field distortions

Following the procedure explained in Section 2.5.2, we calculated the deformations in the director field (at steady state) for different values of force dipole strength $|\beta|$, at each volume fraction ϕ_{af} (shown in Figure 5.5). At low global activity, distortions were observed to be minimal (Uniform regions in Figure 5.5). This is because, while pusher flow fields perturbed the nematic director field, these perturbations remained localized around the swimmer at low activity (refer to $|\beta|= 3$ in Figure 5.2). Above a critical activity, the influence of flow fields on the global nematic alignment became significant, and we observed a wave-like pattern in the director field, as showed in Figure 5.3. In these wave states, bend dominated the distortions, followed by the splay and twist (see Wave regions in Figure 5.5). At higher activities, the distortions further increased, and defects appeared in the chaotic states (Chaotic regions in Figure 5.5).

The distortion analysis indicates the growth of all distortions with activity, but particularly, we see a significant increase in bend distortions. This suggests that bend is the dominant instability. In our system, the activity is from pusher swimmers, which have extensile flow fields (fluid is pushed along the particle axis). A pusher swims parallel to the nematic director [39]. Therefore, our system can be seen as a nematic liquid crystal with moving extensile force dipoles. Interestingly, the linear stability analysis of 2D extensile active nematics has predicted bend to be the most unstable mode. Therefore, our results agree with the theoretical predictions (as shown by increasing bend in Figure 5.5). Continuum simulation studies [53, 98, 50, 100] of extensile active systems in 2D, have also observed the dominance of bend.

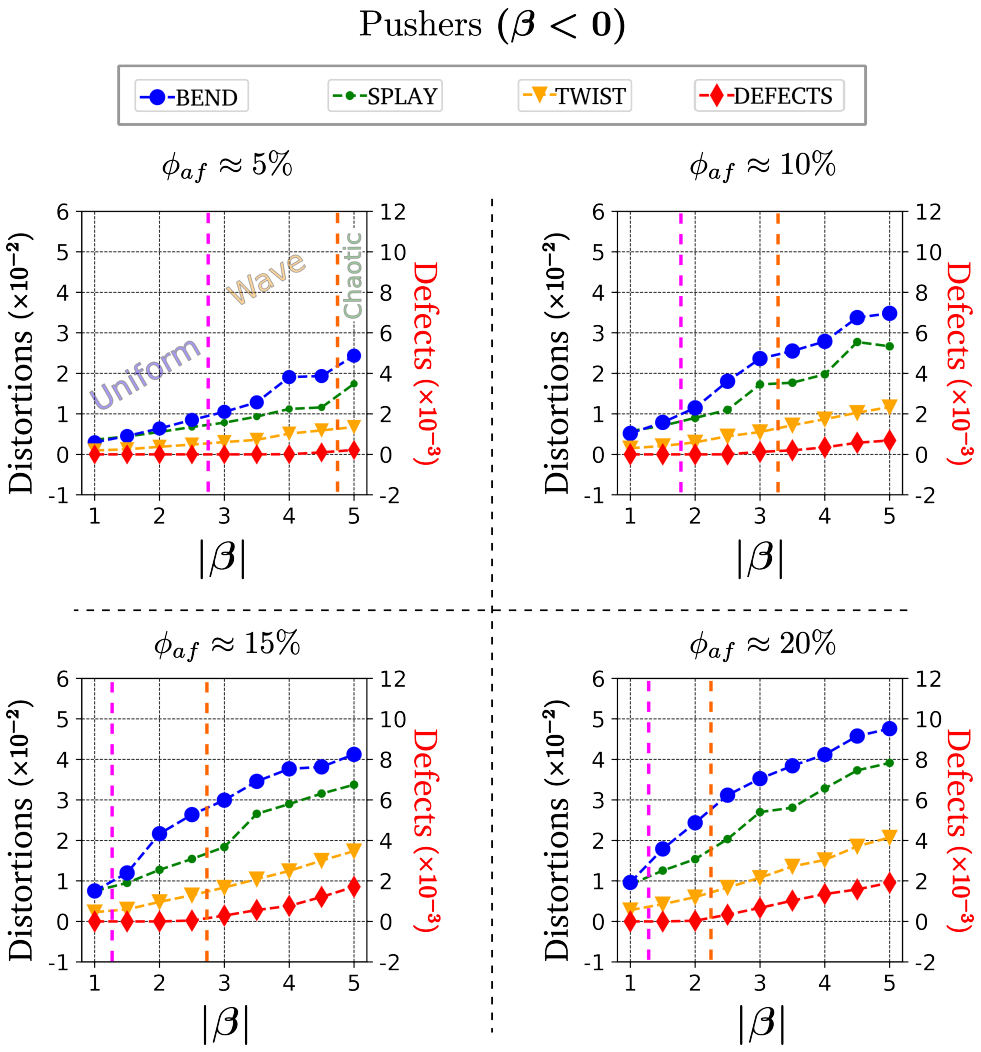

Figure 5.5: **Distortions and defect densities** For nematic liquid crystals with pushers, confined within quasi-2D space, the figure shows the distortion and defect densities as a function of the squirmer parameter $|\beta|$, for various volume fraction ϕ_{af}. The values are time averaged over steady states. The pink dashed line separates the Uniform and Wave states, and the orange dashed line separates the Wave and Chaotic states. Distortions: twist (yellow), bend (blue), and splay (green) are minimal in the uniform states. Within wave states, high values of bend is observed. In chaotic states, distortions have higher values and non-zero defect densities.

5.3 | State Diagram (quasi-2D)

Our simulations show that the uniform nematic alignment is unstable to activity. Because of swimmer flow fields, the liquid crystal state transitions from Uniform, to Wave and to Chaotic state. Figure 5.6 shows the state diagram summarizing the nature of the steady state observed at various volume fraction ϕ_{af} and squirming strength $|\beta|$.To classify states, we visually inspected the director field (within the mid-plane) at steady state. States with periodic wave-like pattern (like in Figure 5.3) were identified as Wave state, while states with defects (as in Figure 5.4) present were classified as Chaotic.

In our system, the state transition is observed to depend on both swimmer volume fraction ϕ_{af} and force dipole strength $|\beta|$ (see state diagram in Figure 5.6). At the continuum limit, the activity scales with both the force dipole strength and the concentration of active particles [49, 98, 99]. Following the same, we approximate the global activity ζ for our system, as $\zeta \sim |B_2|\,\phi_{af}$, where B_2 represents the force dipole strength. With all other parameters fixed, the transition occurs at a critical activity ζ^*, which gives a critical volume fraction $\phi^*_{af} \sim B_2^{-1}$. This relationship captures the transition boundary between the uniform and the wave states remarkably well (pink line in Figure 5.6).

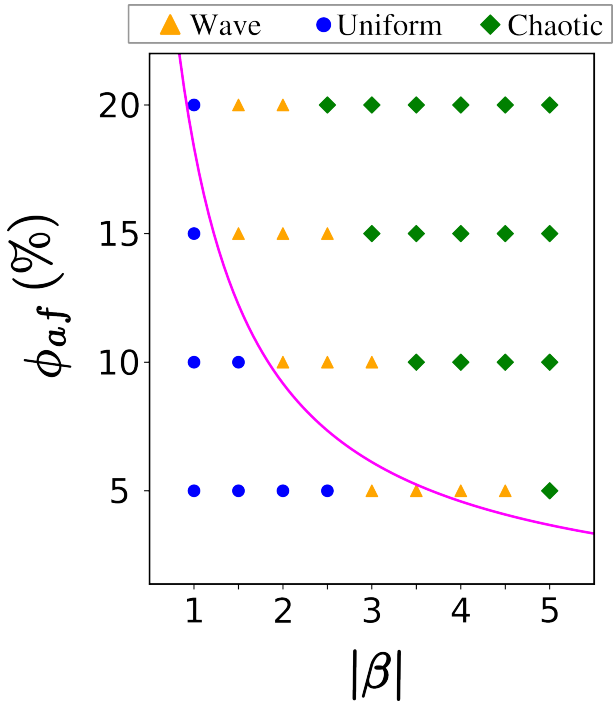

Figure 5.6: **State diagram**: For a system consisting of spherical microswimmers in a confined (quasi-2D) nematic liquid crystal, the figure shows the observed steady states, as a function of the squirmer parameter $|\beta|$ and the swimmer volume fraction ϕ_{vf}. In $\beta = \frac{B_2}{B_1}$, the source dipole is kept constant $B_1 = 0.0015$, only the force dipole strength is varied B_2. Blue circles represent stable uniform states, orange triangles denote stable wave states, and green rhombuses indicate chaotic states. Pink line represents the best fit for the critical volume fraction $\phi^*_{af} \sim B_2^{-1}$.

5.4 | Pusher-Shakers in 2D nematic liquid crystal

In the nematic liquid crystal with pusher swimmers, a flow instability emerged due to the coupling between swimmer flow fields and the orientational order. Now, we investigate the effect of swimming speed on this instability by introducing pushers with zero speed, also called pusher-shakers. These particles generate pusher-like hydrodynamic flow but has no self-propulsion. The source dipole term B_1 in the slip velocity (Equation 3.2), determines the swimming speed u_0 $(= \frac{2B_1}{3})$. For shakers B_1 is set to be zero, which gives $u_0 = 0$. The sign of the force dipole strength B_2 determines the shaker type: $B_2 < 0$ corresponds to

pusher-shaker, which has pusher-like (extensile) flow field. Conversely, $B_2 > 0$ corresponds to puller-shaker (not addressed in this chapter).

The swimmer volume fraction was kept constant, $\phi_{af} \approx 15\%$, while the force dipole strength B_2 was varied in [-0.0075,-0.0015], to change the activity. Figure 5.7 summarizes our simulation results for pusher-shakers. We observed a similar transition as with pushers (from Uniform to Wave to Chaotic, see Figures 5.2 to 5.4). At low activity, the uniform nematic alignment was observed to be stable (Uniform state in Figure 5.7). Beyond a critical $|B_2|$, wave-like pattern was observed in the director field (Wave state in Figure 5.7), and at high activity, $\pm 1/2$ defects were observed in the system (Chaotic states in Figure 5.7).

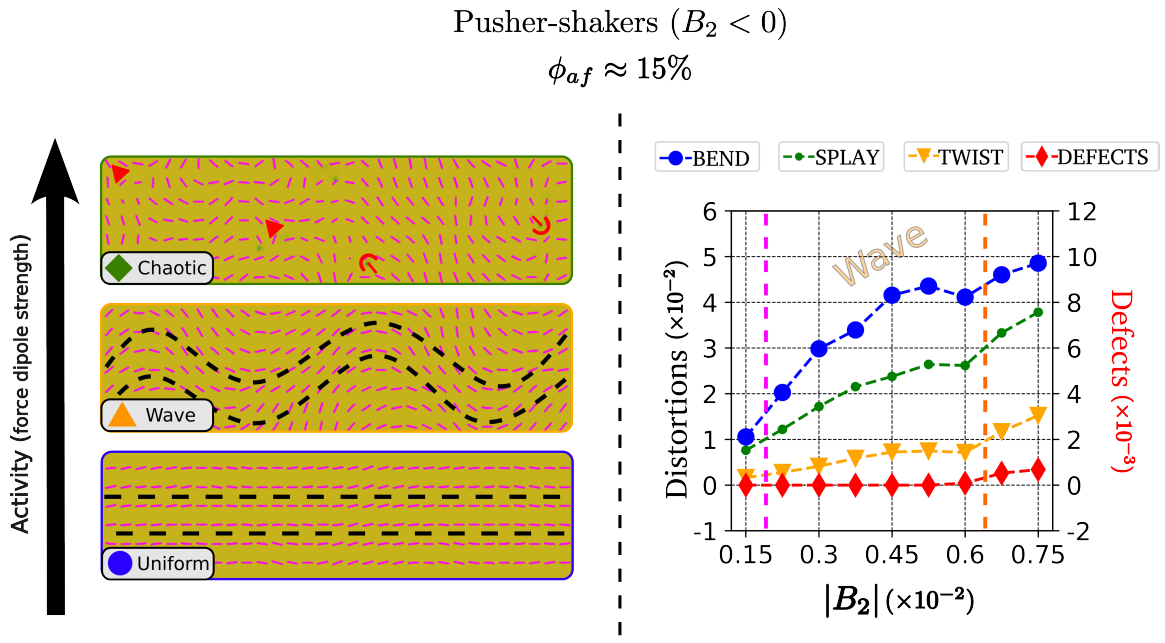

Figure 5.7: **Emergence of instability in nematic liquid crystals with pusher-shakers:** The figure provides a visual summary of our simulations with pusher-shakers. The uniform nematic order is observed to be unstable to activity. The particle volume fraction is fixed, $\phi_{af} \approx 15\%$. The activity is increased by increasing the force dipole strength $|B_2|$. In the left figure, the director fields (in pink) are presented for the Uniform state (at $|B_2| = 0.0015$), the Wave state ($|B_2| = 0.0030$), and the Chaotic state (at $|B_2| = 0.0075$). The right figure presents the distortion analysis, where the pink dashed line separates the Uniform and Wave states, and the orange dashed line separates the Wave and Chaotic states. Instability leads to higher values of bend deformations (Wave and chaotic region). Non-zero defect density is observed only in chaotic states.

Our findings align closely with observations for pushers (see Figures 5.2 to 5.4). Pusher-shakers also exhibit periodic undulations in the director field due to the flow instability (Wave state in Figure 5.7). The instability must be a result of the coupling between pusher-shakers flow fields and the liquid crystal order. Pusher-shakers are immobile and have no source dipole contribution in their flow fields. This suggests that instability is driven by the coupling between force dipoles and the nematic order. Since both pushers and pusher-shakers generate extensile flow fields, same flow instability can be expected for both. Indeed, the distortion analysis confirms this, bend dominated the deformations, followed by splay and twist (Figure 5.7).

5.5 | Discussion

In this chapter, we investigated the collective behavior of spherical microswimmers in a confined (quasi-2D) nematic liquid crystal. Our results suggest that, increasing the swimmer volume fraction (or force dipole strength) beyond a critical threshold onsets a flow instability, causing periodic undulations in the director field. By analyzing the distortions, we found bend as the most unstable mode, which aligns with predictions for 2D extensile active nematics [49].

Unlike in active nematics, our system has actual swimmers that generate flow fields and interact with the nematic liquid crystal. This makes our system fundamentally similar to real-world systems like bacterial suspensions in nematic environments, such as Living Liquid Crystals (LLCs) [40]. In our simulations, the director field patterns observed in the Uniform, Wave, and Chaotic states closely resemble to the ones seen in thin film LLC experiments (Figure 5.8). This agreement further validates our simulation model.

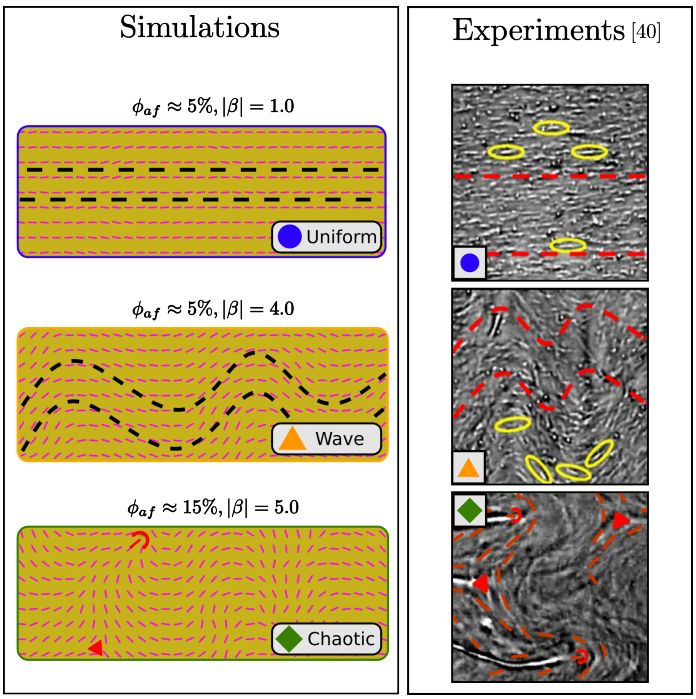

Figure 5.8: **Comparing our simulation results with LLC experiments:** Our system, consisting of spherical pusher swimmers in the nematic liquid crystal, is a realization of bacterial suspensions in nematic liquid crystals, such as living liquid crystals (LLCs) [40]. The figure compares our simulation results with the experiments observation with thin films LLCs [40]. At low swimmer density and activity, our simulations show a steady Uniform state with uniform nematic alignment, resembling LLCs with inactive bacteria (right-top). The Wave state (characterized by wave-like patterns in the director field) observed at higher activity resembles the periodic distortions seen in LLCs with active bacteria (right-middle). In regions with higher swimmer densities, LLC experiments observe the formation of $\pm 1/2$ defects (right-bottom), which is observed in our Chaotic states. The LLCs experiment images are adapted from [40].

The flow instability observed for pusher swimmers as well as for non-motile pusher-shakers suggest that the instability is independent of the swimming speed. The most unstable mode remained bend, for swimmers and for shakers. This consistency in dominant instability underscores the role of force dipoles, rather than source dipoles, in destabilizing the uniform nematic order.

While working in quasi-2D environment, we chose to exclude puller swimmers in our analysis, because an individual puller prefers to swim perpendicular to the director field [39]. Therefore, within our setup, it is highly probable that pullers would swim towards the walls of the simulation box.

The chapter explored the collective effects of the swimmer population in a quasi-2D nematic liquid crystal. We observed that the coupling between the swimmer flow field and the nematic order lead to a bend-dominated flow instability. Our findings agree with both theoretical predictions and experiments. To investigate whether the observed instability is influenced by the quasi-2D confinement, the next chapter extends our study into three-dimensional space, and we include pullers to comprehensively analyze the impact of swimmer flow fields on instability.

Chapter 6

Microswimmers in 3D nematic liquid crystal

In this chapter, we continue our study on the collective effects of microswimmers in nematic liquid crystals. Within quasi-2D confinement, we observed the emergence of a bend-dominated flow instability due to coupling between swimmer (pusher) flow fields and the nematic order. Now, we ask, what happens if we open the 3rd dimension? Will the bend remain the dominant instability for pusher swimmers in 3D ? Also, will the system with puller (contractile) swimmers exhibit a splay-dominated instability, which has been predicted for contractile active nematic systems?

We begin by introducing our 3D simulation setup, and describing the initial conditions for the system. Following that, we present simulation results, focusing on pusher swimmers followed by puller swimmers. In subsequent sections, we discuss the emerging instabilities, swimmer dynamics, and present a state diagram as a function of the swimmer volume fraction and the squirmer parameter. Additionally, we investigate the impact of swimming speed on the instability by introducing shakers (particles with zero swimming speed) in nematic liquid crystals.

6.1 | 3D Simulation Setup

Hydrodynamic simulations were conducted in a cubic simulation box with dimensions $128 \times 128 \times 128$ (Figure 6.1). Initially, spherical swimmers with random orientations were placed randomly inside the simulation box (refer to Figure 6.1). The nematic liquid crystal was uniformly initialized throughout the box with a scalar order, $s = 1/3$, and the director field $\hat{\mathbf{n}}(\mathbf{r})$ was aligned along the x-axis, as illustrated in Figure 6.2.

We initialized N spherical swimmers of radius $R = 6$ with the surface slip velocity given by Equation 3.2. Both pusher (extensile, $\beta < 0$) and puller (contractile, $\beta > 0$) swimmers were considered in our simulations. The source dipole coefficient B_1 in the squirmer parameter $\beta = \frac{B_2}{B_1}$ was kept at 0.0015, fixing the particle velocity $u_0 \equiv \frac{2}{3}B_1 = 10^{-3}$. The strength of the force dipole B_2 was then systematically varied in equal steps within the range $\beta \in [-5, +5]$. Negative values $B_2 < 0$ represent extensile flow fields (fluid

pushed outwards) for pushers, while positive values $B_2 > 0$ represent contractile flow fields (fluid pulled inward) for pullers. The swimmer volume fraction ϕ_{vf} was calculated using $\phi_{vf} = \frac{N\,4/3\pi R^3}{L^3}$, where L is the box size. The ϕ_{vf} was varied between 1% and 5% for both pushers and pullers.

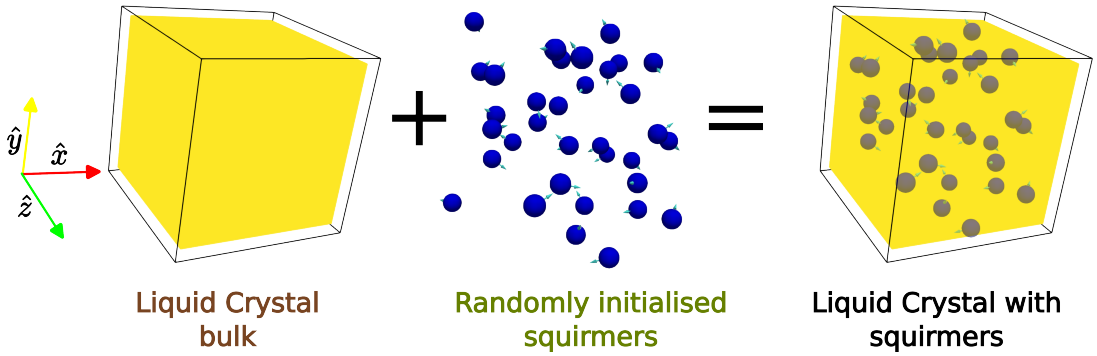

Figure 6.1: **Schematics of the 3D simulation setup:** The simulations were conducted in a 3D box of dimension $128 \times 128 \times 128$. The nematic liquid crystal was uniformly initialized throughout the simulation box, and the director field was initialized along the x-axis. The microswimmers with random orientations were randomly placed inside the box.

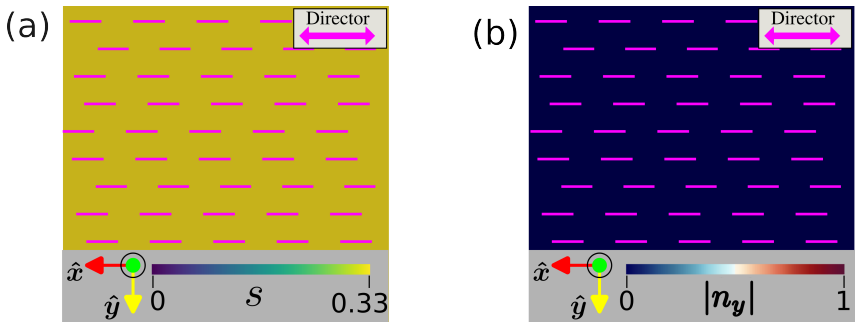

Figure 6.2: **Nematic liquid crystal at initial time step**: The figure shows the initial director field (in pink), at a random xy-plane. In subfigure (a), the color bar corresponds to the scalar order parameter $s = 1/3$. In subfigure (b), the color bar indicates the absolute value of the director component along y-axis, denoted by $|n_y|$.

To maintain consistency with our quasi-2D simulations, we used the same liquid crystal parameters: $A_0 = 0.1$, $\gamma = 3.0$, $K = 0.005$, $\Gamma = 0.3$, and rotational viscosity $\gamma_1 = \frac{2s^2}{\Gamma} = 5/3$. These parameters give the same Reynolds number, $\mathrm{Re} \equiv \frac{u_0 R}{\eta} \approx 0.036$, and the Ericksen number, $\mathrm{Er} \equiv \frac{\gamma_1 u_0 R}{K} \approx 2$.

6.2 | Pushers in 3D nematic liquid crystal

6.2.1 | Uniform state

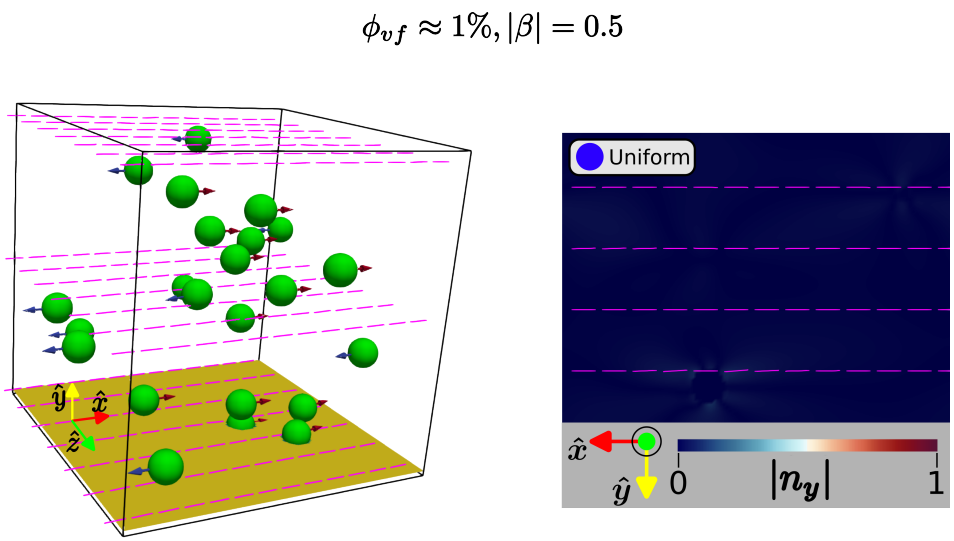

Figure 6.3: **Uniform state**: For the nematic liquid crystal with pusher swimmers, an example of a stable Uniform state observed at a volume fraction of $\phi_{vf} \approx 1\%$ and a squirming parameter of $|\beta| = 0.5$. On the left, a snapshot of the 3D simulation box at steady state with nematic directors (colored in pink) and pushers (in green). Pushers are observed to follow nematic director and exhibit apolar linear motion, red and blue arrows indicate motion along $(\hat{x})$ and $(-\hat{x})$, respectively. The yellow color represents the value of the scalar order parameter $s = 1/3$. In the right figure, the director field is shown at a random xy-plane within the simulation box, and the color bar corresponds to $|n_y|$, the absolute value of the director component along $\hat{y}$. The nematic director field is not affected by inclusion of pushers, the distortions are minimal and localized (represented by light white shading).

In 3D nematic liquid crystals with pusher swimmers, at low global activity, the uniform nematic state was observed to be stable. Figure 6.3 shows a system at low volume fraction and low force dipole strength, where the nematic director field, which was initially aligned along the x-axis, remains unaffected and aligned in the same direction. The pushers were found to swim along the nematic director $\hat{\mathbf{n}}$ in an apolar fashion, meaning the number of swimmers moving along $\hat{\mathbf{n}}$ and $-\hat{\mathbf{n}}$ was balanced (see red and blue arrows in Figure 6.3). At low global activity, the distortions in the director field were minimal and localized around the particle (see $\phi_{vf} \approx 4\%$ and $|\beta| = 0.5$ in Figure 6.4). As discussed in Chapter 5, such states with stable nematic order are classified as Uniform.

The director field distortions in the uniform states were observed to be minimal but not zero. This is because pushers generate flow fields and perturb the surrounding director field. In the uniform states, these perturbations remain localized around the particles and do not affect the global uniform nematic order. However, within the uniform states, increasing global activity, either by increasing swimmer volume fraction or the magnitude

of force dipole, resulted in more local perturbations. This is demonstrated by increasing (light) white regions in Figure 6.4 from left to right, which signify the growing extent of local perturbations.

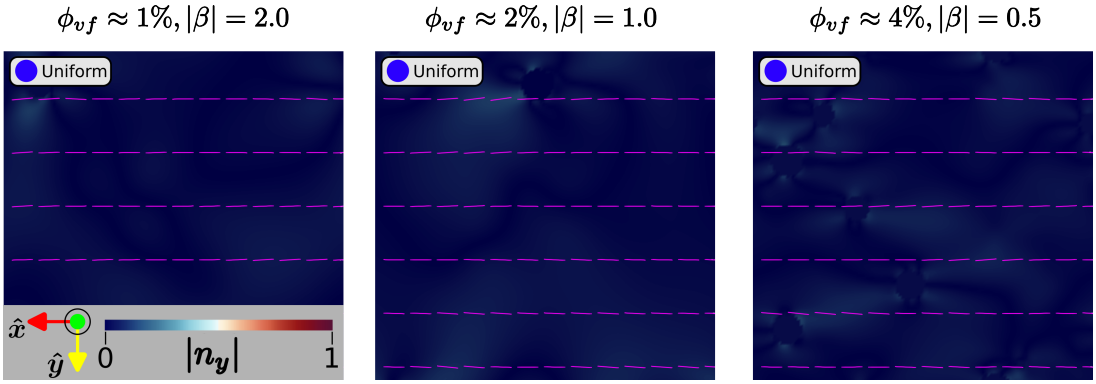

Figure 6.4: **Local perturbations increase with the activity**: For the nematic liquid crystal with pushers, the director field corresponding to various steady uniform states are presented. Within the uniform states, an increase in global activity, either by increasing the pusher volume fraction ϕ_{vf} or the squirmer parameter $|\beta|$, leads to more localized perturbations in the director field (represented by light white shading). However, the global nematic alignment remains unaffected and uniform. Directors are depicted in pink, and the color bar corresponds to the absolute value of the director component along the y-axis, denoted as $|n_y|$.

Beyond a critical global activity, the coupling between the swimmer flow fields and the nematic order gave rise to a flow instability. As a result of arising flow instability, we observed a spontaneous chiral symmetry breaking in the system; a continuous twist developed in the director field, leading to cholesteric-like structure. Because of its helical director field arrangement (similar to the one in Figure 2.4), we named this state the "Helical state". However, at even higher activity, this chiral state disappeared and topological defects (disclinations) appeared in the system. This "Chaotic state" lacked any clear spatial symmetry, and the particle dynamics became unpredictable in this state. We will first explore the Chaotic state, and then we will look at the Helical state in detail.

6.2.2 | Chaotic state

At high activity (high volume fraction or force dipole strength), the coupling between the swimmer flow fields and the nematic order led to the emergence of disclination lines in the system. The director field, which was initially aligned along the x-axis (as shown in Figure 6.2), exhibited significant spatial variations throughout the system, as shown in Figure 6.5. These abrupt spatial changes in director orientations resulted in the formation of disclination lines. Topological defects were also observed in the chaotic states of our quasi-2D simulations (Figure 5.4).

In quasi-2D simulations, the chaotic states exhibited straight disclination lines that appeared as $\pm 1/2$ point defects (see Figure 5.4). However, in 3D, chaotic states exhibited

curved disclinations (highlighted in red in Figure 6.5 and 6.6). Previous studies have indicated that activity disrupts the uniform nematic order, and leads to turbulent states [50, 53, 56, 57] characterized by $\pm 1/2$ point defects in 2D [50, 54, 98], and curved disclination lines in 3D [55, 53, 56, 57]. Indeed, our findings are consistent with the existing literature, we observed curved disclinations in 3D (see Figure 6.5 and 6.6). We further observed that the number and length of disclinations increased with increasing activity. This is shown in Figure 6.6, where the increase in swimmer volume fraction ϕ_{vf} results in more disclinations.

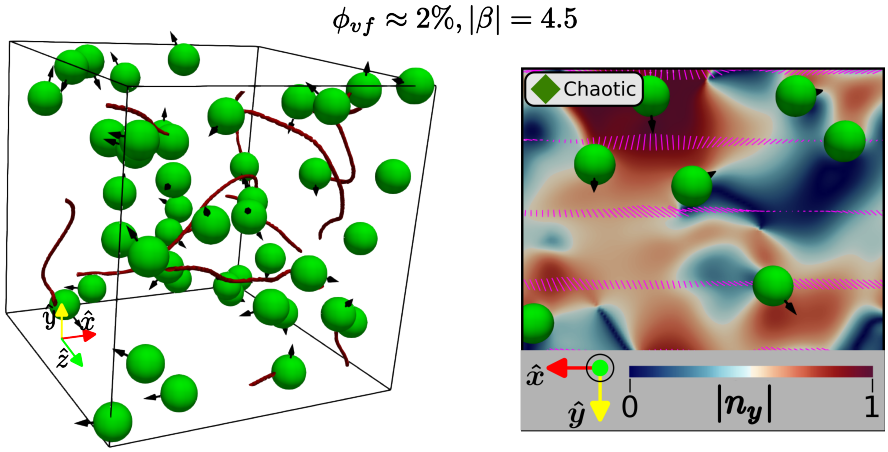

Figure 6.5: **Chaotic state**: For nematic liquid crystal with pushers, an example of Chaotic state, observed at pusher volume fraction $\phi_{vf} \approx 2\%$ and $|\beta| = 4.5$. On the left, a snapshot of the 3D simulation box is shown with disclination lines (colored in red) and pushers (in green). At high activity, the director field lacked any clear spatial symmetry, the abrupt change in director orientation resulted in the defects formation. The pushers are observed to align along the local nematic director. In the right figure, the director field is visualized at a random xy-plane, with the color bar representing the absolute value of the director component along the y-axis, denoted as $|n_y|$. The particles shown are close to the xy-plane. Disclination lines are visualized with the isosurface of the scalar order parameter $s = 0.27$.

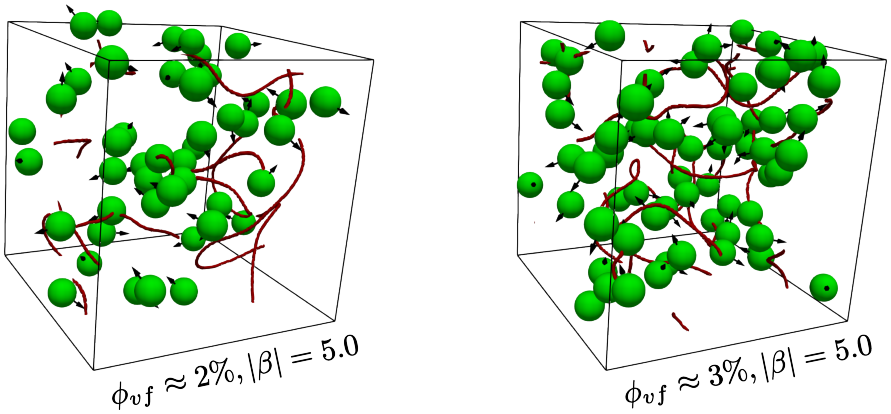

Figure 6.6: **Increase in disclinations with activity:** For the nematic liquid crystal with pushers, the figure compares systems with different pusher volume fractions, $\phi_{vf} \approx 2\%$ and 3%, and same squirmer parameter $|\beta|$. The disclinations (highlighted in red) increase with the activity (here achieved by increasing ϕ_{vf}).

In the uniform states, pushers aligned parallel to the local nematic director $\hat{\mathbf{n}}$ and exhibited linear apolar motion, swimming along $\hat{\mathbf{n}}$ and $-\hat{\mathbf{n}}$ (represented by red and blue arrows in Figure 6.3). However, in chaotic states, the spatially varying director field led to complex and irregular swimmer trajectories. The pushers still aligned with the local director $\hat{\mathbf{n}}$ (black arrows in Figure 6.5 and 6.6), but their motion lacked a well-defined trajectory, because of spatial changes in the director orientation.

6.2.3 | Helical states

As the global activity in the swimmer/nematic system was increased (by increasing swimmer numbers or force dipole strength), the initially aligned nematic became unstable, and we observed a spontaneous emergence of a continuous twist in the director field. We labeled this state the Helical state (an example is shown in Figure 6.7). This Helical state is particularly unique, because it exhibits a cholesteric-like order, similar to that seen in cholesteric liquid crystal (see Figures 2.6 and 6.7).

$$\phi_{vf} \approx 1\%, |\beta| = 4.0$$

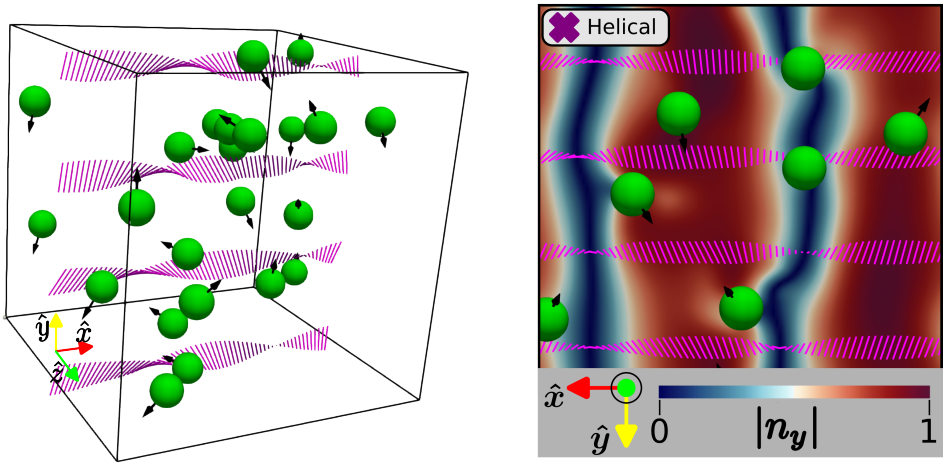

Figure 6.7: **Helical State**: For the nematic liquid crystal with pushers, an example of the Helical state, observed at the pusher volume fraction $\phi_{vf} \approx 1\%$ and $|\beta| = 4$, is shown. In the left figure, at steady state, a snapshot of the 3D simulation box is presented with directors (colored in pink) and pushers (in green). A continuous twist along the x-axis is observed in the director field. The pitch of the helical director field is approximately equal to the box length. The pushers are observed to align with the local nematic director. In the right figure, the director field is visualized at a random xy-plane, with the color bar representing the absolute director component along the y-axis, $|n_y|$. Variations in $|n_y|$ are observed along the x-axis; in the y-axis, $|n_y|$ is not varying significantly.

At the onset of the Helical state, we observed the helical director field with a continuous twist along the same axis as the initial nematic alignment (x-axis in our case). To investigate the influence of initial alignment, we performed another simulation with the same parameters but with the different initial director field alignment, along the y-axis. In this case, the continuous twist was observed along the y-axis, which demonstrated that

the initial nematic alignment determines the orientation of the helical axis in the Helical state. As expected, with our same initial alignment (along x-axis, see Figure 6.2) in 3D simulations, we consistently observed the continuous twist to be along the x-axis, as shown by the three examples in Figure 6.8.

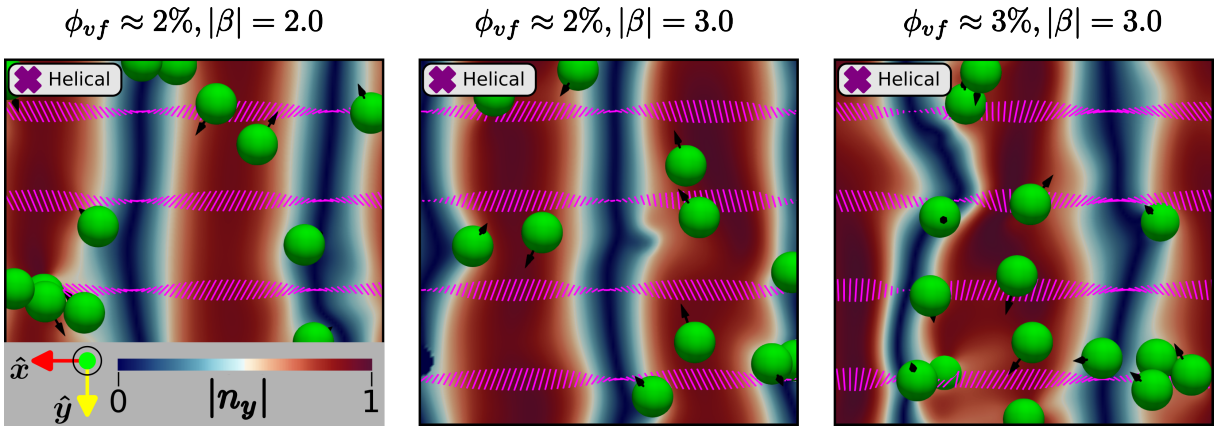

Figure 6.8: **Examples of helical states**: For the nematic liquid crystal with pushers, some examples of the helical states observed at different volume fractions and $|\beta|$ are presented. The snapshots show the director field at steady state, with directors represented in pink and particles shown as green spheres. A continuous twist is observed in the helical states, with the pitch length equal to the box length. The pushers are observed to align with the local nematic director.

The collective effects of the pusher swimmers induced a transition in the nematic liquid crystal; from the uniform nematic to a helical (chiral) state. This transition also influenced the dynamics of the pushers. In uniform states, pushers aligned with the local nematic director and moved in straight lines (refer to Figure 6.3). In chaotic states, pushers aligned with the local nematic director but exhibited irregular trajectories. Interestingly, in the helical states with helical twist along the x-axis, pusher trajectories were observed to be helical (as shown in Figure 6.19) along the same axis (x-axis). This behavior can be explain by the pusher's tendency to swim along the local nematic director [39]. In the helical state, the local nematic director rotates along the helical axis (see in Figure 6.7). Thus, the pusher consistently aligns with the local nematic director as it moves along this axis, resulting in a helical trajectory. Further discussion on pusher dynamics will be presented later in Section 6.5.

We consistently observed helical states across a range of swimmer volume fractions ϕ_{vf} and squirmer parameter $|\beta|$. To gain deeper insights into the characteristics of these states, next, we analyze the properties of the helical director field present in these states, such as the pitch length P and tilt angle α. These parameters describe the spatial periodicity and the inclination of the helical twist (w.r.t the helical axis), respectively (see cholesteric phase in Section 2.2.2).

Characterization of the continuous twist in helical states

As mentioned earlier, the Helical state closely resembles the cholesteric state. The continuous twist structures in both look similar, but there is a difference in the director orientations. In both, a continuous twist defines the director field, but the tilt angle of the directors relative to the helical axis differs. We compare a single twist from both in Figure 6.9. In cholesteric phase, the directors are perpendicular to the helical axis (x-axis), meaning the tilt angle $\alpha = 90°$. As per the helical configuration $\hat{\mathbf{n}}(\mathbf{r}) = (\cos\alpha,\ \sin\alpha\cos qx,\ \pm\sin\alpha\sin qx)$, the x-component of the director vanishes ($n_x = 0$) in cholesteric twist (see director components in Figure 6.9). Interestingly, in the Helical state, we observe that the directors are not exactly perpendicular to the helical axis (x-axis); the tilt angle is less than 90°, resulting in non-zero n_x values (see Figures 6.9 and 6.10). Within a helical twist (corresponding to a Helical state), we observed small fluctuations in the n_x values (see Figure 6.10). Furthermore, with increasing activity (left to right in Figure 6.11), the average n_x decreased. Since $n_x = \cos\alpha$ in the helical configuration, this decrease indicates a slight increase in the tilt angle α with increasing activity (see Figure 6.12).

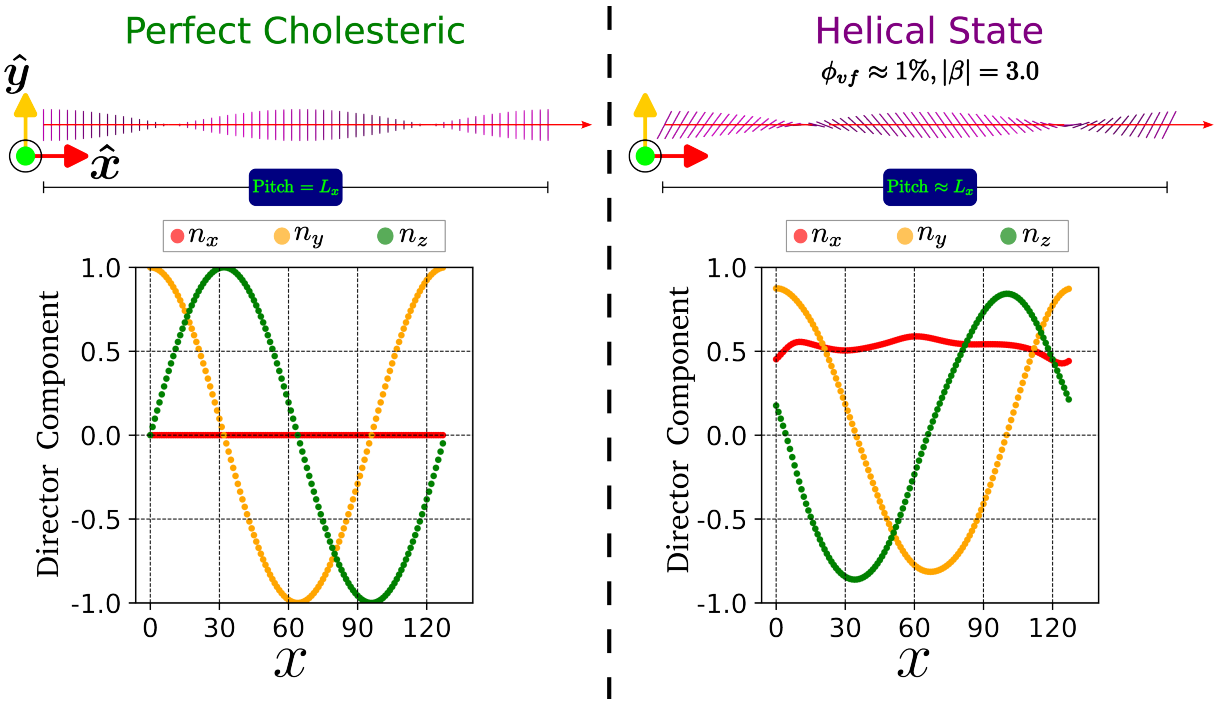

Figure 6.9: **Comparing continuous twist in the Cholesteric and the Helical state**: The figure compares an isolated continuous twist from the cholesteric liquid crystal and the helical state (observed at $\phi_{vf} \approx 1\%$ and $|\beta| = 3$). Pink lines represents the director. Also, the director components n_x, n_y, n_z are plotted as a function of the x-coordinate. For helical director fields, $n_x = \cos\alpha$, $n_y = \sin\alpha\cos qx$, and $n_z = \pm\sin\alpha\sin qx$, with $q = 2\pi/P$. The pitch length P = 128 is the same for both cases; only the tilt angle is observed to be different. In perfect cholesteric, the directors are perpendicular to the helical axis (i.e., $\alpha = 90°$) and $n_x = 0$. In the helical state, the directors are not perpendicular to the helical axis, which gives $n_x \neq 0$, and the n_x is fluctuating around 0.5.

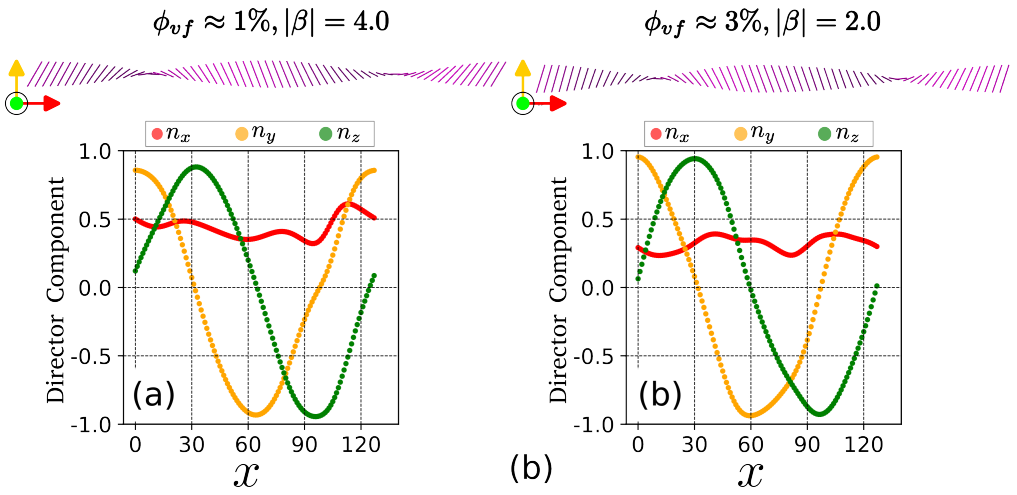

Figure 6.10: **Helical configuration in the helical states**: The figure compares the continuous twist corresponding to various helical states, observed at different pusher volume fraction ϕ_{vf} and $|\beta|$. The director components $\hat{n} = (n_x, n_y, n_z)$ corresponding to the twist are plotted as a function of x-coordinate. The average $n_x \approx 0.45$ for $\phi_{vf} \approx 1\%$ and $|\beta| = 4$, while the average $n_x \approx 0.3$ for $\phi_{vf} \approx 3\%$ and $|\beta| = 2$. This decrease is due to an increase in the global activity $\zeta \sim \phi_{vf} B_2$.

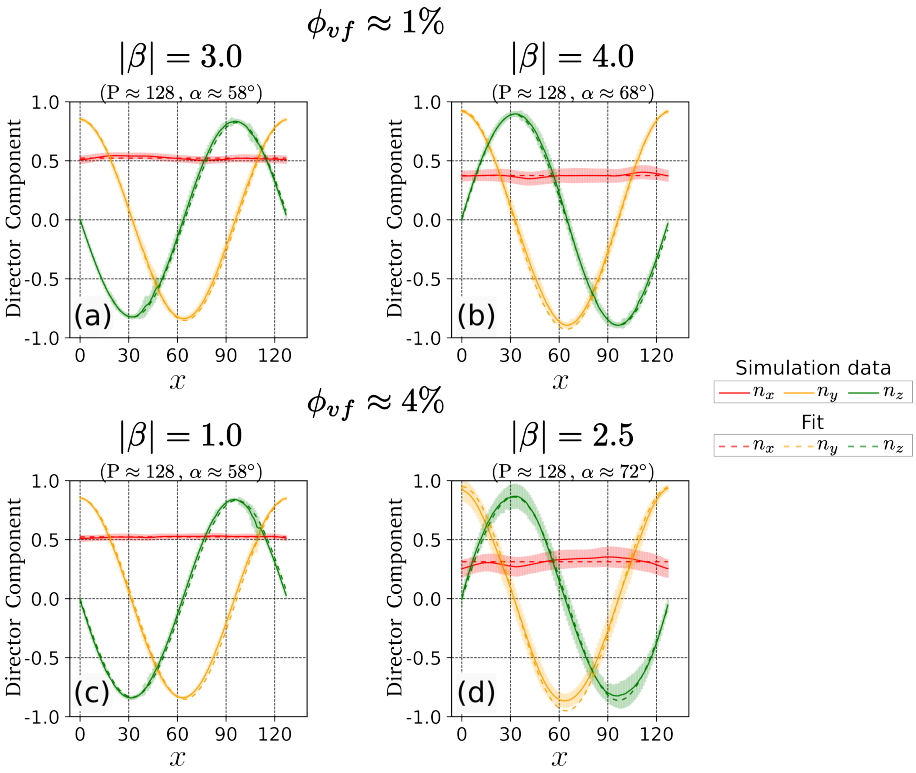

Figure 6.11: **Fitting helical director field**: The figure shows a few examples of the director components n_x, n_y, and n_z along the x-axis (solid lines) from various helical states. The components are averaged over yz-planes and fitted by the director field corresponding to the helical configuration $n_x = \cos\alpha$, $n_y = \sin\alpha \cos qx$, and $n_z = \pm \sin\alpha \sin qx$, with $q = 2\pi/P$. The helical states in subfigure (b) and (d) show right handed twists, and in subfigure (a) and (c) show left handed twists. The dashed lines show the best fit using the pitch P and tilt angle α. The α is observed to increase with the global activity ($\zeta \sim \phi_{vf} B_2$), while P $\approx$ 128 across the helical states. At a fixed pusher volume fraction ϕ_{vf}, the variations within yz-planes (represented by vertical lines) are more pronounced for higher $|\beta|$.

Across all helical states, the tilt angle α never reached 90°, indicating that the directors were never perfectly perpendicular to the helical axis. The x-component of the director n_x remained non-zero (shown in Figures 6.10 to 6.12). The continuous twist oberved along the x-axis and the director field maintained a relatively uniform (in aspect of director components) within the yz-plane (Figures 6.7 and 6.8). To further analyze the director field, we calculated the average of each director component (n_x, n_y, n_z) across each yz-plane at steady states. Plotting these averaged components as a function of the x-coordinate (Figure 6.11) revealed larger deviations from the average director components, for higher force dipole strengths ($|\beta|$), (see Figure 6.11). This is understandable because a higher force dipole strength intensifies local fluid mixing around the swimmers, causing stronger local perturbations in the director field.

To calculate the pitch length P and the tilt angle α of the helical twist, we fitted the averaged director components with the helical configuration: $n_x = \cos\alpha$, $n_y = \sin\alpha\cos qx$, and $n_z = \pm\sin\alpha\sin qx$, (where $\pm$ corresponds to left and right-handed helices). As the activity increased, the tilt angle α was observed to increase slightly, within the range 55° to 72°, shown in Figure 6.12. Interestingly, the pitch length P remained relatively constant at ≈ 128, giving $q = 2\pi/\mathrm{P} \approx 0.049$ (purple in Figure 6.12). The consistency is likely due to the periodic boundary conditions imposed on the simulaion box, which restrict P to be a multiple of the box length $L = 128$.

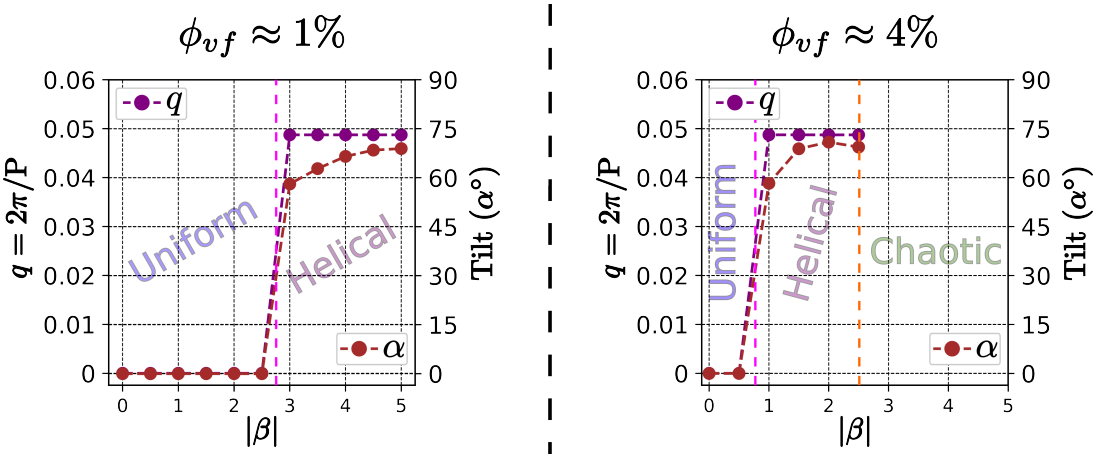

Figure 6.12: **Variation of pitch length and tilt with the squirming strength**: For nematic liquid crystals with pushers, the figure presents the variation in the pitch length P and the tilt angle α as a function of the squirmer parameter β, for pusher volume fractions $\phi_{vf} \approx 1\%$ and 4%. At the onset of the instability, P and α are observed to be non-zero in the helical states. Within the helical states, the tilt angle α is observed to increase slightly, while the pitch length remains ≈ 128, giving $q \approx 0.49$ across the helical states.

In 3D nematic liquid with pushers, the coupling between the swimmer flow fields and the nematic order gave rise to a flow instability, which led to the formation of a helical twist in the director field. In the next section, we analyze various types of distortions observed in the director field across different states (Uniform, Helical, and Chaotic) to understand the nature of instability.

6.2.4 | Analysis of director field distortions

After analyzing the helical states, we now look at the various deformations (e.g, twist, bend and splay) across different states. We time averaged the deformation densities over steady states for simulated volume fractions ϕ_{vf} and squirmer parameter $|\beta|$ (shown in Figure 6.13). As expected, the uniform nematic states with stable uniform nematic order exhibited minimal twist, bend and splay deformations (see Uniform region in Figure 6.13). This is because, the perturbations in the director field were localized around the swimmers. The collective effects of the pusher population were not strong enough to disturb the global uniform nematic alignment (see Figures 6.3 and 6.4).

When the global activity was increased beyond critical value (by increasing ϕ_{vf} or $|\beta|$), we observed an emergence of flow-induced orientational instability, which transitioned the Uniform state into the Helical state, characterized by the helical director field. This spontaneous chiral symmetry breaking caused a sudden growth in distortions (see Helical region in Figure 6.13). Within the helical states, twist distortions were significantly higher than bend and splay distortions. At even higher activity, helical states transitioned into chaotic states, which is marked by non-zero defect densities in Figure 6.13. In chaotic states, bend and splay distortions significantly increased, while twist slightly decreased, but both twist and bend distortions remained dominant compared to splay (see Chaotic region in Figure 6.13).

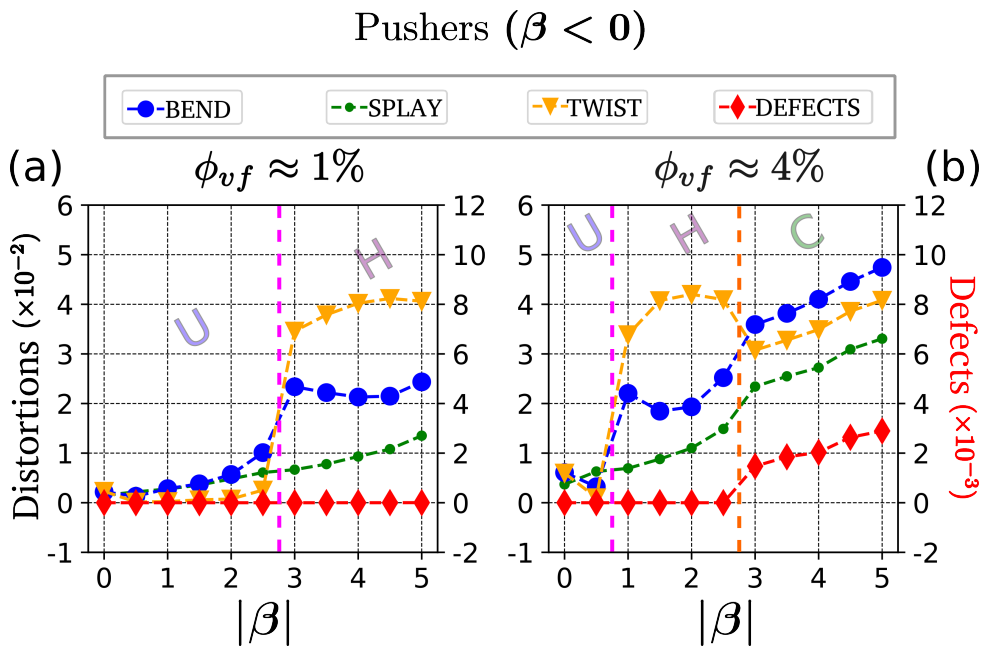

Figure 6.13: **Distortion and defect densities**: For nematic liquid crystals with pushers, the figure shows distortion and defect densities as functions of the squirmer parameter β, for pusher volume fractions $\phi_{vf} \approx 1\%$ and 4%. The values are time averaged over steady states. The distortions are minimal in the uniform states. At the onset of the instability, there is a sudden increase in the distortion densities. Within the helical states, twist distortions are the highest, followed by bend distortions. In chaotic states, defect density is non-zero, and increasing with $|\beta|$.

Across the helical states, we observed a slight increase in twist with the squirming strength $|\beta|$ (see twist in Figure 6.13). This is likely caused by the increasing tilt angle α within the helical states, as seen in Figure 6.12. Using the Oseen-Frank formalism, we can approximate the twist deformation $T = \hat{\mathbf{n}} \cdot \nabla \times \hat{\mathbf{n}}$ for a helical configuration as $|T| \sim q \sin^2 \alpha$. Since the pitch length (q) remained relatively constant in the helical states (refer to Figure 6.12), this analysis suggests that observed increase in twist is primarily caused by the increasing tilt angle.

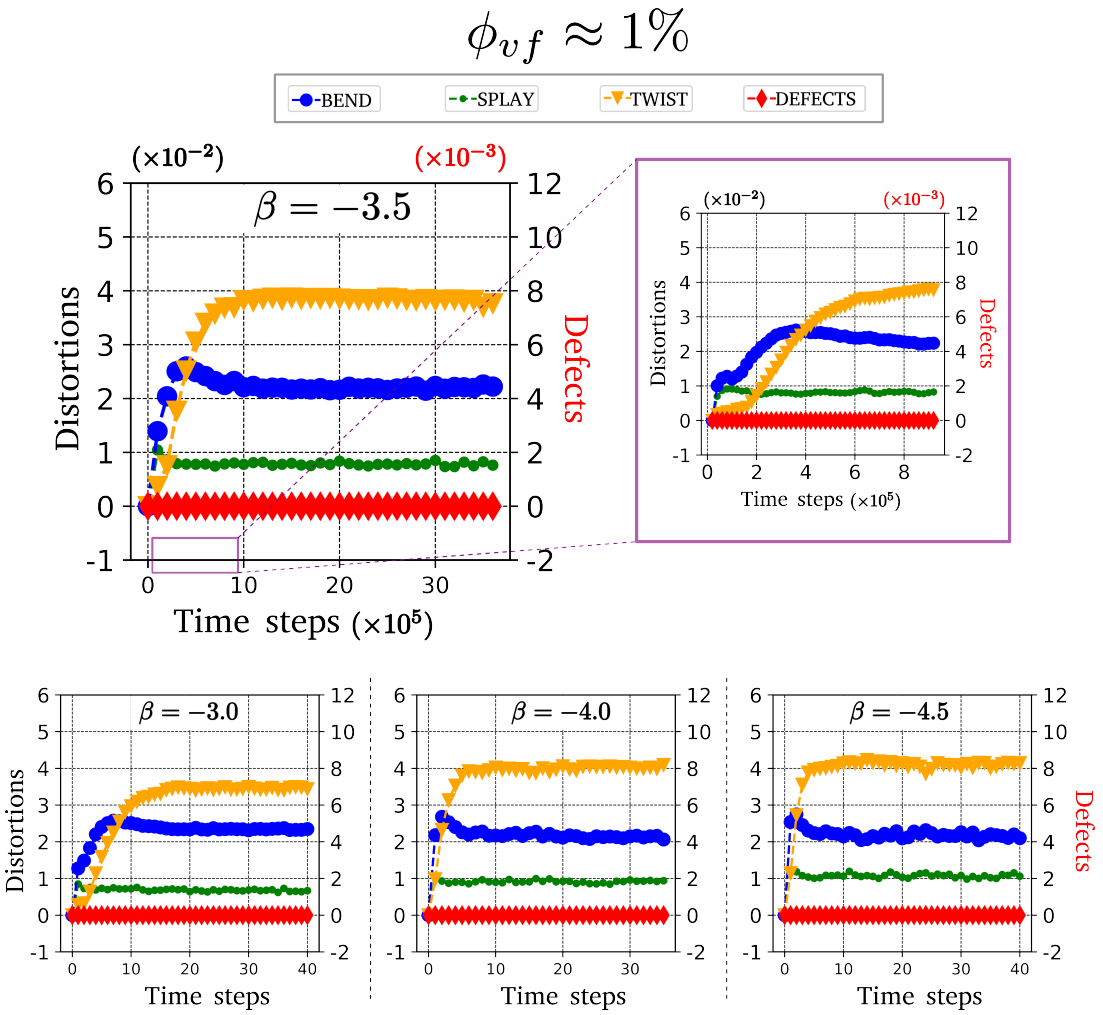

Figure 6.14: **Time evolution of deformations in the helical states**: The figure shows the time evolution of distortions and defect densities for various helical states observed with the swimmer volume fraction of $\phi_{vf} \approx 1\%$. At the squirmer parameter $|\beta| = -3.5$, the zoomed region in the purple box depicts the deformation growth over time in the early stages of the simulation. The trend in deformation growth remains consistent across the helical states. Initially, splay and bend deformations are observed in the system. First, splay is observed to reach a constant value. For a brief time period, bend grows at a higher rate than twist. Within $\approx 10^6$ time steps, twist surpasses bend, and reach a constant value (a continuous twist forms in the director field).

When the deformations are plotted as a function of time (shown in Figure 6.14), an interesting trend is observed. Early in the simulation, the flow instability induced splay and bend deformations in the system (see Inset in Figure 6.14). The splay deformation plateaued before the bend. For a brief period, the bend continued to grow at a higher rate

than the twist. However, the twist eventually surpassed the bend and reached a steady value (yellow lines in Figure 6.14). This marks the spontaneous chiral symmetry breaking and formation of continuous twist in the director field. The time to reach this steady helical state varied across ensembles, but it can be estimated to be 10^6 time steps, which tells us that particles travel approximately 1000 lattice sites or 80 particle lengths (given the swimming speed $u_0 = 10^{-3}$ in lattice units) before a steady continuous twist emerges in the director field.

In 3D nematic liquid crystals with pushers, we observed that the uniform nematic order is unstable, and the flow instability leads to the spontaneous formation of continuous twist in the director field (see Figures 6.7 to 6.12). The sudden growth of twist and bend distortions, compared to splay, at the transition between the uniform and helical states (Figures 6.13 and 6.14) strongly suggests that the most unstable mode is a twist-bend mode. Interestingly, the twist distortions were approximately twice as large as bend distortions and four times that of splay distortions (see Figures 6.13 and 6.14). From an energy point of view, the deformations cost is non-zero, in terms of the elastic free energy (refer to Equation 2.11). So, why did the system favor twist-bend distortions?

Linear stability analysis of 3D extensile active nematic systems has predicted twist-bend as the dominant instability [55, 53]. Extensile systems have particle that pushes the fluid outwards along its axis, similar to the flow generated by our pusher particles. Thus, for our active ordered system with extensile pushers, this analysis suggests that the twist-bend mode is the most unstable. Indeed, we observed unstable growth in twist and bend deformations within our system (see Figures 6.13 and 6.14).

6.3 | Pullers in 3D nematic liquid crystal

In the previous sections, we discussed systems with pusher swimmers. We observed that the coupling between swimmer flow fields and the nematic order led to a spontaneous chiral symmetry breaking in the system; the uniform nematic order became unstable, and a continuous twist spontaneously formed in the director field (see Figures 6.7 to 6.12). Now, we ask: what happens when the suspended swimmers are not pushers (extensile) but pullers, which are characterized by contractile flow fields? Will we observe a similar transition from a uniform nematic state to a cholesteric-like state? will the twist-bend mode remain the dominant instability? Based on the fundamental difference in flow fields of pushers and pullers, our hypothesis is that the transition will be different and the splay deformation will grow in the system, since it has been predicted to be dominant for contractile active nematics [49].

To test our hypothesis, we conducted simulations of 3D nematic liquid crystals with puller populations using the same volume fractions and the squirmer parameter (β) used for pushers. The only difference was the sign of the force dipole coefficient B_2 within $\beta = \frac{B_2}{B_1}$.

For pullers only $B_2 > 0$ values were used, which correspond to contractile flow fields. The results are summarized in Figure 6.15. Similar to the pusher case, a spontaneous transition to a cholesteric-like state was observed. At low global activity, the uniform nematic order remained stable. However, beyond a critical activity, a hydrodynamic instability developed, which led to the emergence of a continuous twist in the director field. Interestingly, the critical force dipole strength ($|\beta|$) at a given volume fraction remained similar for pullers and pushers (see state diagram, Figure 6.21). At even higher activities, system lost the cholesteric-like order (Figure 6.15) and disclinations appeared in the chaotic states.

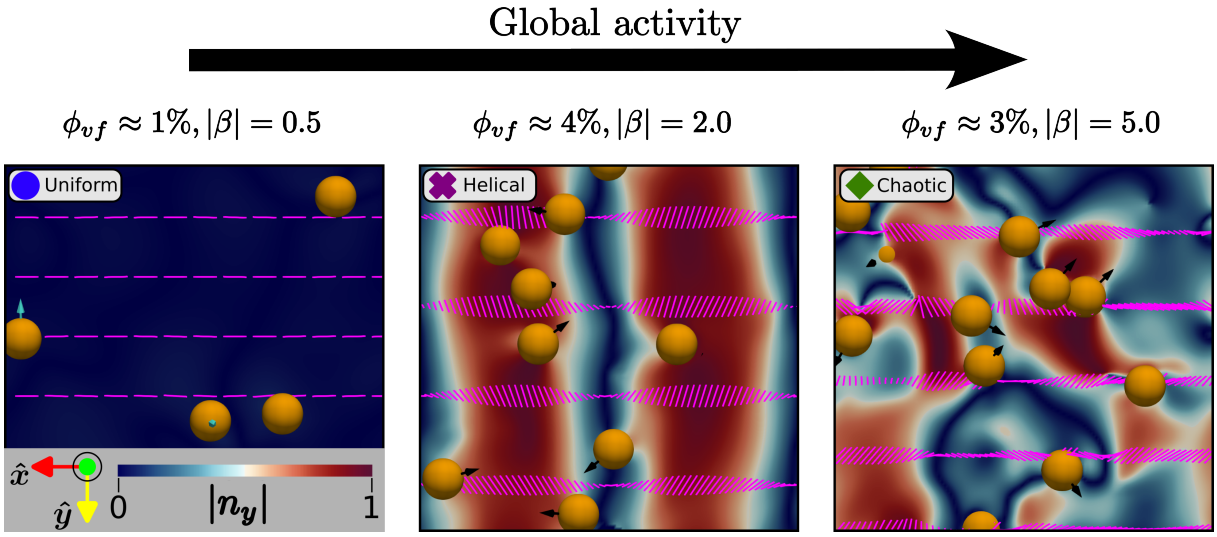

Figure 6.15: **Activity-triggered transition in the nematic liquid crystal with pullers**: The figure summarizes the state transition observed in the system consisting of puller microswimmers (orange spheres) in the nematic liquid crystal. The color bar corresponds to the absolute value of the director component along the y-axis, denoted as $|n_y|$. With an increase in global activity, either by increasing the puller volume fraction ϕ_{vf} or the squirmer parameter β, a transition in the director field is observed, from Uniform to Helical and to Chaotic states. In the Uniform state (leftmost), the director field (depicted in pink) is uniformly aligned along the x-axis. In the Helical state (middle), the director field has a continuous twist around the x-axis. In the Chaotic state, the director field exhibits no clear spatial symmetry, and topological defects have appeared. The pullers swim perpendicular to the local nematic director across the states.

The helical (chiral) states observed with pullers showed remarkable similarities to those with pushers. Notably, the continuous twist in both cases was observed along the same axis (x-axis, see Figure 6.15 and 6.7), also the number of left and right handed ensembles were (almost) equal in both cases (Figure 6.21). Specific helical properties like tilt angle (α) and pitch length (P) also displayed comparable values (for pushers see Figure 6.12 and for pullers see Figure 6.16). Pitch length consistently remained P $\approx$ 128 (likely due to periodic boundary conditions), and α values varied within a narrow range.

Similar qualitative trends were observed in the distortion analysis of both systems with pushers and pullers (Figures 6.17 and 6.13). Both systems showed minimal distortions in the uniform states, followed by a sudden increase in deformations at the onset of instability. Within the helical states, twist distortions were significantly larger than both bend and

splay distortions, with a ratio of 2:1 and 4:1, respectively. Interestingly, twist deformations became even more pronounced in the chaotic states with a puller population (see Chaotic region in Figure 6.17).

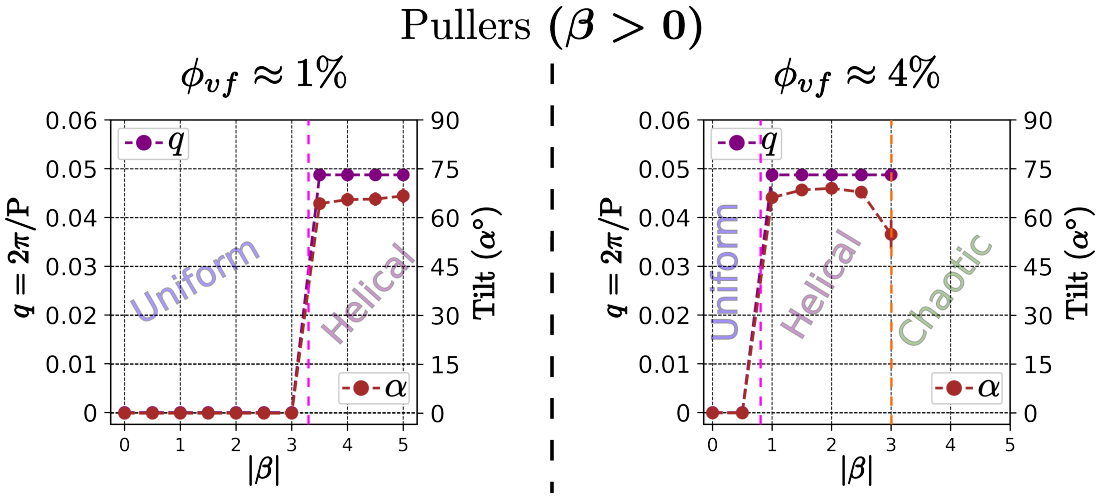

Figure 6.16: **Variation of pitch length and tilt with the squirming strength**: For the nematic liquid crystal with pullers ($\beta > 0$), the plot shows the dependence of pitch length (P) and tilt angle (α) on the squirmer parameter β. For both puller volume fractions $\phi_{vf} \approx 1\%$ and 4%, the α is observed to mostly increase with increase in $|\beta|$, while P remains ≈ 128, giving $q \approx 0.49$ across the helical states.

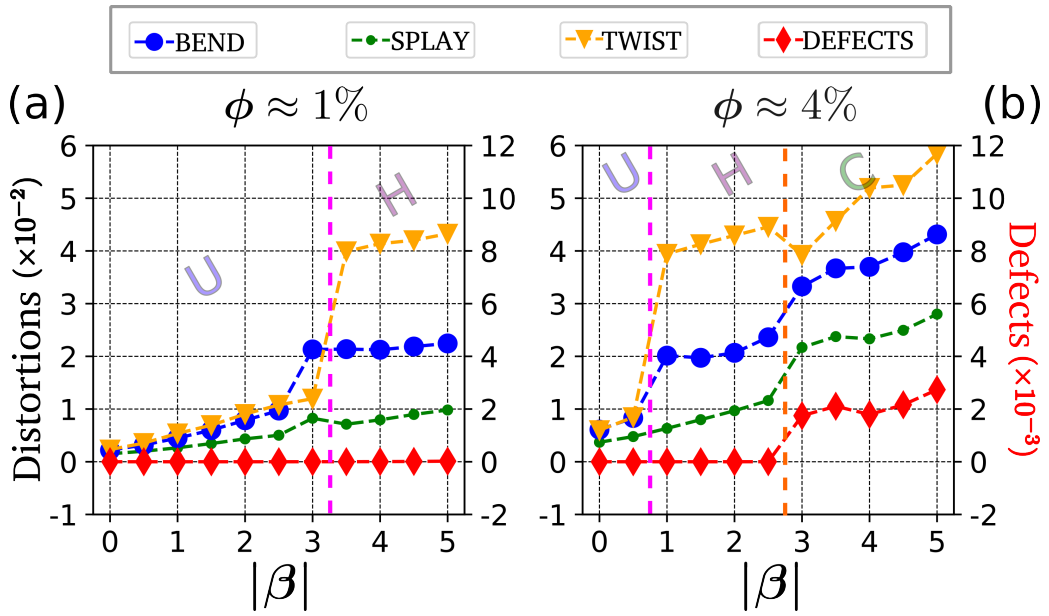

Figure 6.17: **Distortion and defect densities**: For the nematic liquid crystal with pullers, the plot presents distortion and defect densities as a function of the squirmer parameter β, for puller volume fractions $\phi_{vf} \approx 1\%$ and 4%. Distortions are minimal in the uniform states. At the onset of the instability, there is a sudden increase in the distortion densities. Within the helical states, twist distortions are the highest, followed by bend distortions. In chaotic states, defect density is non-zero, and observed to increase with $|\beta|$.

The hydrodynamic torque in the nematic liquid crystal orients a puller perpendicular to the nematic director [39]. This behavior was observed in our simulations, although the puller trajectories varied across different states. In uniform states, with directors aligned along the x-axis, pullers moved within the yz-plane (see particle orientations in Uniform state, Figure 6.15) and in straight lines. In chaotic states, where director orientations varied spatially without any specific pattern, pullers aligned themselves perpendicular to the local nematic director, exhibiting irregular trajectory patterns. Interestingly, helical states, characterized by a continuous twist in the director field, induced helical motion in the pullers (as shown in Figure 6.19). This is because, the puller continuously aligns perpendicular to the local nematic director as it moves along the helical axis, ultimately resulting in a helical trajectory. Further details on these trajectories will be discussed in the section 6.5.

Having explored the systems with pullers, we can now turn our attention to understand, why did both puller and pusher systems exhibit the same twist-bend instability?

6.4 | Dominance of twist-bend instability in 3D.

Linear stability analysis has predicted the dominant growth of twist-bend deformations in 3D active nematics with extensile flows [55]. This prediction is directly relevant to our simulations involving pushers, as their flow field exhibits extensile nature (fluid is pushed along the particle axis). Indeed, our findings for pushers align with the theoretical predictions [55]; our data showed the dominance of twist-bend instability, evidenced by the highest growth of twist and bend deformations (see Figure 6.13).

Surprisingly, both pusher and puller systems exhibited twist-bend instability as the dominant mode (Figure 6.17 and Figure 6.13). This finding seems counterintuitive at first glance, considering the distinct flow fields generated by pushers (extensile) and pullers (contractile). Intuitively, one might expect splay deformations to be dominant in puller systems, as suggested by theoretical studies on contractile active nematics [49].

The unexpected similarity between systems with pushers and pullers is understood by considering the preferred swimming directions of the swimmers within the nematic liquid crystal. A pusher swims along the nematic director, while a puller moves perpendicular to it [39]. Interestingly, when a puller aligns its contractile (inward) force dipole perpendicular to the local nematic director, the flow along the nematic director corresponds to that of an extensile (outward) force dipole, which is the case for pushers (see Figure 6.18). This explains why, despite having different flow field types, pusher and puller systems exhibit the same twist-bend instability (see, for pushers Figure 6.13 and for pullers Figure 6.17).

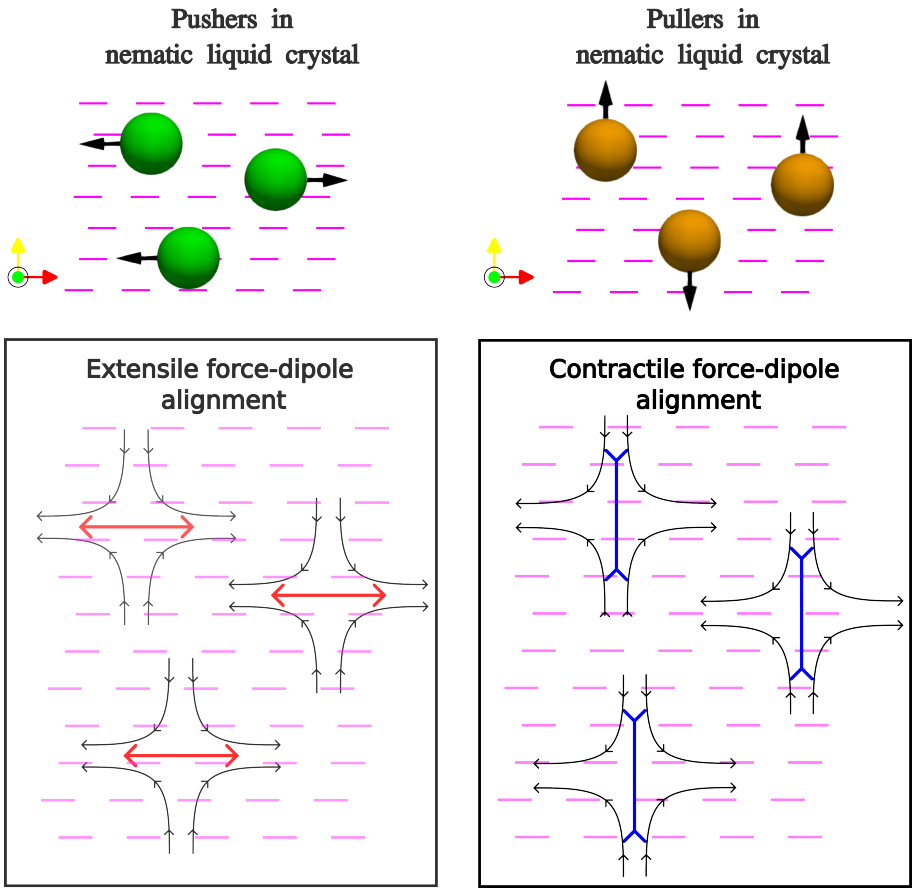

Figure 6.18: **Force-dipole alignment in the nematic liquid crystal:** The sketch illustrates the alignment of force dipoles for pusher (extensile) and puller (contractile) swimmers in a nematic environment. As a pusher moves along the local nematic director, its extensile force dipole (in red) aligns parallel to the director. In contrast, a puller, moving perpendicular to the nematic director, aligns its contractile force dipole (in blue) perpendicular to the director. The perpendicular alignment of an inward (contractile) force dipole approximately corresponds to the parallel alignment of an outward (extensile) force dipole.

6.5 | Squirmer dynamics in helical states

In 3D nematic liquid crystals with spherical microswimmers, above a critical activity, we observed the formation of a helical twist in the director field. Since the particle dynamics and director orientations are connected, this twist significantly impacted the swimmers trajectories. As shown in Figure 6.19, both pusher and puller swimmers exhibited apolar helical motion in the Helical state, meaning swimmers moving parallel and antiparallel to the helical axis (x-axis) were balanced. Interestingly, the pitch length of their helical trajectories matched the pitch length of the continuous twist, regardless of swimmer type. However, there was a notable difference between pusher and puller trajectories; at the same volume fraction and the squirming strength ($|\beta|$), the pusher swimmers displayed helical trajectories with larger radii compared to pullers (see Figures 6.19 and 6.20).

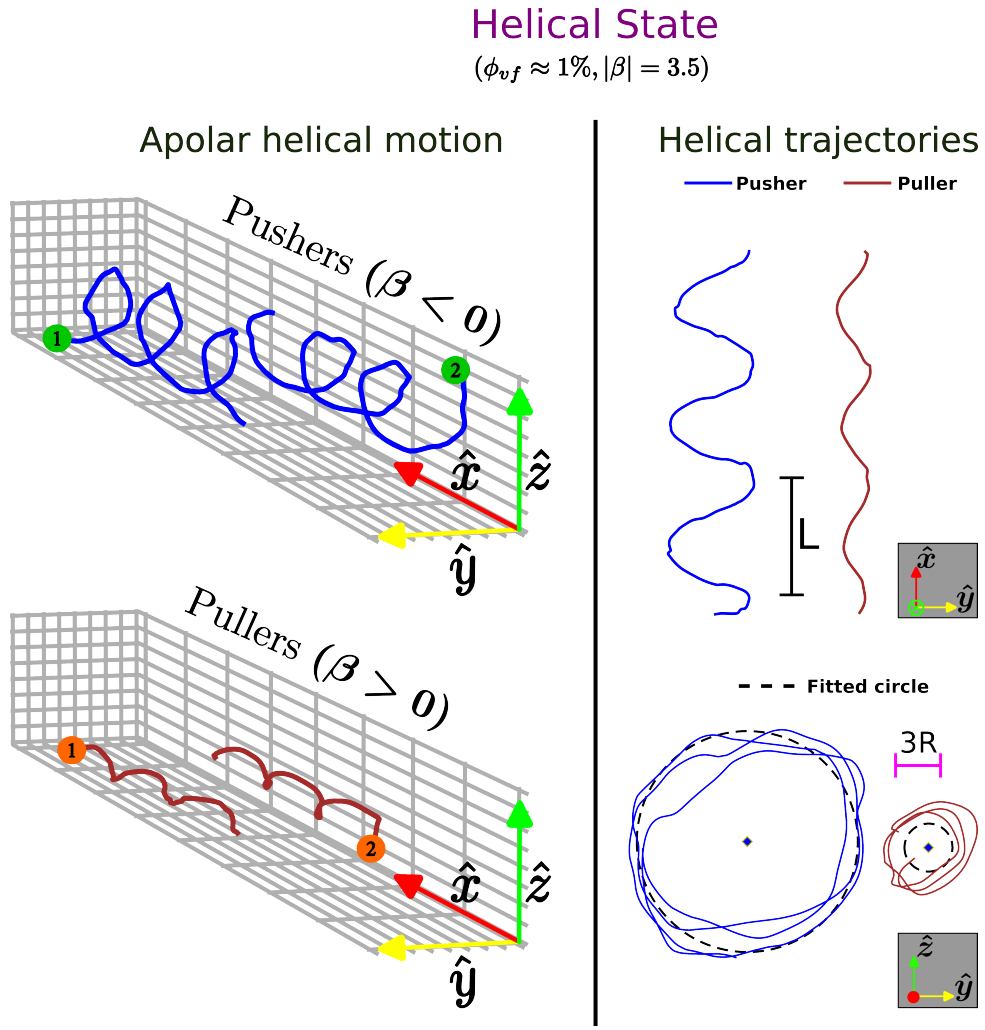

Figure 6.19: **Particle dynamics in the Helical state**: At the same volume fraction $\phi_{vf} \approx 1\%$ and squirming strength $|\beta| = 3.5$, a Helical state observed for nematic liquid crystal with pushers and with pullers. The figure compares the helical trajectories of pushers (in blue) and pullers (in brown) in the helical states. Regardless of the squirmer type, particles exhibit apolar motion. The black scale bar corresponds to the box length ($L \approx 21R$), and the pink scale bar corresponds to $3R$. Both pusher and puller trajectories have a similar pitch length, P ≈ L. The fitting of the pusher trajectory gives the radius of helix $\approx 7R$, and for the puller trajectory, the radius of helix $\approx 1.5R$. Fitted circles (dashed black lines) agree well with the observed trajectories in yz-pane.

To understand the observed difference in radii, let's look at the particle dynamics analytically. Consider a Helical state with a defined tilt angle α and pitch P, where the helix is right-handed and is along the x-axis. As discussed earlier, the director components follow, $n_x = \cos\alpha$, $n_y = \sin\alpha\cos qx$, and $n_z = \sin\alpha\sin qx$, with $q = 2\pi/\mathrm{P}$. For a pusher spherical swimmer that prefers to swim parallel to the nematic director [39], the orientation vector $\hat{\mathbf{m}}$ at the position (x, y, z) is along the local nematic director,

$$m_x = \pm\cos\alpha, \qquad m_y = \sin\alpha\cos qx, \qquad m_z = \sin\alpha\sin qx \tag{6.1}$$

where ± indicates two possible helical paths, corresponding to motion parallel and antiparallel to the helical axis.

If the pusher moves with speed u_0, then its velocity components are,

$$V_x = \pm u_0 \cos\alpha, \qquad V_y = u_0 \sin\alpha \cos qx, \qquad V_z = u_0 \sin\alpha \sin qx \tag{6.2}$$

Integrating this velocity over time t gives a helical trajectory,

$$X(t) = \pm u_0 \cos\alpha \; t \tag{6.3}$$

$$Y(t) = \tfrac{\tan\alpha}{q}(\sin q\, X(t)) \tag{6.4}$$

$$Z(t) = \tfrac{\tan\alpha}{q}(\cos q\, X(t)) \tag{6.5}$$

The radius of helical trajectory traced by a pusher ($\mathrm{ROH_{ps}}$), can be calculated as:

$$\mathrm{ROH_{ps}} = \sqrt{Y^2 + Z^2} \implies \mathrm{ROH_{ps}} = \frac{\tan\alpha}{q} \tag{6.6}$$

The radius of helix is independent of time and depends on the tilt angle (α) and pitch length (P). Using data from simulations at volume fraction $\phi_{vf} \approx 1\%$ and a squirming strength $|\beta| = 3.5$, (as shown in Figure 6.12), we obtain the radius of helix for pusher, $\mathrm{ROH_{ps}} \approx 43$, which is approximately seven times the radius of a squirmer (R). This calculated helical trajectory radius closely matches the observed trajectories of pushers in the helical state (fitted circle in Figure 6.19). Now, let's look at pullers.

We follow the same procedure to determine the radius of the puller's helical trajectory ($\mathrm{ROH_{pl}}$). While a pusher aligns with the director, a puller aligns perpendicular to it [39]. Thus, the orientation vector $\hat{\mathbf{m}}$ at the position (x, y, z) is given by,

$$m_x = \cos\alpha', \quad m_y = \sin\alpha' \cos qx, \quad m_z = \pm \sin\alpha' \sin qx \tag{6.7}$$

where $\alpha' = 90° - \alpha$. This results in a different radius of helix,

$$\mathrm{ROH_{pl}} = \frac{\cot\alpha'}{q} = \frac{1}{q \tan\alpha}$$

Using the simulation data for $\phi_{vf} \approx 1\%$ and $|\beta| = 3.5$ (from Figure 6.16), we find $\mathrm{ROH_{pl}} \approx 1.5R$. This value matches well with the observed radius of puller's helical trajectory (fitted circle Figure 6.19). This radius is significantly smaller compared to the pusher's ($\mathrm{ROH_{ps}}$) calculated earlier, highlighting the distinct effects of their swimming preferences on their trajectories within the helical state.

To determine the tilt angle α and the pitch length P of a helical state (presented in Figures 6.12 and 6.16), we fitted the director field. However, α and P can also be calculated by fitting the particle trajectories, using equations for helical motion (Equations 6.1 and 6.7). This fitting was done for both pusher and puller trajectories, and the resulting average tilt angles are presented in Figure 6.20. These values closely align with those

obtained from the director field data (Figures 6.12 and 6.16). This agreement confirms that, even though pusher and puller swimmers move in helical way, they still align themselves parallel and perpendicular to the local nematic director, as reported in [39].

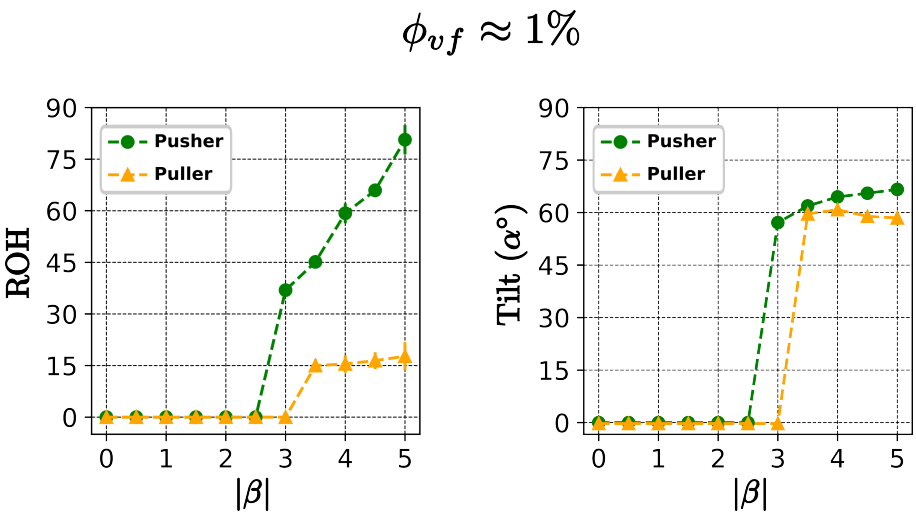

Figure 6.20: **Radius of helix and tilt (from particle trajectories) against the squirming strength**: For nematic liquid crystals with a squirmer population, the plot shows the change in radius of helix (ROH) with squirming strength $|\beta|$ for pusher (green line) and puller (orange line) trajectories. The radius of pusher's helical trajectory is observed to be higher than that of puller's trajectory. On the right, the figure shows the tilt angle (α) calculated by fitting particle trajectories as per Equations 6.1 and 6,7.

6.6 | State Diagram (3D)

We investigated the behavior of spherical microswimmers in 3D nematic liquid crystals, and observed that their collective swimming can destabilize the uniform nematic order. At low global activity, the system maintained the uniform nematic alignment. However, as the activity increased (either by increasing swimmer density or force dipole strength), the system underwent a nematic-to-helical transition, resulting in a continuous twist in the director field. This twist eventually disappeared at higher activity, because of the emergence of topological defects. The transition was observed for both pusher (extensile, $\beta < 0$) and puller (contractile, $\beta > 0$) swimmers. Figure 6.21 indicates the nature of steady states, observed at various volume fractions ϕ_{vf} and squirming parameter β.

For classifying the observed states in the liquid crystal, we established specific criteria. The uniform state exhibited a global nematic alignment with minimal spatial variations in the director field and no disclination lines (for example, see Figure 6.3). The helical state was identified by a continuous twist in the director field, with a well-defined pitch length and no disclinations (like in Figure 6.7). Finally, the chaotic state was characterized by the presence of visible disclinations (as shown in Figure 6.5). As shown in the state diagram (Figure 6.21), the transition between the uniform and helical states depends on both the

swimmer volume fraction and the squirmer parameter β. With the source dipole B_1 fixed in the definition of $\beta = \frac{B_2}{B_1}$, the transition is linked to the force dipole strength B_2.

The transition to the Helical state arises from the hydrodynamic coupling between the swimmer flow fields and the orientational order in nematic liquid crystal. The vorticity ω (measure of local fluid rotation) generated by a squirmer's flow field can reorient another nearby squirmer [84]. To estimate the torque on a squirmer at a distance r, we consider the squirmer flow field in an isotropic fluid $\mathbf{v}(\mathbf{r})$ [101], and find vorticity $\omega = \nabla \times \mathbf{v}(\mathbf{r}) \equiv -3/2 \sin 2\theta B_2/r^3 \hat{\mathbf{e}}_\xi$, where $\hat{\mathbf{e}}_\xi$ is a unit vector along the azimuthal direction. In a system with uniform density of squirmers, the average separation l between them scales as $l \sim \phi_{vf}^{-1/3}$. Using the relationship for vorticity and considering uniform density, we can approximate the activity ζ in the continuum limit as $\zeta \sim B_2 \phi_{vf}$. Assuming that the transition to the Helical state occurs only when activity exceeds a certain critical level ζ^*, we find that the critical volume fraction $\phi_{vf}^* \sim B_2^{-1}$. This relation agrees with the existing literature on active nematics [98, 40, 48] and fits the simulation data remarkably well (white lines in Figure 6.21).

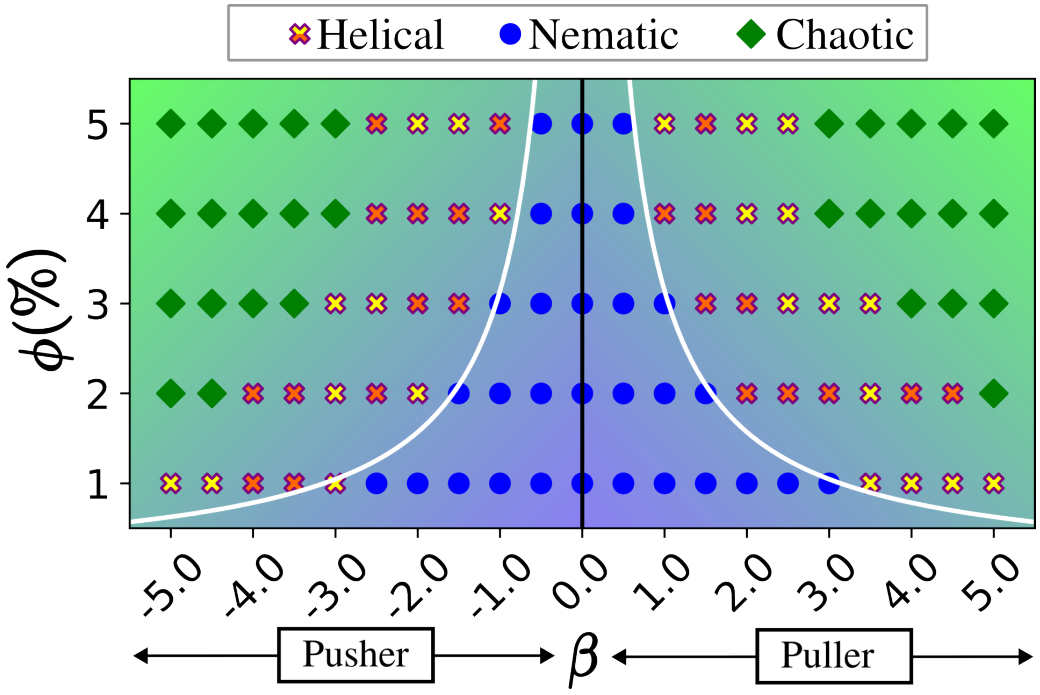

Figure 6.21: **State diagram**: For a system consisting of spherical microswimmers in a 3-dimensional nematic liquid crystal, the figure illustrates the observed steady states as a function of the swimmer volume fractions ϕ_{vf} and the squirming parameter (β). The source dipole $B_1 = 0.0015$ remains constant in $\beta = B_2/B_1$, and only the force dipole strength B_2 is changing. The blue circle represents the Uniform state, the cross denotes the Helical state, with the yellow cross indicating a left-handed helix and the orange cross representing a right-handed helix. The green diamond represents the Chaotic state. Simulations show almost equal number of left and right-handed helices (23:22). White lines show the fitting for the critical volume fraction $\phi_{vf}^* \sim \beta^{-1}$; it represents the transition boundary between the uniform and helical states.

6.7 | Shakers in 3D nematic liquid crystal

We observed a spontaneous chiral symmetry breaking in a system of 3D nematic liquid crystals with microswimmers, as a result of emerging twist-bend instability. Now, we ask, does this instability depend on the swimmer speed? The vorticity, given by $\omega \sim \sin 2\theta B_2/r^3$, has no contribution from the source dipole B_1. This suggests that the instability is independent of the swimming speed u_0 (because $u_0 = \frac{2}{3}B_1$). To test this, we used shakers, which are particles that generate a hydrodynamic flow but have zero speed ($u_0 = 0$). The slip flow at a shaker's surface is described by keeping $B_1 = 0$ and $B_2 \neq 0$ in the Equation 3.2. When the force dipole $B_2 < 0$, the flow field corresponds to that of a extensile force dipole (pusher), while for $B_2 > 0$, it corresponds to that of a contractile force dipole (puller).

In Chapter 5, we observed the bend-dominated instability in confined quasi-2D nematic liquid crystals with both swimmers (see Figures 5.3 and 5.5) and shakers (see Figure 5.7). This observation further supports the idea that the instability is independent of motility. Now, we present our results for nematic liquid crystals with shakers in a 3-dimensional setup.

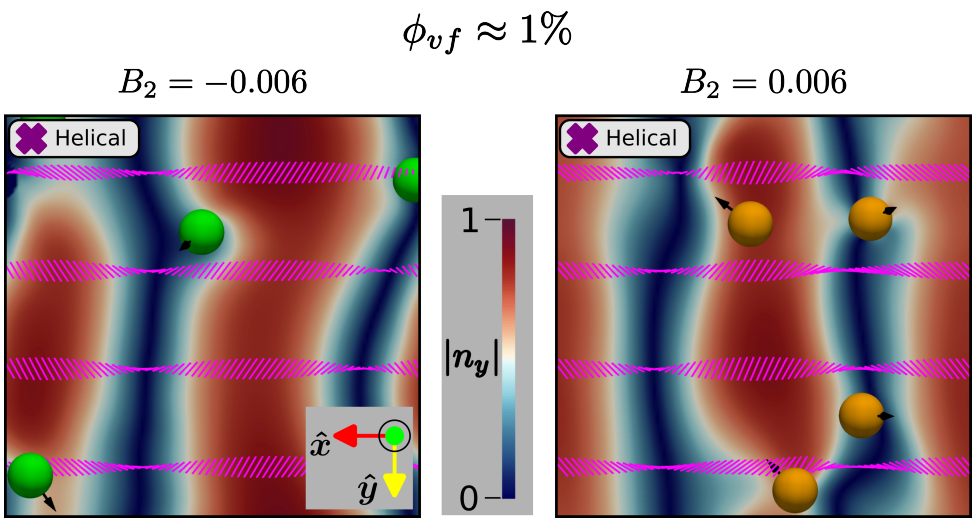

Figure 6.22: **Emergence of instability in nematic liquid crystal with shakers**: For the system consisting of spherical shakers in the nematic liquid crystal, the snapshots (at steady) show the continuous twist formation in the director field, observed at the volume fraction $\phi_{vf} \approx 1\%$. For pusher-shaker (green spheres), the strength of the force dipole B_2 is set to -0.006, while for puller-shakers (orange spheres), $B_2 = 0.006$. The color bar represents $|n_y|$, the absolute value of the director component along the y-axis.

Both pusher-shakers ($B_1 = 0, B_2 < 0$) and puller-shakers ($B_1 = 0, B_2 > 0$) were considered in our simulations, each with volume fractions of $\phi_{vf} \approx 1\%$ and 4%. We observed a chiral symmetry breaking beyond a critical global activity, where the uniform nematic order became unstable, and a continuous twist formed in the director field (see Figure 6.22). The instability was observed for both pusher-shakers ($B_2 < 0$ in Figure 6.22)

and puller-shakers ($B_2 > 0$ in Figure 6.22). A few ensembles showed a loss of continuous twist over time (only at low ϕ_{vf}). The time evolution of distortions indicated a decrease in twist distortions (refer to $B_2 = -0.0045$ in Figure 6.23). At a high volume fraction of $\phi_{vf} \approx 4\%$, we observed less fluctuations in deformations over time (see Figure 6.23).

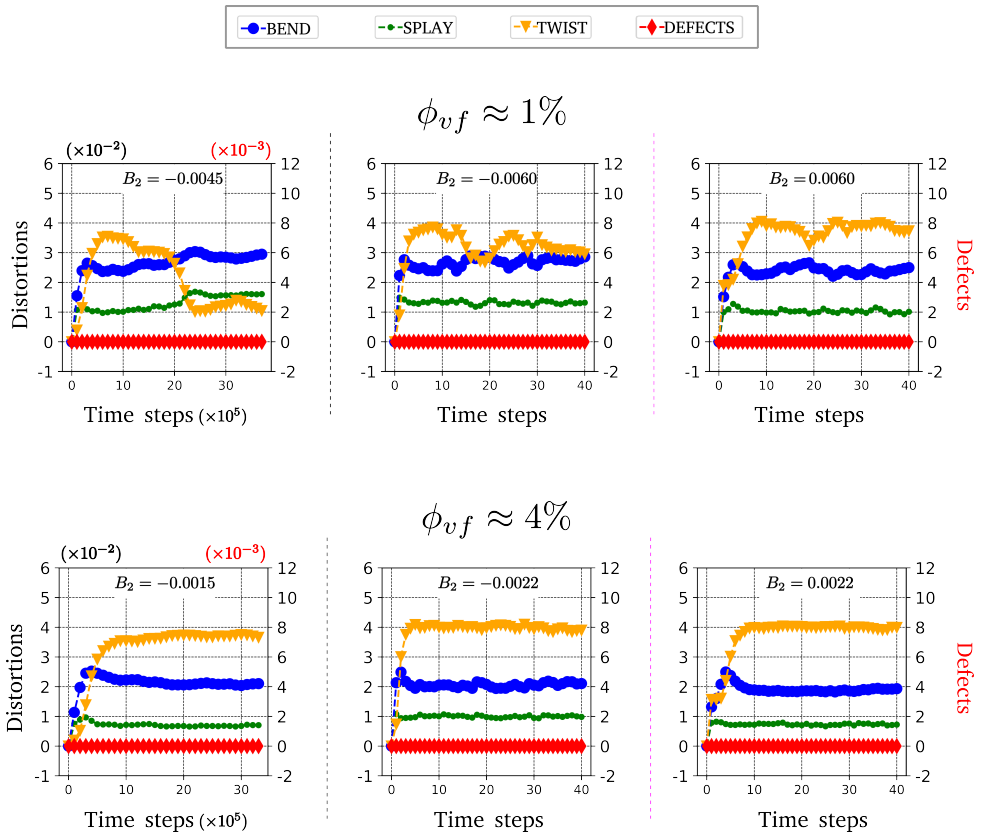

Figure 6.23: **Time evolution of deformations (for shakers)**: The figure shows the deformations over time for nematic liquid crystals with shakers ($B_1 = 0, B_2 \neq 0$). Data is presented for systems exhibiting continuous twist in the director field. A positive force dipole ($B_2 > 0$) corresponds to puller-shakers, and $B_2 < 0$ corresponds to pusher-shakers. The trend in deformation growth remains consistent for most ensembles. Initially, splay and bend deformations are observed in the system. First, splay reaches a constant value, followed by bend. Within approximately 10^6 time steps, twist reaches a constant value (steady continuous twist forms in the system). The twist and bend are the dominant deformations.

Our results suggest that the flow instability does not depend on the self-propulsion. The coupling between flow fields by the force dipoles and the liquid crystal elasticity destabilizes the uniform nematic order. The observed instability is the twist-bend mode (see Figure 6.23), which is also observed with pusher swimmers (refer to Figure 6.17). Both pusher swimmer and pusher-shaker have extensile force dipoles, and the hydrodynamic torque aligns the extensile force dipole parallel to the (local) nematic director $\hat{\mathbf{n}}$ [39]. This suggests a same flow instability can be expected for pusher-shakers and pusher swimmers. The twist-bend mode has been predicted to be the most unstable in 3D extensile active nematics [55], and our findings agree with this prediction (see Figures 6.23 and 6.17).

As with pusher-shakers, the twist-bend mode remains dominant for puller-shakers (see for $B_2 > 0$ in Figure 6.23). As discussed earlier in section 6.4, the perpendicular alignment of the contractile force dipole of puller-shaker, corresponds approximately to the parallel alignment of the extensile force dipole of pusher-shaker (refer to Figure 6.18). This suggests that both pusher-shakers and puller shakers can exhibit same instability, which agrees with our observations (see Figures 6.23).

6.8 | Discussion

In this chapter, we investigated the behavior of spherical microswimmers in 3D nematic liquid crystals. We found that the hydrodynamic coupling between the swimmer flow fields and the nematic order can lead to the spontaneous formation of a continuous twist in the director field. Distortion analysis indicated, twist-bend mode to be the most unstable, which is consistent with the linear stability analysis of 3D extensile active nematics [55]. This twist-bend instability dominated not only in systems with pushers, but also with pullers.

Our findings suggest that realizing a contractile active nematic system using spherical puller swimmers might not be possible. An alternative approach to potentially realize such system, could be introducing non-spherical pullers, such as rod-like pullers, into the nematic liquid crystal. This is because, for the rod-like swimmers, the elastic torque can exceed the hydrodynamic reorienting torque. Consequently, rod-like pullers would swim along the nematic director, and align their inward (contractile) force dipoles parallel to the nematic director. Simulations of elliptical microswimmers with surface anchoring have observed this parallel alignment for pullers [102]. Nematic liquid crystals with such elliptical puller swimmers could be seen as a contractile active nematic system.

Our simulations also demonstrated that the particle dynamics and director orientations are connected. The Helical (chiral) state, characterized by a continuous twist in the nematic director field, induced helical motion in both pusher and puller swimmers. This behavior was explained by considering the preferred swimming direction of particles. Pushers prefer swimming parallel to the nematic director, while pullers prefer perpendicular to it [39]. As the local director spatially rotates in the Helical state, the swimmers continuously adjust their direction to maintain their preferred alignment, resulting in their helical trajectories.

Using the concept of vorticity of the squirmer flow field, we approximated the activity ζ at the continuum limit as $\zeta \sim B_2\phi_{vf}$, leading to a critical volume fraction $\phi^*_{vf} \sim B_2^{-1}$. This aligns well with existing literature on active nematics [98, 40, 48] and fitted our simulation data remarkably well. Furthermore, our vorticity argument suggests that the emergence of instability is independent of the swimming speed (i.e, the source dipole). In fact, the coupling between the force dipole flow field and the nematic order drives the instability.

This was confirmed by both our quasi-2D and 3D simulations where systems with shakers (particles with zero swimming speed) exhibited the bend instability in quasi-2D and the twist-bend instability in 3D.

Simulation studies have reported the growth of twist deformations in 3D extensile active nematics [53, 55, 54, 57]. Also, recent simulations with homeotropically confined extensile active nematics have reported stable continuous twists [103]. However, our work focuses on a system with actual microswimmers generating hydrodynamic flow fields, offering a distinct approach to understand the interaction between the active particles and the nematic order.

The observed shift from bend-dominated instability in our quasi-2D simulations to twist-bend dominated in 3D aligns well with theoretical predictions for extensile active nematics [49, 55]. Our finding highlights the crucial role of dimensionality in shaping the instability and suggests that similar behavior might be observed in experiments with active bacteria/nematic suspensions. For instance, experiments with quasi-2D LLCs have already observed the bend instability [40]. Opening the third dimension in such experiments could serve as a direct verification of our findings.

Having explored the collective behavior of microswimmers in nematic liquid crystals, the next chapter investigates how individual microswimmers move within this environment. We focus on strategically manipulating swimmer dynamics using techniques like patterned nematics and further explore the potential for cargo transport using shared topological defects.

Chapter 7

Controlling microswimmer dynamics using liquid crystalline order

This chapter investigates strategies like patterned nematics to control the dynamics of microswimmers in nematic liquid crystals. Inspired by bacterial experiments, we simulated both pusher and puller type swimmers in various patterns (pure bend, pure splay, mixed bend-splay). Our simulations revealed distinct trajectories for each swimmer based on its preferential swimming direction. Furthermore, at Ericksen numbers below a specific threshold (where elastic forces dominate), both pusher and puller swimmers were observed to be trapped at different pattern centers.

After studying microswimmer behavior in patterned nematic, the second section explores the cargo transport using spherical swimmers. We propose a novel approach, utilizing topological defects (like a rope) to bind the swimmer and cargo. Interestingly, our simulations reveal that replacing a passive cargo particle with an active colloid (either pusher or puller) preserves the defect while adding the crucial element of motility. We further explore how the swimmer type dictates the cargo transport direction. Lastly, we investigate a system inspired by the Pac-Man game, where the active colloid (puller) collects passive colloids through dynamic reformation of entangled topological defects.

7.1 | Simulation setup

Concerning this chapter, the simulations were conducted in a quasi-2D box with dimensions $256 \times 256 \times 21$. To have patterned nematic director field, walls with a fixed director orientations were placed in the z-direction, with anchoring strength $W_0 = 0.1$. Spherical swimmers with a radius $R = 6$ in lattice units (LU), were initialized within the mid-plane. The surface velocity profile of the swimmer followed squirmer model (Equation 3.2), with the squirmer parameter β set to -1 for a pusher and $+1$ for a puller. The parameter B_1 was set to 0.0015, resulting in a swimming speed $u_0 = 0.001$. For simulations concerning

entangled colloids (in Section 1.3), passive and active colloids with homeotropic surface anchoring were used, with anchoring strength $W_0 = 0.1$.

The parameters used for the nematic liquid crystal were $A_0 = 0.1$, $\gamma = 3.0$, $K = 0.065$, $\Gamma = 0.3$, and rotational viscosity $\gamma_1 = \frac{2(3s/2)^2}{\Gamma} = 5/3$, where s is the scalar order parameter. These values gives the Ericksen number $\mathrm{Er} \equiv \frac{\gamma_1 u_0 R}{K} \approx 0.15$, and the Reynolds number, $\mathrm{Re} \equiv \frac{u_0 R}{\eta} \approx 0.036$.

7.2 | Microswimmer in patterned director field

As an anisotropic medium, nematic liquid crystals have proven to be effective in controlling microswimmer dynamics [37, 36, 41]. Experiments with Living Liquid Crystals (LLCs), bacterial suspensions in nematic liquid crystals, have shown promising results. In these experiments, researchers confine LLCs into flat cells with surface anchoring effects [37, 36, 41]. Typically, the anchoring at the cell surface ensures that the director follows the pattern given by $\hat{\mathbf{n}}_0 = (\cos\theta, \sin\theta, 0)$, where θ represents the angle between the radial vector and the director. When $\theta = 90°$, the director field has maximum bend deformation (see director field in black, Figure 7.1b), and the pattern is referred to as the pure bend pattern. Conversely, when $\theta = 0°$, the director field has maximum splay deformation (see Figure 7.1d), and the pattern is termed as the pure splay pattern. Motivated by experiments, we also use a pattern with $\theta = 45°$; it has equal bend and splay deformation (see Figure 7.3), and is referred to as the mixed splay-bend pattern.

In experiments with dilute suspensions of LLCs, pusher-type bacteria have been observed to swim along the (local) nematic director without affecting the patterned director field [37, 36, 41]. Within the $\theta = 90°$ pattern, bacteria exhibit apolar circular motion [37], represented by blue and red lines in Figure 7.1a. However, in the $\theta = 0°$ pattern, corresponding a pure splay pattern, the bacteria display apolar linear motion [37] (blue and red lines in Figure 7.1c), with some of them aggregating at the defect center.

In our simulations, we considered a pusher-type spherical microswimmer with random initial orientations in the pure bend and the pure splay patterns. Within both patterns, the pusher was observed to follow the local nematic director (Figures 7.1b and 7.1d). In the pure bend pattern, depending on the initial orientation, the pusher exhibited clockwise or anticlockwise circular trajectories (red and blue lines in Figure 7.1b). However, in the pure splay environment, different initial orientations resulted in the pusher moving towards or away from the pattern center (red and blue lines in Figure 7.1d).

Our findings demonstrate that an individual pusher follows the local nematic director in the patterned liquid crystal (Figure 7.1b and 7.1d). In experiments with LLCs, below the threshold for collective behavior, the pusher-like bacteria are observed to follow the local nematic director as well (Figure 7.1a and 7.1c). Thus, our simulation results align with the experiments.

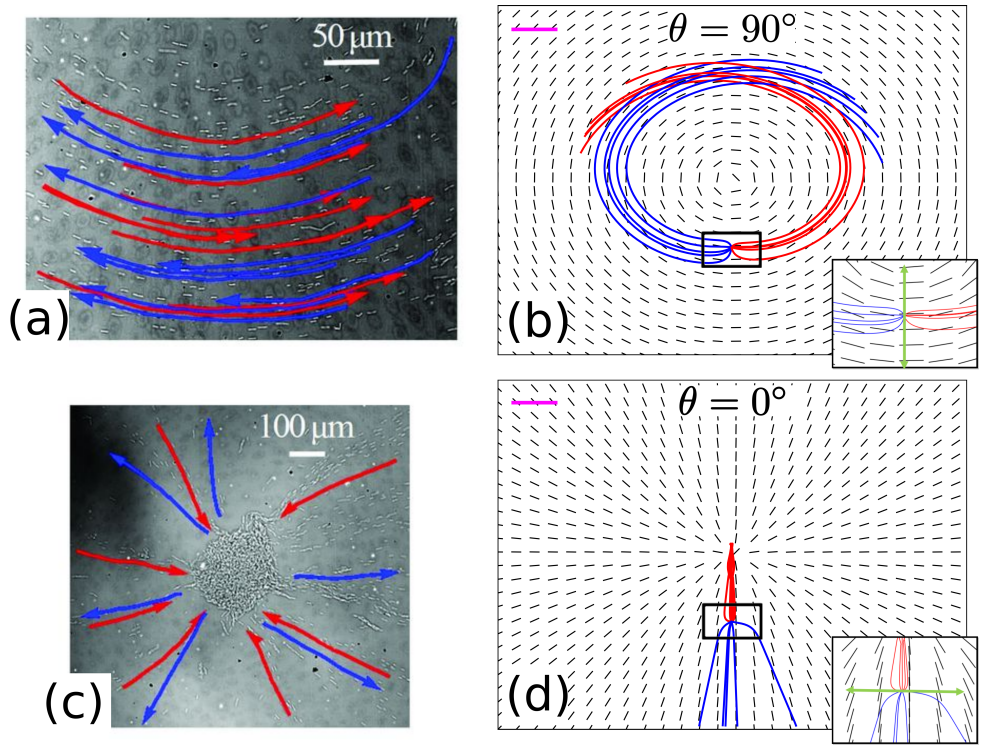

Figure 7.1: **Pusher in patterned nematic liquid crystal:** The figure compares our simulation results with existing experiments. Subfigures (a) and (c) depict trajectories observed in simulations with a pusher squirmer in patterned nematic liquid crystal.The pink scale bars correspond to $4R$, where R is the squirmer radius. Subfigures (b) and (d) show trajectories from experiments with pusher-type bacteria, *B. subtilis*, in patterned liquid crystal [37]. In (a) and (b), the director field pattern is pure bend, while in (c) and (d), it is pure splay. Note that the trajectories observed in simulations (Figures (a) and (c)) are for a single squirmer with different initial random orientations. Both experimental and simulation results suggest that an individual pusher swims parallel to the local director.

A spherical pusher and a puller generate distinct flow fields (refer to Figure 3.4), and the hydrodynamic torque acting on them within the nematic environment also differs. The torque rotates the pusher to swim parallel to the nematic director, while it orients the puller to swim perpendicular to the nematic director [39]. Consequently, one would anticipate different behaviors between a pusher and a puller in the same patterned nematic environment. In our simulations, the pusher was observed to have circular trajectory in a pure bend environment (Figure 7.1b). However, in the same patterned director field, the puller exhibited linear trajectories (see Figure 7.2a). This behavior can be understood in terms of the preferred swimming direction for a puller. Since a puller prefers to swim perpendicular to the nematic director [39], in a pure bend pattern, the perpendicular directions to a local nematic director are either towards or away from the pattern center. Thus, depending on the initial orientation, the puller can move either towards or away from the pattern center, and our results confirm this (red and blue lines in Figure 7.2a).

A similar argument can be made for a puller moving in a pure splay pattern. In this scenario, by swimming perpendicular to the local nematic director, the puller will exhibit a circular trajectory. We observed this behavior (shown in Figure 7.2b), the puller exhibited

either clockwise or anticlockwise circular trajectories (represented by blue and red lines in Figure 7.2b), depending on its initial orientation.

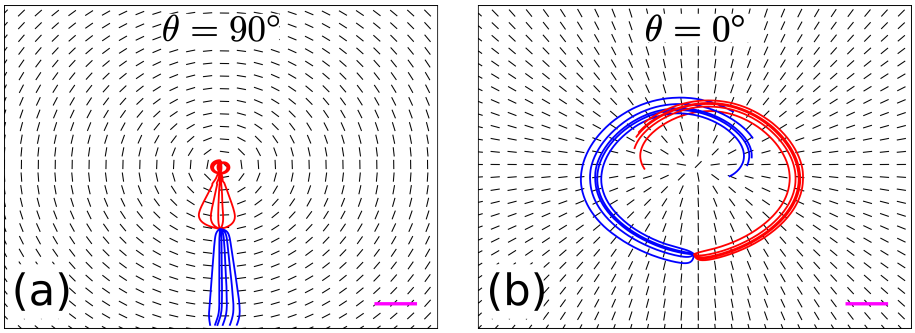

Figure 7.2: **Puller in patterned nematic liquid crystal:** The figure shows trajectories observed for a puller squirmer with random initial orientations in patterned director fields. Figure (a) displays trajectories in a pure bend environment, while Figure (b) shows trajectories in a pure splay environment. The pink scale bars correspond to $4R$, where the squirmer radius $R = 6$. Our results demonstrate that an individual puller swims perpendicular to the local director.

After examining microswimmer dynamics in pure bend and pure splay patterns, we shift our focus to a mixed splay-bend pattern. At $\theta = 45°$ in $\hat{\mathbf{n}}_0 = (\cos\theta, \sin\theta, 0)$, the patterned director field has both bend and splay deformations (see Figure 7.3). This mixed splay-bend pattern resembles an anticlockwise spiraling vortex. The interesting aspect of this pattern is that tracing paths, whether moving perpendicular or parallel to the local nematic director, leads to convergence at the vortex center.

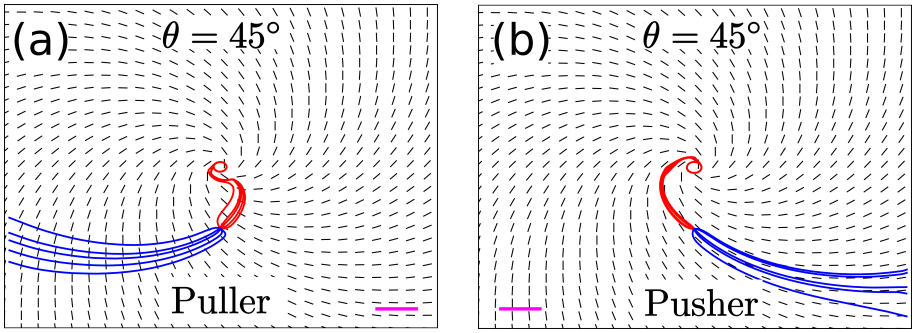

Figure 7.3: **Microswimmers in mixed bend-splay environment:** The figure shows trajectories for a squirmer with random initial orientations in patterned director fields, specifically in a mixed bend-splay environment. In subfigure (a), our simulations show that an individual puller swims perpendicular to the local director and ends up at the spiral vortex center. In subfigure (b), pushers are observed to follow the local director but also converge at the spiral vortex center. The pink scale bar corresponds to $4R$.

In our simulations, similar trajectories were observed for both pusher and puller in this mixed splay-bend environment (Figure 7.3). Puller moved perpendicular to the local director, converging at the vortex center, while pushers moved parallel to the local director, also converging at the vortex center (red lines in Figure 7.3a and 7.3b). However, not all initial orientations resulted in trajectories converging at the center; roughly speaking, pusher and puller initially pointing towards the vortex center ended up at the center.

Interestingly, experiments have seen a shift in bacterial (pusher) behavior: at low concentrations, rod-like bacteria align with the local director and move towards the vortex center [41]. However, as the bacterial density increases, their movement transitions to unipolar circular swimming [41, 37].

Trapping microswimmer in patterned nematic

In our simulations with patterned director fields, spherical swimmers were observed to be stopped or trapped at the defect core (see red trajectories in Figures 7.1d, 7.2a, and 7.3). We named this phenomenon trapping and it occurs when the microswimmer is arrested at the core to minimize the elastic term (Equation 4.2) in the total liquid crystal free energy [104]. To investigate the impact of elastic forces on trapping, we simulated both a pusher and a puller in patterned liquid crystal with different elastic constants, specifically, $K = 0.065$ (high) and $K = 0.01$ (low), while keeping other parameters constant.

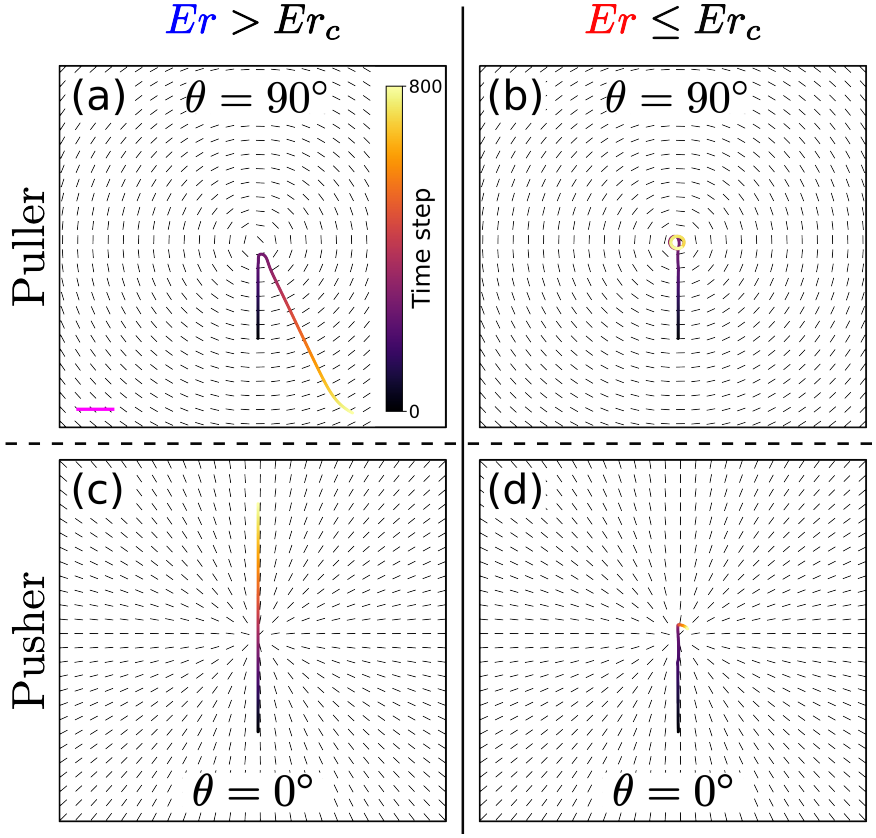

Figure 7.4: **Trapping microswimmers using patterned liquid crystal:** The figure shows trajectories for a spherical squirmer in a patterned nematic director field. In the early time steps, a puller (pusher) is observed to move perpendicular (parallel) to the local director. Above the critical Ericksen number Er_c, the puller is deflected at the defect core and continues moving perpendicular to the director, while the pusher moves parallel to the director. However, below a critical number Er_c, the puller (pusher) is observed to be trapped at the center of a pure splay (bend) defect. The trajectories are color-mapped based on the time color bar, and the pink scale bar corresponds to $4R$. Subfigures (a) and (c) correspond to $K = 0.01$, $Er \approx 1$, while subfigures (b) and (d) correspond to $K = 0.065$, $Er \approx 0.15$.

Simulation results, presented in Figure 7.4, suggest a critical Ericksen number, Er_c, below which elastic forces dominate over viscous forces. In this limit, the director field is barely affected by the flow fields generated by the squirmer. Thus, upon reaching the defect core, the squirmer cannot affect the the director field and to minimize the elastic free energy, it covers up the defect. This is observed when the elastic constant K is high ($K = 0.065$), corresponding to a Ericksen number $Er \approx 0.15$. Specifically, a puller was observed to be trapped at the defect core of a pure bend pattern (Figure 7.4b), and the pusher was also observed to be trapped at the core of a pure splay pattern (Figure 7.4d).

7.3 | Cargo transport using entangled defect

When a spherical colloid with surface anchoring, such as homeotropic or planar anchoring, is dispersed in a nematic liquid crystal, topological defects form around the colloid's surface [75, 76, 105]. If the colloid has homeotropic surface anchoring, a topological defect known as the "Saturn ring" forms around the particle (see Figure 7.5a). This occurs because the homeotropic anchoring at the colloid's spherical surface forces the nematic director to be perpendicular (black solid lines in Figure 7.5b). However, there is a region on the surface where the director orientation changes abruptly (black ring in Figure 7.5b), resulting in a ring-like defect encircling the colloid (see Figure 7.5a).

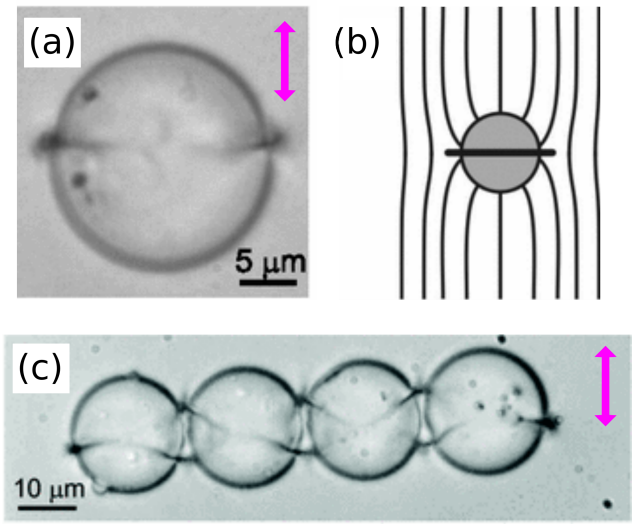

Figure 7.5: **Topological defects around colloids:** Experimentally observed topological defects around colloids with homeotropic surface anchoring, dispersed in a nematic liquid crystal. Subfigure (a) depicts a Saturn ring observed around glass spheres with a surface treatment inducing homeotropic alignment for liquid crystal molecules. Subfigure (b) schematically illustrates the director field around the particle surface, leading to Saturn ring formation. Subfigure (c) showcases the entangled defect encircling all spheres. The pink double-sided arrow indicates the director field alignment. Figures are taken from [75, 76].

When multiple spherical colloids are dispersed in a thin nematic liquid crystal, experiments have revealed an interesting phenomenon [75, 76]. At large separations, each particle

is surrounded by a Saturn ring. However, at smaller separations, these Saturn rings merge to form entangled topological defects [75, 76], including the "Entangled Hyperbolic defect" (see Figure 7.6c). In this structure, the defect loops around two colloids, and an additional loop is formed in the middle. Studies have found that the elastic contribution from the entangled structure is lower than that of isolated Saturn rings [106]. Moreover, the energy required to break the Entangled Hyperbolic defect has been measured to be the order of $1000k_BT$ [75]. Thus, the entangled defect reduces the overall elastic energy contribution while providing a strong binding force. Ultimately, colloidal entanglement via topological defects can contribute to the development of complex colloid-nematic composite materials.

To simulate the formation of an entangled topological defect, we placed two spherical colloids with homeotropic surface anchoring in proximity within a quasi-2D nematic liquid crystal. At the walls of the simulation box homeotropic anchoring was applied. Our simulation revealed a stable topological defect encircling both colloids (Figure 7.6(a)-(b)), similar to the Entangled Hyperbolic defect observed in the experiments (Figure 7.6c) [75].

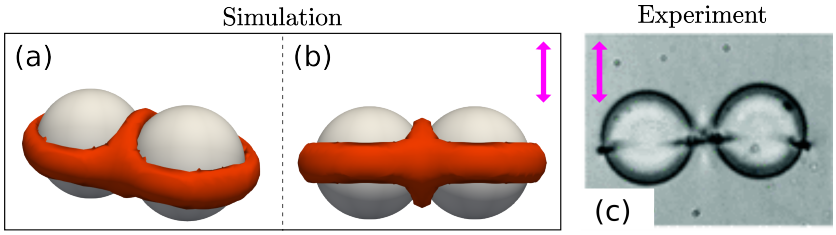

Figure 7.6: **Entangled colloidal dimers:** The figure compares the entangled structures observed in our simulations with those seen in experiments. Subfigures (a) and (b) show the entangled structure observed in our simulations, featuring two colloids with homeotropic anchoring at the surface within a nematic liquid crystal. An entangled topological defect is observed, encircling both the colloids. The simulation conducted using an elastic constant $K = 0.065$. Subfigure (c) showcases the topological defect, the Entangled Hyperbolic defect, observed in the experiment by Ravnik et al. [75]. The director orientation is indicated by the pink double-sided arrow. The defect loop (depicted in red) is visualized using an isosurface of the scalar order parameter $s = 0.22$. Subfigure (c) is adapted from [75].

Now, the question is: Can we transport the cargo of entangled passive colloids using an active colloid, where the binding force (to hold the cargo) is provided by the entangled topological defect? We propose adding a spherical squirmer with homeotropic surface anchoring to the entangled structure. Our assumption is that within the low Ericksen number regime, where elastic forces dominate over viscous forces, the flow field generated by the active colloid will not significantly affect the surrounding director field. Consequently, the entangled topological defect will remain unaffected, and the whole entangled structure will be moved by the active colloid.

In our simulations, we explored arrangements with three spherical colloids with homeotropic surface anchoring within a nematic liquid crystal. First, we used two passive colloids and one active colloid of puller type, as shown in Figure 7.7. In the early stages,

a stable entangled topological defect was observed, which encircled all the colloids, including the puller. As the active puller started moving, the entire entangled structure was observed to move with it in unison (see Figure 7.7), resembling a "Squirmer Train" with passive colloids as cargo and the puller acting as the engine. Since a puller tends to move perpendicular to the nematic director [39], the cargo train was also observed to move in the same direction.

The existence of entangled structures with two or more colloids has already been observed in experiments (see Figure 7.5c and 7.6c) [75]. However, our simulation findings (Figure 7.7) suggest that an active spherical colloid can replace one of the passive colloids without disrupting the entangled topological defect. These insights contribute to the exploration of cargo transport systems within nematic environments.

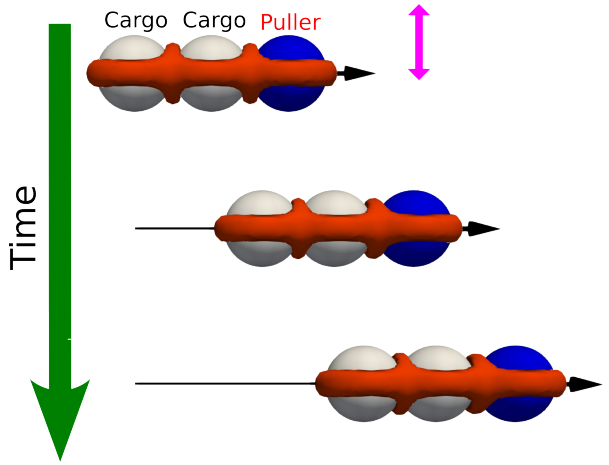

Figure 7.7: **Squirmer Train:** This figure shows the cargo transport observed in our simulations. The entangled structure, Squirmer Train, consists of three spherical colloids: two passive colloids and one puller at front. The presented snapshots are taken at successive time steps. The puller and two passive colloids have homeotropic anchoring on their surfaces. The simulation was conducted using an elastic constant $K = 0.065$. Defect loops (depicted in red) form an entangled structure holding colloids together. The black solid lines represent the observed trajectory of the colloids, with the black arrow indicating the puller's orientation. The defects are visualized using an isosurface with scalar order parameter $s = 0.22$. The pink double-sided arrow gives the nematic director orientation.

Another observation from Figures 7.6 and 7.7 is the plane in which the entangled structure forms, perpendicular to the nematic director. The hydrodynamic torque on a puller moving in this plane is zero [39]. Without a torque to keep the puller's orientation fixed, the Squirmer Train will equally prefer any direction perpendicular to the nematic director. This characteristic makes the moving direction of the Squirmer Train susceptible to any fluctuation, which is not an ideal for guided cargo transport.

To achieve truly guided cargo transport, we propose the use of a pusher-type squirmer as the active colloid. The hydrodynamic torque on a pusher keeps its swimming direction parallel to the nematic director [39], ensuring that the moving direction of the entangled structure remains fixed (along the nematic director). If the puller in the front of the

Squirmer Train is replaced by a pusher, the pusher will initially orient itself along the nematic director and attempt to pull the entire structure. However, due to the asymmetry in the entangled structure, this configuration may not be optimal for guided transport.

We simulated a symmetric arrangement, termed as the "Squirmer Jet", where the pusher was positioned at the center of the entangled structure (see Figure 7.8). Our simulations with this symmetric arrangement, showed directed movement of the entangled structure (Figure 7.8). As the pusher swims along the nematic director, the entire structure was observed to move in the same direction. Although a stretching of the entangled defect was observed, it remained unbroken throughout the simulation duration.

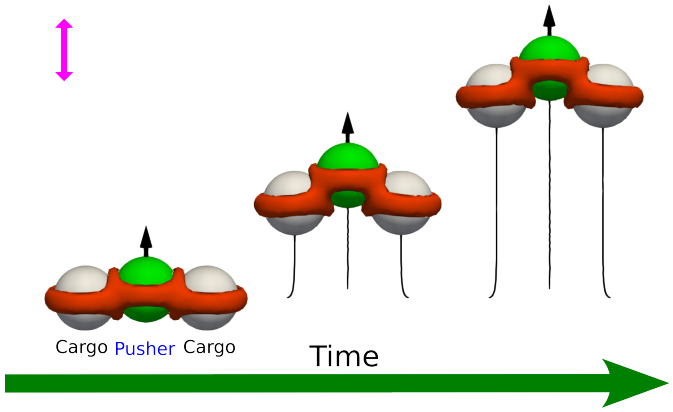

Figure 7.8: **Squirmer Jet:** Our simulation findings show the transport of an entangled structure consisting of two passive colloids and a pusher. This entangled arrangement is named as Squirmer Jet. The snapshots shown are taken at successive time steps. The observed trajectories of the pusher and passive colloids are depicted in black solid lines. The orientation vector of the pusher is represented by a black arrow. The pusher and the two passive colloids have homeotropic anchoring on their surfaces. The simulation was conducted using an elastic constant $K = 0.065$. The nematic director orientation is denoted by the pink double-sided arrow.

Several versions of the Squirmer Jet were considered in our simulations. These configuration were named CFG-1, CFG-2, and CFG-3 (Figure 7.9). While the earlier-discussed Squirmer Jet, referred to as CFG-1, has one pusher in the entangled structure, both CFG-2 and CFG-3 have two pushers positioned at the edges of the structure (see Figure 7.9). The pusher orientations in CFG-2 and CFG-3 were initialized differently. In CFG-2, the pusher orientations were parallel to each other and aligned with the nematic director. However, in CFG-3, the pusher orientations were set to point away from each other and at 45° to the nematic director.

In simulations, CFG-2 was observed to be the fastest, while CFG-1 was the slowest (Figure 7.10). Our findings can be understood by examining the forces acting on the particles. The ratio of the total drag forces in CFG-1 and CFG-2 is ≈ 2 (because of 2 passive colloids in CFG-1). This suggests that the ratio of the velocities should be around this value. From Figure 7.10, the ratio of average velocities for CFG-1 and CFG-2 appears

to be ≈ 2.4, which is not significantly different from our estimate. The discrepancy may arise from the coupling of pusher flow fields in CFG-2.

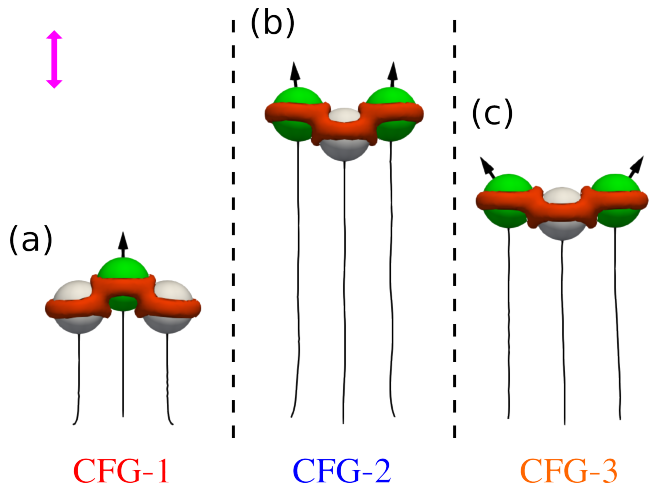

Figure 7.9: **Trajectories in different Squirmer Jet configurations:** The figure compares the trajectories observed for various Squirmer jet configurations, CFG-1, CFG-2, and CFG-3, within 50 simulation time steps. Each configuration consists of a entangled structure with three colloids. In CFG-1, one colloid is a pusher and is at the middle of the structure. In CFG-2, two of the colloids are pushers and are at two sides of the structure. CFG-2 have the longest trajectories within the same time; hence, this configuration is the fastest.

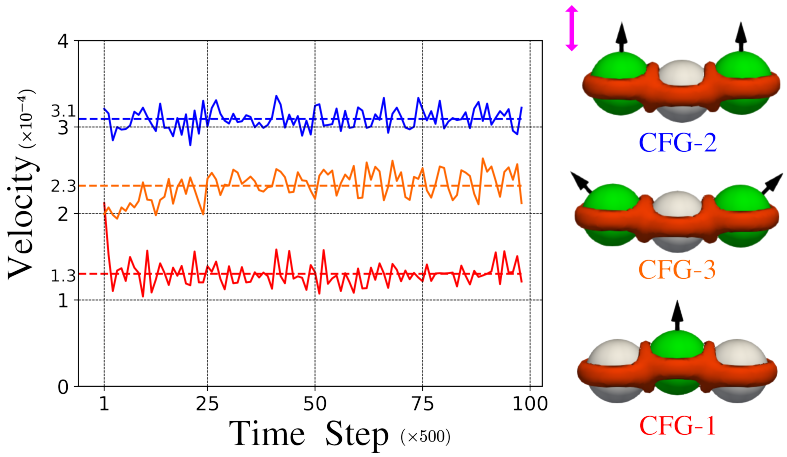

Figure 7.10: **Comparing velocities of Squirmer Jet configurations:** The plot compares the velocity of the entangled structure as a function of time for CFG-1, CFG-2, and CFG-3 configurations. The dashed lines represent the average velocity. The colors red, blue, and green correspond to CFG-1, CFG-2, and CFG-3, respectively. The average velocity is maximum for CFG-2, while it is minimum for CFG-1. Velocity and time are in simulation units.

Both CFG-2 and CFG-3 have the same number of passive colloids, meaning the amount of drag is the same in both cases. However, the propulsion forces in CFG-3 are at an angle of $\approx 45°$ to the nematic director, while they are along the nematic director in CFG-2. Thus, simple force balance suggests the ratio of velocities of CFG-3 and CFG-2 to be ≈ 1.4, which is remarkably close to the observed ratio of 1.3 (see Figure 7.10).

We must address that the observed behavior of configuration CFG-3 deviates from our expectations. Considering that the hydrodynamic torque aligns the pusher's orientation along the nematic director, we anticipated that the initial orientations of pushers in CFG-3, set at 45°, would rotate to align with the nematic director. And the dynamics of CFG-3 and CFG-2 will be similar. However, in CFG-3, the pusher orientations were not observed to align with the nematic director. We are unable to provide an explanation for the dynamics of CFG-3. But, it may be a consequence of boundary effects from the passive colloid present between two pushers.

For all the discussed entangled systems, including the Squirmer Train and various configurations of the Squirmer Jet, we carefully initialized the system to form a linear entangled structure. The colloids were positioned in proximity and in a straight line, with the orientations of the active colloids properly initialized to enable guided motion. However, achieving such precise control in experiments can be challenging. To bridge the gap between simulations and real-world scenarios, we simulated a system where a bunch of randomly distributed colloids were present in a quasi-2D nematic cell, along with a randomly initialized active colloid (see Figure 7.11). This setup can be realized in experiments using glass spheres as passive colloids, like in the work done by Ravnik et al. [75]. For the active colloid, a Janus sphere is a promising candidate. In experiments, Janus colloids powered by an AC electric field have demonstrated guided motion in nematic liquid crystal [107].

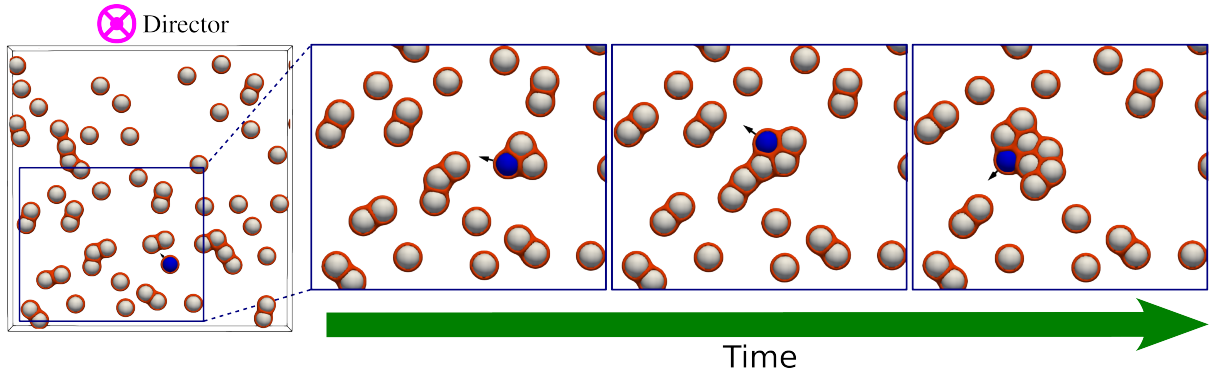

Figure 7.11: **Pacman game:** Our simulation of the Pacman game concept. In this, the quasi-2D box is initialized with a population of passive colloids and a puller, all with homeotropic anchoring at their surfaces. The nematic director is set along z-axis, denoted by a pink cross. The leftmost figure shows the system in early stages, where colloids in proximity form entangled structures of various lengths and shapes. The blue rectangle highlights the zoomed area within the simulation box and the 2D snapshots are taken at successive time steps. The puller moves perpendicular to the nematic director. When in proximity to an entangled structure, the puller's Saturn ring merges with it, forming a larger entangled structure. The passive colloids get entangled with the puller, expanding the size of the entangled structure. During the simulation duration, the puller is able to collect seven passive colloids.

In our simulations, we randomly initialized approximately 55 passive colloids and a puller-type squirmer within a quasi-2D nematic environment. In the early stages of the

simulation, colloids in proximity formed entangled structures of various lengths and shapes (see Figure 7.11). As expected, the puller was observed to move perpendicular to the nematic director. Upon nearing another colloid, its Saturn ring merged with another topological defect, forming a larger entangled topological defect. This process continued, and other passive colloids became entangled with this moving structure. Over time, the puller successfully collected multiple colloids. However, the velocity of the massive entangled structure decreased continuously due to the increasing drag force with each collection of passive colloids.

Our simulation results, presented in Figure 7.11, vaguely reminded us of the popular game, Pac-Man, where the objective was to collect dots. Hence, we named our system Pacman.

7.4 | Discussion

In this chapter, we first explored the strategies for guiding microswimmers using patterned nematic liquid crystal. We investigated the behavior of spherical swimmers of both pusher and puller types within various patterned director fields, such as pure splay, pure bend, and mixed splay-bend.

Our findings demonstrate that a pusher moves parallel to the local nematic director, resulting in circular trajectory in a pure bend, and linear trajectory in a pure splay pattern. These observations align with the experiments with bacteria (at low concentrations) in the patterned nematic [37]. However, we observed the opposite behavior for pullers. In a pure bend pattern, the puller exhibited linear trajectory, while in a pure splay, it exhibited circular trajectory. Finally, both pusher and puller showed similar convergence to the pattern center in a spiral vortex pattern.

We observed microswimmers to be trapped in a patterned nematic. At low Ericksen number, the microswimmer does not significantly affect the local director field, and can get trapped at the pattern center. By covering up the defect at the pattern center, the system minimizes the elastic term in the total Landau free energy. In simulations, at low Ericksen number, the pusher was trapped in the pure splay pattern, and the puller was trapped at the pure bend.

Furthermore, we explored the cargo transport of passive colloids using a spherical swimmer. The cargo was attached to the swimmer via the entangled topological defect. Our simulations suggest that the topological defect can be shared between active colloids and passive colloids. And, within the low Ericksen number regime, the entangled topological defect is not affected by the flow field of the active colloid. Specifically, we simulated the Squirmer Train with a puller attached to the cargo (passive colloids) via topological defect. Our simulations demonstrated directed cargo transport in a direction perpendicular to the nematic director. However, a puller prefers any direction perpendicular to the nematic

director; thus, maintaining a fixed direction of movement can be challenging. To achieve truly guided motion, we propose using a pusher instead, because, the hydrodynamic torque on a pusher, ensures the swimming direction to be along the nematic director [39].

We named the entangled system of pusher swimmers and cargo of passive colloids, the Squirmer Jet. Three different versions of squirmer jet were simulated, CFG-1, CFG-2, and CFG-3. In CFG-1, a single pusher was positioned in the middle of the structure (with two passive colloids); CFG-2 and CFG-3 had two pushers at the sides (with one passive colloid in middle). All three configurations moved along the nematic director, with CFG-2 reaching the highest speed, followed by CFG-2 and then CFG-1.

Lastly, we simulated a system inspired by a popular game, Pac-Man. In this setup, passive colloids and an active colloid, all with homeotropic surface anchoring, were introduced into a quasi-2D nematic environment. Since the shared topological defects cost less elastic energy, entangled structures of various shapes and sizes emerged in the early stages of the simulation. As the puller approached colloids in proximity, the Saturn ring of the puller merged with the topological defect, resulting in a larger entangled topological defect. This process repeated throughout the simulation duration, enabling the puller to collect multiple colloids. However, with each collection, the drag force increased, leading to a significant slowdown of the puller.

The insights from our findings can contribute to the design of efficient cargo transport systems. The entangled structure strongly bound via topological defects, has already been observed in experiments. Our findings suggest that introducing an active colloid can provide mobility to the structure without affecting the topological defect. The choice of the active colloid as either a pusher or puller type provides control over guiding the transport either along or perpendicular to the nematic director. Additionally, introducing patterns in the nematic director field can add another layer of control for directing the entangled structures.

Chapter 8

Conclusion

We investigated the collective behavior of microswimmers in nematic liquid crystals, using hydrodynamic simulations. We observe that the flow fields generated by swimmers destabilize the orientational order present in the nematic liquid crystal. Under quasi-2D confinement, a wave-like pattern emerges in system with pusher (extensile) swimmers. Distortion analysis reveals the bend mode as the most unstable, aligning with predictions for 2D extensile active nematics [49]. Also, the bend-dominated instability has been seen in experiments with quasi-2D living liquid crystals (bacteria/nematic suspensions) [40].

When the swimmers are introduced in full 3-dimensional nematic liquid crystals, we observe spontaneous chiral symmetry breaking in the system; the uniform nematic state becomes unstable and transitions into a cholesteric-like (chiral) state, characterized by a continuous twist. This occurs for pushers (extensile) and pullers (contractile). Since there is no inherent chirality in the system, we observe equal number of ensembles with right and left-handed twists. Distortion analysis indicates the twist-bend mode to be the most unstable, consistent with theoretical predictions for 3D extensile active nematics [55]. Our findings suggest that opening the 3rd dimension in experiments of quasi-2D living liquid crystals [40] could lead to the emergence of a chiral state.

The continuous twist also impacts the swimmer dynamics. Because of their preferential alignment with the nematic director (pushers parallel, pullers perpendicular) [39], both swimmer exhibit helical trajectories in the chiral state. We also examined the role of swimming speed by introducing shakers in nematic liquid crystals. Shakers generate hydrodynamic flow but have zero swimming speed. Our observations for shakers, in both quasi-2D and 3D systems suggest that the instability arises from the coupling between the force dipole flow field and the nematic order, and is independent of the swimming speed (source dipole).

Finally, we explore strategies like patterned nematics for guiding microswimmers. Inspired by bacterial experiments, we simulated both pusher and puller type swimmers in various patterns (pure bend, pure splay, mixed bend-splay). Our simulations revealed distinct trajectories for each swimmer based on its preferred swimming direction. We also

observe trapping of microswimmer in certain patterns. Furthermore, we explore the cargo transport of colloids. Our simulations demonstrate that a cargo of passive colloids can be attached with a spherical swimmer using a topological defect (like a rope). Based on swimmer type, we see cargo transport along and perpendicular to the nematic director. To experimentally observe cargo transport, we suggest using active Janus spheres [107] and entangled glass spheres [75]. The Janus colloid could then be attached to the cargo of glass spheres, via a topological defect, which would propel the cargo chains in the desired direction.

Bibliography

[1] Jaideep Katuri, Xing Ma, Morgan M. Stanton, and Samuel Sanchez. Designing Micro- and Nanoswimmers for Specific Applications. *Acc. Chem. Res.*, 50(1):2–11, January 2017.

[2] Clemens Bechinger, Roberto Di Leonardo, Hartmut Löwen, Charles Reichhardt, Giorgio Volpe, and Giovanni Volpe. Active particles in complex and crowded environments. *Rev. Mod. Phys.*, 88(4):045006, November 2016.

[3] Julius Adler. Chemotaxis in Bacteria. *Science*, 153(3737):708–716, August 1966.

[4] Bagmi Pattanaik, Rhena Schumann, and Ulf Karsten. Effects of Ultraviolet Radiation on Cyanobacteria and their Protective Mechanisms. In *Algae and Cyanobacteria in Extreme Environments*, pages 29–45. Springer, Dordrecht, The Netherlands, 2007.

[5] Susan S. Suarez. Control of hyperactivation in sperm. *Hum. Reprod. Update*, 14(6):647–657, November 2008.

[6] Alan C. H. Tsang, Ebru Demir, Yang Ding, and On Shun Pak. Roads to Smart Artificial Microswimmers. *Adv. Intell. Syst.*, 2(8):1900137, August 2020.

[7] Luisa Sonntag, Juliane Simmchen, and Veronika Magdanz. Nano-and Micromotors Designed for Cancer Therapy. *Molecules*, 24(18):3410, September 2019.

[8] Yue Dong, Lu Wang, Veronica Iacovacci, Xiaopu Wang, Li Zhang, and Bradley J. Nelson. Magnetic helical micro-/nanomachines: Recent progress and perspective. *Matter*, 5(1):77–109, January 2022.

[9] Benno Liebchen and Hartmut Lowen. Synthetic Chemotaxis and Collective Behavior in Active Matter. *Acc. Chem. Res.*, 51(12):2982–2990, December 2018.

[10] Rémi Dreyfus, Jean Baudry, Marcus L. Roper, Marc Fermigier, Howard A. Stone, and Jérôme Bibette. Microscopic artificial swimmers. *Nature*, 437:862–865, October 2005.

[11] Daiki Nishiguchi and Masaki Sano. Mesoscopic turbulence and local order in Janus particles self-propelling under an ac electric field. *Phys. Rev. E*, 92(5):052309, November 2015.

[12] Sambeeta Das, Astha Garg, Andrew I. Campbell, Jonathan Howse, Ayusman Sen, Darrell Velegol, Ramin Golestanian, and Stephen J. Ebbens. Boundaries can steer active Janus spheres. *Nat. Commun.*, 6(8999):1–10, December 2015.

[13] Allison P. Berke, Linda Turner, Howard C. Berg, and Eric Lauga. Hydrodynamic Attraction of Swimming Microorganisms by Surfaces. *Phys. Rev. Lett.*, 101(3):038102, July 2008.

[14] Eric Lauga and Thomas R. Powers. The hydrodynamics of swimming microorganisms. *Rep. Prog. Phys.*, 72(9):096601, August 2009.

[15] J. Elgeti, R. G. Winkler, and G. Gompper. Physics of microswimmers-single particle motion and collective behavior: a review. *Rep. Prog. Phys.*, 78(5):056601, April 2015.

[16] E. M. Purcell. Life at low Reynolds number. *Am. J. Phys.*, 45(1):3–11, January 1977.

[17] Knut Drescher, Jörn Dunkel, Luis H. Cisneros, Sujoy Ganguly, and Raymond E. Goldstein. Fluid dynamics and noise in bacterial cell–cell and cell–surface scattering. *Proc. Natl. Acad. Sci. U.S.A.*, 108(27):10940–10945, July 2011.

[18] Willow R. DiLuzio, Linda Turner, Michael Mayer, Piotr Garstecki, Douglas B. Weibel, Howard C. Berg, and George M. Whitesides. Escherichia coli swim on the right-hand side. *Nature*, 435:1271–1274, June 2005.

[19] Matthew F. Copeland and Douglas B. Weibel. Bacterial Swarming: A Model System for Studying Dynamic Self-assembly. *Soft Matter*, 5(6):1174–1187, 2009.

[20] Nicholas C. Darnton, Linda Turner, Svetlana Rojevsky, and Howard C. Berg. Dynamics of Bacterial Swarming. *Biophys. J.*, 98(10):2082, May 2010.

[21] Avraham Be'er and Gil Ariel. A statistical physics view of swarming bacteria. *Mov. Ecol.*, 7(1):1–17, December 2019.

[22] Iago Grobas, Marco Polin, and Munehiro Asally. Swarming bacteria undergo localized dynamic phase transition to form stress-induced biofilms. *eLife*, March 2021.

[23] Xiaoling Wang, Raphael Blumenfeld, Xi-Qiao Feng, and David A. Weitz. 'Phase transitions' in bacteria – From structural transitions in free living bacteria to phenotypic transitions in bacteria within biofilms. *Phys. Life Rev.*, 43:98–138, December 2022.

[24] Lene K. Vestby, Torstein Grønseth, Roger Simm, and Live L. Nesse. Bacterial Biofilm and its Role in the Pathogenesis of Disease. *Antibiotics*, 9(2), February 2020.

[25] Ali Houry, Michel Gohar, Julien Deschamps, Ekaterina Tischenko, Stéphane Aymerich, Alexandra Gruss, and Romain Briandet. Bacterial swimmers that infiltrate and take over the biofilm matrix. *Proc. Natl. Acad. Sci. U.S.A.*, 109(32):13088–13093, August 2012.

[26] Enkeleida Lushi, Hugo Wioland, and Raymond E. Goldstein. Fluid flows created by swimming bacteria drive self-organization in confined suspensions. *Proc. Natl. Acad. Sci. U.S.A.*, 111(27):9733–9738, July 2014.

[27] Hugo Wioland, Francis G. Woodhouse, Jörn Dunkel, John O. Kessler, and Raymond E. Goldstein. Confinement Stabilizes a Bacterial Suspension into a Spiral Vortex. *Phys. Rev. Lett.*, 110(26):268102, June 2013.

[28] Donald L. Koch and Ganesh Subramanian. Collective Hydrodynamics of Swimming Microorganisms: Living Fluids. *Annu. Rev. Fluid Mech.*, 43(1):637–659, January 2011.

[29] Christopher Dombrowski, Luis Cisneros, Sunita Chatkaew, Raymond E. Goldstein, and John O. Kessler. Self-Concentration and Large-Scale Coherence in Bacterial Dynamics. *Phys. Rev. Lett.*, 93(9):098103, August 2004.

[30] J. C. Loudet, P. Hanusse, and P. Poulin. Stokes Drag on a Sphere in a Nematic Liquid Crystal. *Science*, 306(5701):1525, November 2004.

[31] Helen F. Gleeson, Tiffany A. Wood, and Mark Dickinson. Laser manipulation in liquid crystals: an approach to microfluidics and micromachines. *Philos. Trans. Royal Soc. A*, 364(1847):2789–2805, August 2006.

[32] T. Turiv, I. Lazo, A. Brodin, B. I. Lev, V. Reiffenrath, V. G. Nazarenko, and O. D. Lavrentovich. Effect of Collective Molecular Reorientations on Brownian Motion of Colloids in Nematic Liquid Crystal. *Science*, 342(6164):1351–1354, December 2013.

[33] Anil Kumar, Tigran Galstian, Sudip K. Pattanayek, and Simon Rainville. The Motility of Bacteria in an Anisotropic Liquid Environment. *Mol. Cryst. Liq. Cryst.*, May 2013.

[34] Peter C. Mushenheim, Rishi R. Trivedi, Hannah H. Tuson, Douglas B. Weibel, and Nicholas L. Abbott. Dynamic self-assembly of motile bacteria in liquid crystals. *Soft Matter*, 10(1):88–95, 2014.

[35] Peter C. Mushenheim, Rishi R. Trivedi, Susmit Singha Roy, Michael S. Arnold, Douglas B. Weibel, and Nicholas L. Abbott. Effects of confinement, surface-induced orientations and strain on dynamical behaviors of bacteria in thin liquid crystalline films. *Soft Matter*, 11(34):6821–6831, August 2015.

[36] Runa Koizumi, Taras Turiv, Mikhail M. Genkin, Robert J. Lastowski, Hao Yu, Irakli Chaganava, Qi-Huo Wei, Igor S. Aranson, and Oleg D. Lavrentovich. Control of microswimmers by spiral nematic vortices: Transition from individual to collective motion and contraction, expansion, and stable circulation of bacterial swirls. *Phys. Rev. Res.*, 2(3):033060, July 2020.

[37] Chenhui Peng, Taras Turiv, Yubing Guo, Qi-Huo Wei, and Oleg D. Lavrentovich. Command of active matter by topological defects and patterns. *Science*, 354(6314):882–885, November 2016.

[38] Martyna Goral, Eric Clement, Thierry Darnige, Teresa Lopez-Leon, and Anke Lindner. Frustrated 'run and tumble' of swimming Escherichia coli bacteria in nematic liquid crystals. *Interface Focus*, 12(6):20220039, October 2022.

[39] J. S. Lintuvuori, A. Wurger, and K. Stratford. Hydrodynamics Defines the Stable Swimming Direction of Spherical Squirmers in a Nematic Liquid Crystal. *Phys. Rev. Lett.*, 119(6):068001, August 2017.

[40] Shuang Zhou, Andrey Sokolov, Oleg D. Lavrentovich, and Igor S. Aranson. Living liquid crystals. *Proc. Natl. Acad. Sci. U.S.A.*, 111(4):1265–1270, January 2014.

[41] Taras Turiv, Runa Koizumi, Kristian Thijssen, Mikhail M. Genkin, Hao Yu, Chenhui Peng, Qi-Huo Wei, Julia M. Yeomans, Igor S. Aranson, Amin Doostmohammadi, and Oleg D. Lavrentovich. Polar jets of swimming bacteria condensed by a patterned liquid crystal. *Nat. Phys.*, 16:481–487, April 2020.

[42] Shuang Zhou, Oleh Tovkach, Dmitry Golovaty, Andrey Sokolov, Igor S. Aranson, and Oleg D. Lavrentovich. Dynamic states of swimming bacteria in a nematic liquid crystal cell with homeotropic alignment. *New J. Phys.*, 19(5):055006, May 2017.

[43] Amin Doostmohammadi, Jordi Ignés-Mullol, Julia M. Yeomans, and Francesc Sagués. Active nematics. *Nat. Commun.*, 9(3246):1–13, August 2018.

[44] Tim Sanchez, Daniel T. N. Chen, Stephen J. DeCamp, Michael Heymann, and Zvonimir Dogic. Spontaneous motion in hierarchically assembled active matter. *Nature*, 491:431–434, November 2012.

[45] Stephen J. DeCamp, Gabriel S. Redner, Aparna Baskaran, Michael F. Hagan, and Zvonimir Dogic. Orientational order of motile defects in active nematics. *Nat. Mater.*, 14:1110–1115, November 2015.

[46] Pau Guillamat, Jordi Ignés-Mullol, and Francesc Sagués. Control of active liquid crystals with a magnetic field. *Proc. Natl. Acad. Sci. U.S.A.*, 113(20):5498–5502, May 2016.

[47] Rui Zhang, Nitin Kumar, Jennifer L. Ross, Margaret L. Gardel, and Juan J. de Pablo. Interplay of structure, elasticity, and dynamics in actin-based nematic materials. *Proc. Natl. Acad. Sci. U.S.A.*, 115(2):E124–E133, January 2018.

[48] Sriram Ramaswamy. The Mechanics and Statistics of Active Matter. *Annu. Rev. Condens. Matter Phys.*, 1(1):323–345, July 2010.

[49] R. Aditi Simha and Sriram Ramaswamy. Hydrodynamic Fluctuations and Instabilities in Ordered Suspensions of Self-Propelled Particles. *Phys. Rev. Lett.*, 89(5):058101, July 2002.

[50] Sumesh P. Thampi, Ramin Golestanian, and Julia M. Yeomans. Instabilities and topological defects in active nematics. *Europhys. Lett.*, 105(1):18001, January 2014.

[51] H. Wioland, E. Lushi, and R. E. Goldstein. Directed collective motion of bacteria under channel confinement. *New J. Phys.*, 18(7):075002, July 2016.

[52] Andrey Sokolov, Shuang Zhou, Oleg D. Lavrentovich, and Igor S. Aranson. Individual behavior and pairwise interactions between microswimmers in anisotropic liquid. *Phys. Rev. E*, 91(1):013009, January 2015.

[53] Tyler N. Shendruk, Kristian Thijssen, Julia M. Yeomans, and Amin Doostmohammadi. Twist-induced crossover from two-dimensional to three-dimensional turbulence in active nematics. *Phys. Rev. E*, 98(1):010601, July 2018.

[54] Mehrana R. Nejad and Julia M. Yeomans. Active Extensile Stress Promotes 3D Director Orientations and Flows. *Phys. Rev. Lett.*, 128(4):048001, January 2022.

[55] Rayan Chatterjee, Navdeep Rana, R. Aditi Simha, Prasad Perlekar, and Sriram Ramaswamy. Inertia Drives a Flocking Phase Transition in Viscous Active Fluids. *Phys. Rev. X*, 11(3):031063, September 2021.

[56] Guillaume Duclos, Raymond Adkins, Debarghya Banerjee, Matthew S. E. Peterson, Minu Varghese, Itamar Kolvin, Arvind Baskaran, Robert A. Pelcovits, Thomas R. Powers, Aparna Baskaran, Federico Toschi, Michael F. Hagan, Sebastian J. Streichan, Vincenzo Vitelli, Daniel A. Beller, and Zvonimir Dogic. Topological structure and dynamics of three-dimensional active nematics. *Science*, 367(6482):1120–1124, March 2020.

[57] Jack Binysh, Žiga Kos, Simon Čopar, Miha Ravnik, and Gareth P. Alexander. Three-Dimensional Active Defect Loops. *Phys. Rev. Lett.*, 124(8):088001, February 2020.

[58] Jack Binysh, Joseph Pollard, and Gareth P. Alexander. Geometry of Bend: Singular Lines and Defects in Twist-Bend Nematics. *Phys. Rev. Lett.*, 125(4):047801, July 2020.

[59] Ludwig: A lattice Boltzmann code for complex fluids, https://github.com/ludwig-cf/ludwig.

[60] P. G. de Gennes, J. Prost, P. G. de Gennes, and J. Prost. *The Physics of Liquid Crystals*. Oxford University Press, Oxford, England, UK, April 1995.

[61] Friedrich Reinitzer. Beitrage zur Kenntniss des Cholesterins. *Monatshefte für Chemie*, 9(1):421–441, December 1888.

[62] Michel Mitov. Liquid-crystal science from 1888 to 1922: Building a revolution. *Chemphyschem : a European journal of chemical physics and physical chemistry*, 15, 05 2014.

[63] P.M. Knoll and H. Kelker. *Otto Lehmann: Researcher of the Liquid Crystals*. Books on Demand, 2010.

[64] Saša Ziherl, Jerneja Pavlin, Katarina Susman, Saša Glažar, Mojca Čepič, and Natasa Vaupotic. A teaching unit on liquid crystals. 01 2010.

[65] essaycompany.com | Classifications of Liquid Crystals, February 2024. [Online; accessed 23. Feb. 2024].

[66] J.P.F. Lagerwall and G. Scalia. *Liquid Crystals With Nano And Microparticles (In 2 Volumes)*. Series In Soft Condensed Matter. World Scientific Publishing Company, 2016.

[67] Quan Li. *Liquid crystals beyond displays: chemistry, physics, and applications*. John Wiley & Sons, 2012.

[68] Lanfang Li Christopher J. Woolverton, Erin Gustely and Oleg D. Lavrentovich. Liquid crystal effects on bacterial viability. *Liquid Crystals*, 32(4):417–423, 2005.

[69] T. Rijavec and S. Bračko. 7 - smart dyes for medical and other textiles. In L. Van Langenhove, editor, *Smart Textiles for Medicine and Healthcare*, Woodhead Publishing Series in Textiles, pages 123–149. Woodhead Publishing, 2007.

[70] M. D. Asiqur Rahman, Suhana Mohd Said, and S. Balamurugan. Blue phase liquid crystal: strategies for phase stabilization and device development. *Sci. Technol. Adv. Mater.*, 16(3), June 2015.

[71] S. Meiboom and M. Sammon. Structure of the Blue Phase of a Cholesteric Liquid Crystal. *Phys. Rev. Lett.*, 44(13):882–885, March 1980.

[72] Hirotsugu Kikuchi. Liquid Crystalline Blue Phases. In *Liquid Crystalline Functional Assemblies and Their Supramolecular Structures*, pages 99–117. Springer, Berlin, Germany, December 2007.

[73] Hiroyuki Yoshida, Yuma Tanaka, Kosuke Kawamoto, Hitoshi Kubo, Tetsuya Tsuda, Akihiko Fujii, Susumu Kuwabata, Hirotsugu Kikuchi, and Masanori Ozaki. Nanoparticle-Stabilized Cholesteric Blue Phases. *Appl. Phys. Express*, 2(12):121501, November 2009.

[74] M. Kleman and O.D. Laverntovich. *Soft Matter Physics: An Introduction*. Partially Ordered Systems. Springer, 2003.

[75] M. Ravnik, M. Skarabot, S. Zumer, U. Tkalec, I. Poberaj, D. Babic, N. Osterman, and I. Musevic. Entangled Nematic Colloidal Dimers and Wires. *Phys. Rev. Lett.*, 99(24):247801, December 2007.

[76] M. Skarabot, M. Ravnik, S. Zumer, U. Tkalec, I. Poberaj, D. Babic, N. Osterman, and I. Musevic. Interactions of quadrupolar nematic colloids. *Phys. Rev. E*, 77(3):Pt, March 2008.

[77] Patrick S. Noonan, Amit Shavit, Bharat R. Acharya, and Daniel K. Schwartz. Mixed Alkylsilane Functionalized Surfaces for Simultaneous Wetting and Homeotropic Anchoring of Liquid Crystals. *ACS Appl. Mater. Interfaces*, 3(11):4374–4380, November 2011.

[78] Stephanie M. Malone and Daniel K. Schwartz. Polar and Azimuthal Alignment of a Nematic Liquid Crystal by Alkylsilane Self-Assembled Monolayers: Effects of Chain-Length and Mechanical Rubbing. *Langmuir*, 24(17):9790–9794, September 2008.

[79] Xiao Li, Takuya Yanagimachi, Camille Bishop, Coleman Smith, Moshe Dolejsi, Helou Xie, Kazue Kurihara, and Paul F. Nealey. Engineering the anchoring behavior of nematic liquid crystals on a solid surface by varying the density of liquid crystalline polymer brushes. *Soft Matter*, 14(37):7569–7577, September 2018.

[80] J.-B. Fournier and P. Galatola. Modeling planar degenerate wetting and anchoring in nematic. *Europhys. Lett.*, 72(3):403, October 2005.

[81] Jonathan V. Selinger. Interpretation of saddle-splay and the Oseen-Frank free energy in liquid crystals. *Liq. Cryst. Rev.*, July 2018.

[82] Howard C. Berg and Robert A. Anderson. Bacteria Swim by Rotating their Flagellar Filaments. *Nature*, 245:380–382, October 1973.

[83] Dennis Bray. *Cell Movements:From Molecules to Motility*. Taylor & Francis, Andover, England, UK, November 2000.

[84] Eric Lauga. *The Fluid Dynamics of Cell Motility*. Cambridge University Press, Cambridge, England, UK, September 2020.

[85] Michael J Lighthill. On the squirming motion of nearly spherical deformable bodies through liquids at very small reynolds numbers. *Communications on pure and applied mathematics*, 5(2):109–118, 1952.

[86] John R Blake. A spherical envelope approach to ciliary propulsion. *Journal of Fluid Mechanics*, 46(1):199–208, 1971.

[87] Andrew I. Campbell, Stephen J. Ebbens, Pierre Illien, and Ramin Golestanian. Experimental observation of flow fields around active Janus spheres. *Nat. Commun.*, 10(3952):1–8, September 2019.

[88] Saverio E. Spagnolie and Eric Lauga. Hydrodynamics of self-propulsion near a boundary: predictions and accuracy of far-field approximations. *J. Fluid Mech.*, 700:105–147, June 2012.

[89] Knut Drescher, Raymond E. Goldstein, Nicolas Michel, Marco Polin, and Idan Tuval. Direct Measurement of the Flow Field around Swimming Microorganisms. *Phys. Rev. Lett.*, 105(16):168101, October 2010.

[90] Takuji Ishikawa and Masateru Hota. Interaction of two swimming Paramecia. *J. Exp. Biol.*, 209(22):4452–4463, November 2006.

[91] Arthur A. Evans, Takuji Ishikawa, Takami Yamaguchi, and Eric Lauga. Orientational order in concentrated suspensions of spherical microswimmers. *Phys. Fluids*, 23(11), November 2011.

[92] Antony N Beris and Brian J Edwards. . In *Thermodynamics of Flowing Systems: with Internal Microstructure*. Oxford University Press, 08 1994.

[93] Timm Kruger, Halim Kusumaatmaja, Alexandr Kuzmin, Orest Shardt, Goncalo Silva, and Erlend Magnus Viggen. *The Lattice Boltzmann Method*. Springer International Publishing, Cham, Switzerland.

[94] Anthony J. C. Ladd. Numerical simulations of particulate suspensions via a discretized Boltzmann equation. Part 1. Theoretical foundation. *J. Fluid Mech.*, 271:285–309, July 1994.

[95] Anthony J. C. Ladd. Numerical simulations of particulate suspensions via a discretized Boltzmann equation. Part 2. Numerical results. *J. Fluid Mech.*, 271:311–339, July 1994.

[96] N.-Q. Nguyen and A. J. C. Ladd. Lubrication corrections for lattice-Boltzmann simulations of particle suspensions. *Phys. Rev. E*, 66(4):046708, October 2002.

[97] I. Llopis and I. Pagonabarraga. Hydrodynamic interactions in squirmer motion: Swimming with a neighbour and close to a wall. *J. Non-Newtonian Fluid Mech.*, 165(17):946–952, September 2010.

[98] Mikhail M. Genkin, Andrey Sokolov, Oleg D. Lavrentovich, and Igor S. Aranson. Topological Defects in a Living Nematic Ensnare Swimming Bacteria. *Phys. Rev. X*, 7(1):011029, January 2017.

[99] Yashodhan Hatwalne, Sriram Ramaswamy, Madan Rao, and R. Aditi Simha. Rheology of Active-Particle Suspensions. *Phys. Rev. Lett.*, 92(11):118101, March 2004.

[100] Charles W. Wolgemuth. Collective Swimming and the Dynamics of Bacterial Turbulence. *Biophys. J.*, 95(4):1564–1574, August 2008.

[101] On Shun Pak and Eric Lauga. Generalized squirming motion of a sphere. *J. Eng. Math.*, 88(1):1–28, October 2014.

[102] Hai Chi, Mykhailo Potomkin, Lei Zhang, Leonid Berlyand, and Igor S. Aranson. Surface anchoring controls orientation of a microswimmer in nematic liquid crystal. *Commun. Phys.*, 3(162):1–9, September 2020.

[103] Vincenzo J. Pratley, Enej Caf, Miha Ravnik, and Gareth P. Alexander. Three-Dimensional Spontaneous Flow Transition in a Homeotropic Active Nematic. *arXiv*, October 2023.

[104] K. Stratford, O. Henrich, J. S. Lintuvuori, M. E. Cates, and D. Marenduzzo. Self-assembly of colloid-cholesteric composites provides a possible route to switchable optical materials. *Nat. Commun.*, 5(3954):1–8, June 2014.

[105] Igor Musevic, Miha Skarabot, Uros Tkalec, Miha Ravnik, and Slobodan Zumer. Two-Dimensional Nematic Colloidal Crystals Self-Assembled by Topological Defects. *Science*, 313(5789):954–958, August 2006.

[106] Takeaki Araki and Hajime Tanaka. Colloidal Aggregation in a Nematic Liquid Crystal: Topological Arrest of Particles by a Single-Stroke Disclination Line. *Phys. Rev. Lett.*, 97(12):127801, September 2006.

[107] Dinesh Kumar Sahu, Swapnil Kole, Sriram Ramaswamy, and Surajit Dhara. Omnidirectional transport and navigation of Janus particles through a nematic liquid crystal film. *Phys. Rev. Res.*, 2(3):032009, July 2020.